**A Thesis Submitted for the Degree of PhD at the University of Warwick**

**Permanent WRAP URL:**
http://wrap.warwick.ac.uk/131580

# Global Gyrokinetic Simulations of Kinetic Ballooning Modes

by

**James P. Martin Collar**

**Thesis**

Submitted to the University of Warwick

for the degree of

**Doctor of Philosophy**

**Physics**

August 2018

# Contents

# Acknowledgments

I would like to take this opportunity to thank both of my supervisors: Dr. Ben F. McMillan from the Centre for Fusion, Space and Astrophysics department at the University of Warwick and Dr. Samuli Saarelma at Culham Centre for Fusion Energy. Both supervisors have provided much assistance and insight into my work and assisted me in all my endeavours.

I would also like to thank Dr. Alberto Bottino for assisting me with the implementation and normalisation in ORB5 and Dr. Natalia Tronko for assistance with the theory behind ORB5, both at the Max-Planck-Institut für Plasmaphysik, Munich. I deeply appreciated the opportunity to spend a two week working trip with them at IPP.

Many thanks to Prof. Laurent Villard and the rest of his colleagues and students at École Polytechnique Fédérale de Lausanne for their insight into the functioning of ORB5 during the fortnightly video conferences on the code.

I would also like to extend my gratitude to the staff at Culham, who provided me a space to work at for the majority of my PhD and to my office mates, who provided much enjoyment and many interesting and thought provoking conversations.

My biggest thanks go to my family, who have supported and encouraged me during the course of these last four years. During times where I have floundered, they have set me straight and it is thanks to them that I have accomplished as much as I have.

# Declarations

This thesis has been submitted in support of my application for a doctorate in philosophy, to the University of Warwick. All the work present in this thesis has either been compiled or written by me and has not been submitted as part of another qualification. All the work present has been compiled and accomplished by the author except:

- Rough working was provided for the comparison of ballooning modes in a Z-pinch by one of my supervisors, Dr. Ben F. McMillan.
- The routines for creating the circular outermost flux surface equilibrium was provided by one of my supervisors, Dr. Ben F. McMillan.
- The original JET equilibrium, which was provided for me by one of my supervisors, Dr. Samuli Saarelma and is from EFIT.
- The simulations undertaken in MISHKA and GS2, including plots of these simulations, which were performed by one of my supervisors, Dr. Samuli Saarelma.
- Chapter 11 follows the work already published in Ref. [1], completed by S. Saarelma, J.P. Martin Collar, D. Dickinson, B.F. McMillan and C.M. Roach. I prepared and completed the ORB5 simulations of the JET equilibrium presented in this paper.

# Abstract

When a tokamak plasma is heated beyond a certain threshold, a pedestal, a region of large pressure gradient, is formed, which is limited by instabilities including kinetic ballooning modes (KBMs). In order to predict the pedestal height and width more accurately, KBMs must be further understood.

Simulations of the pedestal region require both global and kinetic effects be present. The code used during this thesis, the global gyrokinetic Particle-In-Cell code ORB5, can accomplish this, whereas magnetohydrodynamic (MHD) simulations do not include kinetic effects and local gyrokinetic simulations are only correct in the limit of large system size.

In order to study the physics of KBMs, such as drive strength and mode structure, a simplified circular outer-boundary equilibrium was created and ORB5 simulations compared to MHD and local gyrokinetic simulations in the appropriate limits. These simulations show the error that arises from the neglect of the magnetic field strength fluctuations in ORB5 ($A_{\|}$ formulation). With the corrected drive, ORB5 simulations are shown to agree with other codes in the appropriate limits and analytical theory. The growth rates, in gyrokinetic simulations, of high toroidal number modes are then shown to be equal to MHD growth rates with diamagnetic drift stabilisation. The other kinetic effects are not important.

Simulations of KBMs in the pedestal region were then undertaken, in a JET equilibrium. Firstly, a method is provided for extrapolating equilibria beyond the last closed flux surface, avoiding unphysical suppression due to the simulation boundary. Then, the critical-$\beta$ is found to be the same in ORB5 as in local gyrokinetic simulations without the bootstrap current. Therefore, local simulations, without the bootstrap current, can be used to provide the KBM constraint in the EPED model, used for predicting pedestal parameters.

# Chapter 1

# Introduction

## 1.1 Nuclear Fusion as an energy source

Energy production is one of the main challenges facing humanity in the future. Currently, most energy production relies on non renewable sources, such as coal, gas and oil. However, most current forms of renewable energy are not sufficient to provide the demand for energy [2]. As such, nuclear fusion is currently a promising candidate for the production of the earth's energy in the future.

Fusion does occur in nature in the sun and other stars. In the sun, and in laboratory fusion devices, fusion occurs within a plasma, the fourth state of matter. A plasma consists of a heated ionized gas, with a temperature high enough to allow nuclei to overcome the Coulomb repulsion between them and fuse. There are several possible reactions that could be used in a fusion device, but the most promising reaction, thanks to a combination of cross sectional area, element availability and energy production, is the fusion between Deuterium and Tritium, both isotopes of Hydrogen [3]. This reaction is written as:

$$^2_1D +^3_1 T =^4_2 He(3.5\text{MeV}) +^1_0 n(14.1\text{MeV}). \tag{1.1}$$

It is relatively simple to extract Deuterium from water and Tritium can be produced by bombarding Lithium with neutrons.

The mass of the reaction products are lower than the mass of the Deuterium and Tritium nuclei. This lost mass is converted into energy, as given by $E = mc^2$, resulting in 17.6MeV released per nucleus of Deuterium that fuses with a nucleus of Tritium.

By looking at the energy balance of a fusion device, a condition for ignition (where the fusion reactions heat the plasma enough to overcome losses without any external power source) results in the Lawson criteria [4], where the product of the density, $n_e$, temperature, $T$, and the confinement time $\tau_E$ has to exceed a constant value:

$$n_e T \tau_E \geq 10^{21} \text{keV s/m}^3. \tag{1.2}$$

In the sun, confinement is due to the gravitational force. However, this is not possible on the surface of Earth and so other methods of confinement must be considered. Two main contenders for confinement in a fusion device have arisen, inertial confinement and magnetic confinement. For inertial confinement fusion, the achieved density is $10^{30}\text{m}^3$ and the confinement time is typically $10^{-9}$s. However, in this work the second method is considered, in which plasma, composed of ionised particles, is confined using magnetic fields. For both methods, the temperature is of the order of 10 keV. For magnetic confinement fusion, the density is lower at around $10^{21}\text{m}^3$ for a longer duration of around 1s. Note that both these scenarios fulfil Eqn.(1.2).

## 1.2 Tokamak

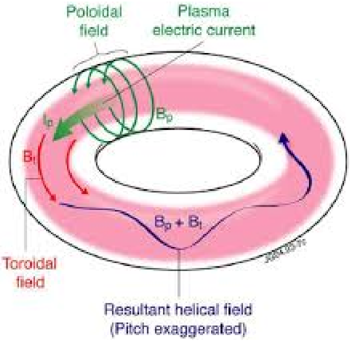

Figure 1.1: The poloidal and toroidal fields in the tokamak [5].

As shown later in Section 2.2.1, charged particles can be confined by magnetic fields. The tokamak is a toroidal device (see Figs. 1.1 and 1.2) whose purpose is to confine a plasma using a magnetic field. The magnetic field $\vec{B}$ consists of both a toroidal magnetic field $\vec{B}_{tor}$ and a poloidal magnetic field $\vec{B}_{pol}$, as shown in Fig 1.1. The

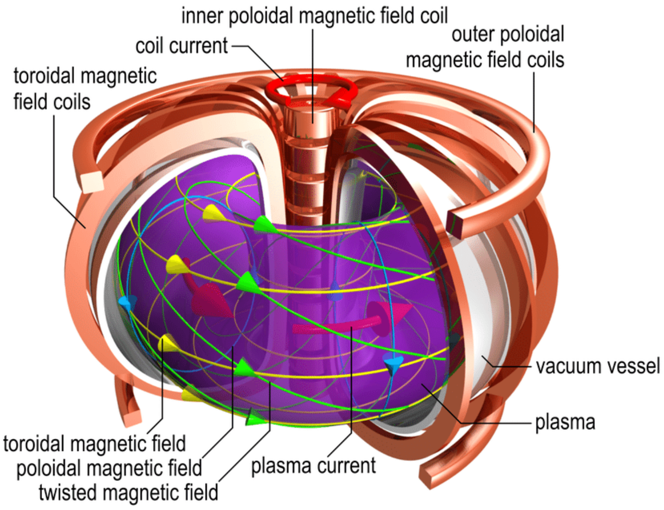

Figure 1.2: The tokamak device [6].

toroidal magnetic field is produced by the central magnetic field coil (see Fig. 1.2) and the poloidal magnetic field is produced by a mixture of the plasma current and coils outside the plasma that shape the plasma. The plasma current is produced by both injecting radio-frequency waves and/or a stream of neutral particles.

## 1.3 H-mode and Pedestal

The plasma within a tokamak can be conceptually split into several regions. The core plasma is the plasma furthest from the vacuum region. The main mechanism for the heat transport (the movement of energy around the plasma) is turbulence, within the core region. Another region in the tokamak is the scrape-off layer (SOL) where the majority of plasma losses occurs, as the plasma travels down the magnetic fields line until it hits the divertor.

When a plasma is heated beyond a certain threshold, the confinement time suddenly increases [7]. In this H-mode (high confinement mode) configuration, the core temperature and density is much higher than the surrounding SOL. The area separating these two regions is known as the pedestal region and is characterised by large temperature and density (pressure) gradients as seen in Fig. 1.3. The main mechanism in the creation and sustenance of the pedestal region is thought to be the suppression of turbulence between the core and the scrape-off layer in a tokamak [7].

The pedestal region is generally not many ion gyroradii wide, for instance the MAST

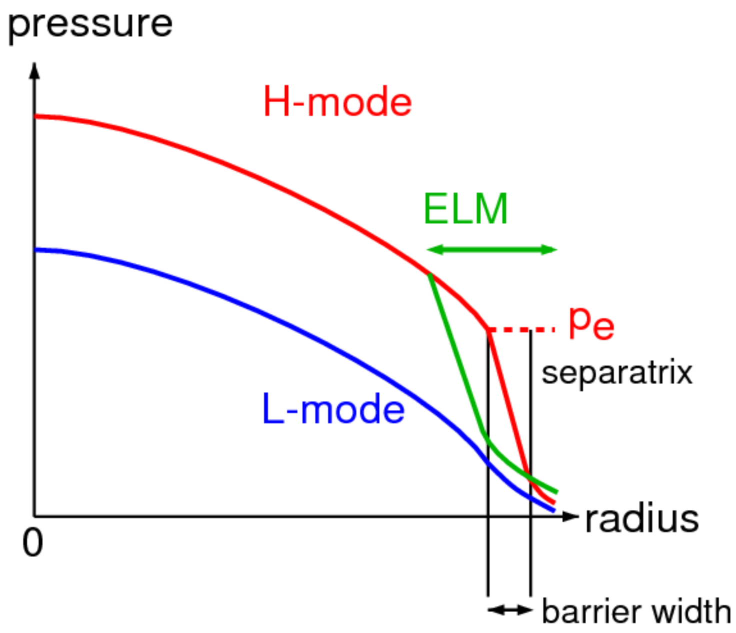

Figure 1.3: The pedestal region in the plasma is the area at the transport barrier, whose width is shown by the two black lines and pressure height is $p_e$. As can be seen, the pressure gradient is greatest in the pedestal region.

pedestal $\approx 5\rho_i$ wide during normal operation.

Another feature that occurs with the transition from L-mode to H-mode is the occurence of Edge-Localized Modes (ELMs) [8] which occur when the high density and temperature gradients in the pedestal lead to a quasi-periodic relaxation of the pressure gradient, during which a large amount of plasma is violently ejected into the surrounding scrape-off layer, potentially leading to damage to the vessel [9] [10].

## 1.4 Instabilities and transport

A system is in equilibrium when all forces are in balance. In a plasma, this results in a plasma where the particles move, but macroscopic properties, such as the density and velocity of the plasma are time invariant.

When a perturbation moves a plasma away from an equilibrium state, there are two outcomes that can occur. Firstly, the plasma can return to the equilibrium, in which the case the plasma is stable. Secondly, the plasma can move further from the equilibrium, in which case the plasma is unstable. This second case, results in an instability in the plasma which grows over time.

The transport of particles and energy in a plasma, which occurs via turbulence and the growth of instabilities, is an area of important research in fusion, since this has a large effect on the power lost from the tokamak and hence the confinement time. The pedestal region results in a suppression of the turbulence and so transport, in this region, occurs via instabilities, such as kinetic ballooning modes that limit the pressure gradient in the pedestal region. In order to minimise the power that is lost from the plasma, these instabilities must be further understood and eliminated or minimised.

## 1.5 Contributions of this thesis

In this thesis, global gyrokinetic simulations of kinetic ballooning modes in the pedestal region in a tokamak equilibrium are performed.

The EPED model [11] [12] [13] is a predictive model for the pedestal height and width in a tokamak. In this model, there are two instabilities that constrain the pedestal height and width: the peeling-ballooning constraint (which is widely understood [14]) and the kinetic ballooning constraint. In order to further understand the kinetic ballooning constraint, simulations have been undertaken in GS2, a local gyrokinetic code. However, the pedestal region is not many gyroradii wide and so local gyrokinetic simulations may not show the correct behaviour for these modes, especially for low toroidal mode number, where modes may be wider than the region of large pressure gradient. Therefore, global effects have to be taken into account. However, global codes have historically been too intensive to use or suffered from numerical issues such as the cancellation problem, further described in Chapter 4. Global codes also suffer from the fact that periodic boundary conditions cannot be used in the radial direction and so a plasma boundary must be included. These boundary conditions are more complicated and can result in the suppression of modes near this boundary.

ORB5 is a global gyrokinetic code that uses a Particle-In-Cell (PIC) method, described in Chapter 4, for the implementation of the distribution function and fields. Recent work prior to this project was the implementation of a solution to the cancellation problem in ORB5, allowing its use for the simulations of kinetic ballooning modes. Therefore during this project, such modes are simulated in a simplified equilibrium first, to allow an understanding of the basic physics, such as the drives. To correctly simulate finite-$\beta$ instabilities in ORB5, without directly solving for the parallel magnetic field perturbation, a correction to the $\nabla B$ drive was introduced.

Secondly, to allow ORB5 to correctly simulate the region near the boundary, it was necessary to create a tool to allow the extension of an equilibrium beyond the last closed flux surface, as shown in Chapter 10. This allows the avoidance of the suppression of modes that occur due to the presence of the boundary so close to the pedestal region.

Several simulations were then undertaken for this equilibrium, which combined the physics understood from the simplified equilibrium with the method for extending the equilibrium. These simulations showed that the important features of KBMs agree with the simulations using GS2 when the bootstrap current, a current that arises spontaneously due to the collision of trapped and passing particles (mentioned in Chapter 2), is removed. Unlike the local results, the presence of the bootstrap current does not result in the plasma achieving second stability and KBMs being suppressed. However, the critical-$\beta$ (the pressure gradient at which KBMs start to grow) is consistent with the values measured in GS2. This, alongside the large increase in growth rate as the $\beta$ increases beyond this critical-$\beta$, provides more evidence that KBMs limit the pedestal gradient between edge localized modes (ELMs).

These simulations will result in a more precise form of the EPED model and therefore a better predictive model of the pedestal height and width, since global simulations include global effects such as the profile shapes (change in the pressure gradient with radius), whereas local simulations assume an infinitely wide space in the radial direction with constant gradients. This will allow for simulations of devices in the future to have more accurate profiles, even before the devices are built. The extension method provided can also be used to create equilibria that allow for the simulations of realistic plasmas, even in codes that only allow the simulation of regions within the last closed flux surface. Finally, the work performed on the simplified equilibrium provides evidence for the functionality of ORB5 and also provides a method for which $A_{\|}$ codes can correct for the effects of $\delta B_{\|}$, for the simulation of KBMs.

## 1.6 Outline

In Chapter 2, some coordinate systems, including those used in ORB5, are described. Then some information is provided about the motion of particles in a magnetic field, including Larmor motion and drifts that arise in the presence of external forces. This is followed by some information about drift modes and KBMs in particular.

In Chapter 3, the $A_{\parallel}$ formalism theory used in ORB5 is provided, including its derivation. The implementation of the equations derived are then discussed in Chapter 4, alongside some issues that arise during this procedure, such as the cancellation problem.

In Chapter 5, the derivation of the gyrokinetic KBM equation is shown and a comparison with the ideal-MHD ballooning equation is provided.

Chapter 6 then shows the MHD equations and derives the Energy Principle, an equation that is used in MISHKA, a code that will be used to validate the ORB5 simulations in the appropriate limits.

Chapter 7 then provides an analysis of the plasma drive that causes the growth of (kinetic) ballooning modes in a simple geometry, a Z-pinch.

Chapter 8 then describes the Grad-Shafranov equation, which is the basis for the creation of equilibria that can then be simulated in codes such as ORB5. The derivation is provided initially. Then, the implementation is provided for HELENA and CHEASE, the two codes which are used during this thesis to create equilibria for simulations.

In Chapter 9, a simplified circular outermost flux surface equilibrium is created, with the pedestal-like region far from the simulation boundary. This equilibrium is then simulated in GS2 (a local gyrokinetic code), MISHKA (an MHD Energy Principle code) and ORB5 in order to understand the drives of ballooning modes and to confirm that ORB5 provides the growth rates expected.

In Chapter 10, a JET-like equilibrium is considered. Due to the presence of the boundary's nearness to the pedestal region, a method is used to extend the region of nested flux surfaces and then the magnetic properties of this extended equilibrium are compared to the properties of the original, to confirm, that on the outboard midplane (where KBMs grow), the extension of the equilibrium does not affect the growth rates of KBMs. Then in Chapter 11, this extended equilibrium is analysed and compared to simulations in GS2 and MISHKA.

# Chapter 2

# Basic Concepts

When a gas is heated sufficiently, it transforms into the fourth state of matter as the bonds within the atoms break so electrons separate from ions and both species act as separate particles. When sufficient atoms are ionized within a material, such that a sufficiently high number of charged particles are present to screen individual charges (i.e. within a Debye sphere), the gas becomes a plasma. Plasmas act similarly to gases, except that the plasma consists of charged particles, which are strongly affected by the presence of magnetic and electric fields.

In this chapter, some basic information about the tokamak device will be provided. Then, the basic motion of particles in the plasma in the presence of magnetic fields will be discussed, followed by a simplified explanation of kinetic ballooning modes, the focus of study for this thesis.

## 2.1 Coordinate systems

To begin describing coordinate systems, a cylindrical coordinate system is chosen, $(R, \phi, Z)$. Using the $\phi$ coordinate as the third spatial coordinate is useful since the tokamak is axisymmetric and so $\partial/\partial\phi = 0$. A common coordinate system used for describing plasma in a tokamak, when the plasma has a circular cross-section, is $(r, \phi, \theta)$, and is defined relative to the cylindrical coordinate system by the following relations, as shown in Fig. 2.1,:

$$R = R_0 + r\cos(\theta), \tag{2.1a}$$

$$Z = r\sin(\theta), \tag{2.1b}$$

$$\phi = \phi. \tag{2.1c}$$

where $R_0$ is the position of the magnetic axis and $r \in [0, a]$ where $a$ is the minor radius.

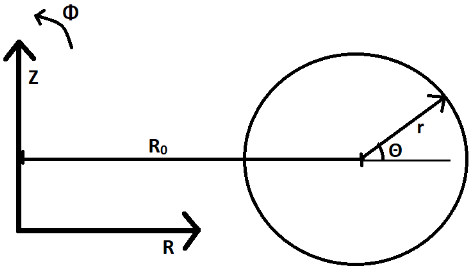

Figure 2.1: $(r, \theta, \phi)$ coordinate for the plasma inside a tokamak.

For the next coordinate system, the poloidal magnetic flux is introduced, $\psi = \int_S \vec{B}.d\vec{\sigma}/2\pi$. The surface $S$ is defined by taking a surface whose edge is the circle defined by $R$,$Z$ = constant going through the central axis at the same value of $Z$ as shown in blue in Fig. 2.2. Then the magnetic flux surface are surfaces where $\psi$ =constant. These surfaces are perpendicular to the magnetic field. The method of the creation of flux surfaces for the simulation equilibrium is given in chapter 8.

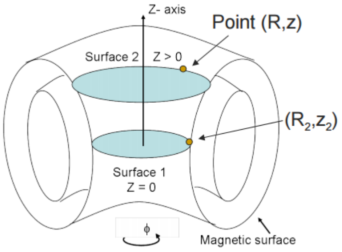

Figure 2.2: Flux surfaces within a tokamak, showing the surface over which the magnetic flux is integrated in blue.

The safety factor of a tokamak equilibrium is the number of times that magnetic field lines loop in the toroidal direction for each loop in the poloidal direction, also known as the twist of the magnetic field line and is defined as:

$$q(\psi) = \frac{1}{2\pi}\oint_{\text{along } B}\frac{d\phi}{d\theta} = \frac{1}{2\pi}\int_0^{2\pi}\frac{\vec{B}\cdot\nabla\phi}{\vec{B}\cdot\nabla\theta}d\theta. \tag{2.2}$$

The safety factor is constant on each flux surface. Using the safety factor, a modified poloidal coordinate can be defined, such that the pitch of the magnetic field line $d\phi/d\chi|_{alongB}$ is constant on a given magnetic flux surface.

$$\chi(\theta) = \frac{1}{q(\psi)}\int_0^{\theta}\frac{\vec{B}\cdot\nabla\phi}{\vec{B}\cdot\nabla\theta'}d\theta'. \tag{2.3}$$

This coordinate system $(\psi, \chi, \phi)$ is known as the straight field line magnetic coordinate system and is used in all the ORB5 simulations detailed in this thesis. In this coordinate system, the spatial gradient operator and volume element are given by .

$$\nabla = \nabla\psi\frac{\partial}{\partial\psi} + \nabla\chi\frac{\partial}{\partial\chi} + \nabla\phi\frac{\partial}{\partial\phi} \tag{2.4}$$

and

$$dV = Jd\psi d\chi d\phi, \tag{2.5}$$

where $\nabla\psi$, $\nabla\chi$ and $\nabla\phi$ are unit vectors and $J$ is the Jacobian, given by

$$J \equiv (\nabla\psi\cdot\nabla\phi\times\nabla\chi)^{-1}. \tag{2.6}$$

The most general form for the equilibrium magnetic field is

$$\bar{B} = \nabla\psi\times\nabla\phi + I(\psi,\chi)\nabla\phi \tag{2.7}$$

with $I$ being a prescribed function. The safety factor then becomes

$$q = \frac{rB_\phi}{R_0 B_\chi} = \frac{1}{2\pi}\oint d\chi\frac{IJ}{R^2}, \tag{2.8}$$

where $r$ is the minor radius.

The straight field line magnetic coordinate system can also be written as $(s, \chi, \phi)$. $\chi$ and $\phi$ are as previously mentioned, but instead of $\psi$, $s = \sqrt{\psi/\psi_{edge}}$ is used as this is more similar to the radial coordinate.

## 2.2 Motion in a magnetic field

### 2.2.1 Larmor motion

Consider a charged particle, with a mass $m$ and charge $q$, moving in the presence of a homogeneous magnetic field $\vec{B} = B\vec{h}$, where $\vec{h} = \frac{\vec{B}}{B}$ and $B = |\vec{B}|$. The velocity of the particle, $\vec{v}$, can be decomposed into two components: $\vec{v} = v_{\|}\vec{h} + \vec{v}_{\perp}$, where $v_{\|} = \vec{v} \cdot \vec{h}$ and $\vec{v}_{\perp} = \vec{v} - v_{\|}\vec{h}$. Then, in the presence of no other forces, Newton's second law gives

$$\frac{d\vec{v}}{dt} = \frac{d\vec{v}_{\perp}}{dt} = \frac{q}{m}\left(\vec{v}_{\perp} \times \vec{B}\right) = \vec{v}_{\perp} \times \vec{\Omega}, \tag{2.9}$$

where $\vec{\Omega} = \Omega\vec{h}$ and $\Omega = \frac{qB}{m}$ is the cyclotron frequency. This means that the rate of change of the perpendicular velocity is perpendicular to both the magnetic field and the perpendicular velocity. This results in a circular motion in the plane perpendicular to the magnetic field. The frequency of the motion is given by the cyclotron frequency and the radius of the motion is given by the Larmor radius, also known as the gyroradius, $\rho = \frac{v_{\perp}}{\Omega}$. The vectorial form of the gyroradius is given by $\vec{\rho} = \frac{\vec{v} \times \vec{B}}{\Omega B}$.

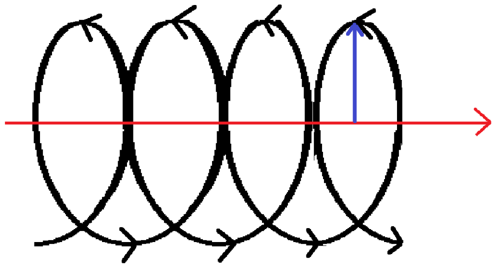

Figure 2.3: The trajectory of a charged particle in the presence of a magnetic field. The red line represents the magnetic field, the black line is the particle trajectory and the blue line is $\vec{\rho}$.

When combined with the parallel velocity of the particle, the gyromotion describes the trajectory of charged particles in a constant straight magnetic field as shown in Fig. 2.3.

### 2.2.2 Particle drifts

If a constant external force, $\vec{F}$ is applied then the motion is found to be

$$v_\parallel(t) = v_\parallel(t_0) + \frac{F_\parallel}{m}(t - t_0), \tag{2.10a}$$

$$\vec{v}_\perp = \vec{v}_D + \vec{v}_{\perp,gc}, \tag{2.10b}$$

$$\vec{v}_D = \frac{1}{qB^2}\vec{F}_\perp \times \vec{B}. \tag{2.10c}$$

where $\vec{v}_{\perp,gc}$ is the gyromotion described in 2.2.1. The perpendicular motion of a charged particle in the presence of a magnetic field and external force, Eqn. 2.10, consists of both the gyromotion and a drift velocity, $\vec{v}_D$.

Take as an example a constant electric field that is perpendicular to the magnetic field $\vec{E}_\perp$. This results in an overall plasma motion, referred to as the $\vec{E} \times \vec{B}$ drift:

$$\vec{v}_{\vec{E}\times\vec{B}} = \frac{\vec{E} \times \vec{B}}{B^2}. \tag{2.11}$$

During one half of the gyromotion, the electric field is speeding up the particle, and so the effective gyroradius is increased. However, during the other half of the gyromotion, the electric field reduces the speed of the particle and so the effective gyroradius is reduced. This causes the particle to have an overall motion perpendicular to both the electric field and the magnetic field, resulting in the $\vec{E} \times \vec{B}$ drift. For most drifts the electrons and ions move in opposite directions since the gyromotions are in opposite directions (from the sign of the charge in Eqn. 2.9). However for the $\vec{E} \times \vec{B}$ drift, both species move in the same direction at the same speed, since the external force is also charge dependent and in opposite directions for the two species, and so there is no net current.

Drifts also arise if the magnetic field is not homogeneous. Firstly, consider a magnetic field with a perpendicular gradient. Suppose that the magnetic field is in the $\hat{z}$-direction and that $\vec{B} = B_z(y)\hat{e}_z$. Again the change in the magnetic field changes the effective size of the gyroradius on opposite halves of the gyromotion. The general case is too complicated to be calculated analytically. However, if the gyroradius is much smaller that the magnetic scale length, then the magnetic field can be Taylor expanded around the gyrocentre (set to $y = 0$)

$$B_z(y) = B_z(0) + y\frac{dB_z}{dy}|_{y=0} + \mathcal{O}(y^2), \tag{2.12}$$

and so the overall force acting on the particle perpendicular to both the gradient of the magnetic field and the magnetic field is

$$F_x = qv_\perp \cos(\Omega t) \left\{ B_z(0) - \frac{dB_z}{dy}|_{y=0} \frac{mv_\perp}{qB} \cos(\Omega t) \right\} \tag{2.13}$$

where $v_y = v_\perp \cos(\Omega t)$ and $y = \frac{mv_\perp}{qB} \cos(\Omega t)$, valid assumptions as this force arises due to unperturbed motion. Then averaging over the gyroangle gives

$$F_x = -\frac{mv_\perp^2}{B} \frac{dB_z}{dy}|_{y=0}. \tag{2.14}$$

Using Eqn. 2.10, the drift can then be calculated as

$$v_{\nabla B} = \frac{mv_\perp^2}{qB^2} \frac{\vec{B}}{B} \times \nabla B. \tag{2.15}$$

Drifts also occur if a particle is travelling in a curved magnetic field. The effective centrifugal force is given by

$$\vec{F}_{curv} = \frac{mv_\parallel^2}{R_c} \frac{\vec{R}_c}{R_c}, \tag{2.16}$$

where $R_c$ is the radius of curvature of the magnetic field and $\vec{R}_c$ is the vector pointed towards the centre of the circle defined by the radius of curvature. The resulting drift is then

$$v_{curv} = \frac{m}{qB} v_\parallel^2 \left( \frac{\vec{R}_c \times \vec{B}}{R_c^2} \right). \tag{2.17}$$

Unlike the $\vec{E} \times \vec{B}$ drift, where ions and electrons move in the same directions, $v_{\nabla B}$ and $v_{curv}$ depend on the charge and so electrons and ions move in opposite directions, resulting in a current.

### 2.2.3 Diamagnetic Drift

Unlike the drifts mentioned above, the diamagnetic drift is not found by considering the motion of an individual particle. The diamagnetic drift arises when there is a gradient in the pressure.

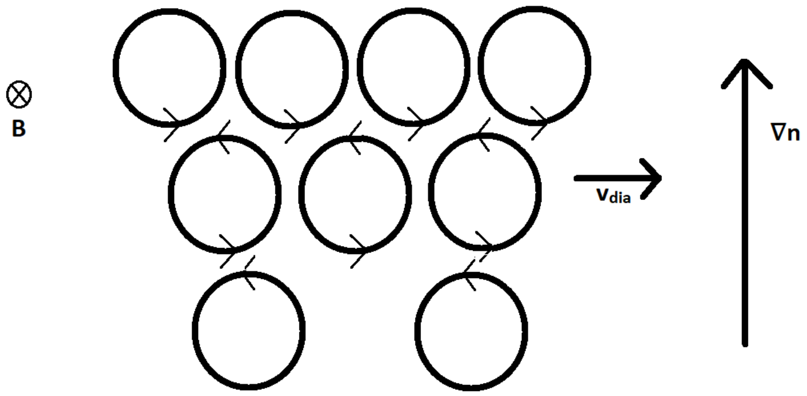

Figure 2.4: Cause of the diamagnetic drift in the presence of a density gradient. The higher density region has more particles present and so in the region between two different densities there is a net current perpendicular to the magnetic field and the density gradient.

Consider a plasma with a density gradient. As can be seen in Fig. 2.4, the density gradient means that there are a greater number of particles gyrating in the region of greater density. At the regions between the rows of guiding centres, there is an overall current due to the imbalance in the number of particles gyrating above and below this connection. As can be seen from the figure, the Larmor rings themselves do not move, but there is an overall fluid velocity present in the plasma.

If the pressure gradient is due to both a density and temperature gradient, then both these mechanisms function together to produce the diamagnetic drift.

The diamagnetic drift is given by

$$\frac{\vec{B} \times \nabla p}{nqB^2}. \tag{2.18}$$

where $\nabla p$ is the pressure gradient, $\vec{B}$ is the magnetic field, $n$ is the density and $q$ is the species charge.

## 2.3 Trapped and Passing Particles

The parallel velocity of a particle can be written as a function of the kinetic energy, $E$ and the magnetic moment, $\mu = \frac{mv_\perp^2}{2B}$, both conserved quantities during a particle's trajectory (see Chapter 3):

$$v_\parallel = \sqrt{\frac{2}{m}(E - \mu B)}. \tag{2.19}$$

As can be seen, if the magnetic moment of the particle is large enough, then the parallel velocity reaches zero before the particle reaches the region of largest magnetic field. In this case, the particle is called a trapped particle. This is the case if $\mu B_{max} \geq E$ and so

$$\frac{v_\parallel}{v_\perp} < \sqrt{\frac{B_{max}}{B(s,\theta)} - 1} \approx \sqrt{\epsilon\,(1 + \cos(\theta))}. \tag{2.20}$$

where $s, \theta$ are two coordinates from the straight field line magnetic coordinates and $\epsilon$ is the aspect ratio. Trapped particles tend to have low parallel velocities, which tend to zero and eventually become negative as the particle heads to the inboard side of the tokamak. This, along with the drifts present at the top and bottom of the tokamak, leads to the motion known as banana orbits, shown in Fig. 2.5. Particles with a high enough parallel velocity to avoid this motion are called passing particles and have trajectories that go all the way around the poloidal plane of the tokamak and always have a non-zero parallel velocity that does not change sign.

The fraction of trapped particles is different on each flux surface. There are more trapped particles on the outer flux surfaces as the aspect ratio is smaller further away from the magnetic axis. The point at which trapped particles reach zero velocity is known as the reflection point.

## 2.4 Electron Drift Modes

Electron drift modes are modes that can grow in even the most simple of configurations of magnetic field and plasma (a non-uniform plasma confined by a straight strong magnetic field) and are also known as 'universal waves' [15]. These instabilities draw upon the thermal energy of the plasma as they propagate perpendicular to the magnetic field. This modes are also characterised by the fact that the wavelength along the magnetic field is finite.

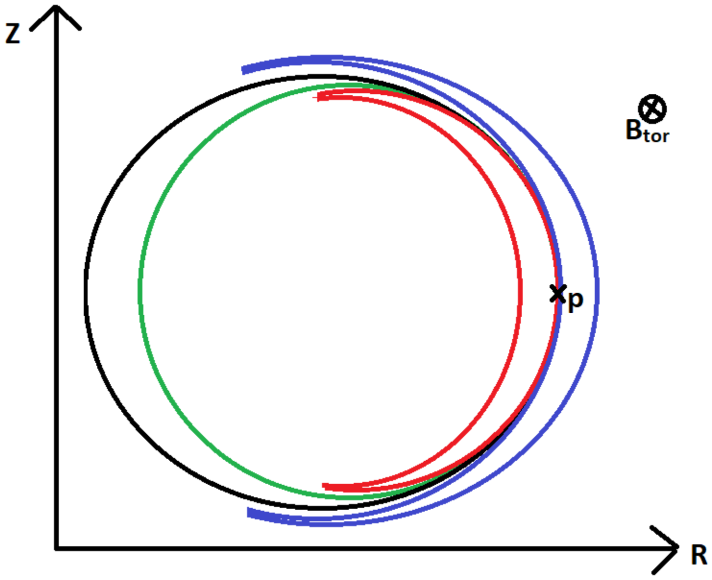

Figure 2.5: Different trajectories for a guiding centre starting at position p. The green and black trajectories represent passing particles with $v_{\|} > 0$ and $< 0$ respectively. The blue and red trajectories represent trapped particles with $v_{\|} > 0$ and $< 0$ respectively, travelling along banana orbits.

Take a plasma slab with a variation in the density and pressure in the $x$-direction, $n_0(x)$ and $p_0(x)$, and a constant strong magnetic field in the $z$-direction, $B_{z,0}$. The dispersion for such waves, from the coupling of drift waves and ion acoustic modes [16], is given by Eqn. 21.40 from Ref. [15]:

$$\left(\omega - \frac{k_z^2 v_A^2}{\omega}\right)\left(1 - \frac{k_y v_{de}}{\omega - k_z^2 C_s^2/\omega}\right) = -\frac{i\eta}{\mu_0} k_\perp^2, \tag{2.21}$$

where $v_A = \frac{B}{(\mu_0 \rho)^{\frac{1}{2}}}$ is the Alfvén velocity, $v_{de} = -\frac{T_{e,0}}{n_{e,0} B_{z,0}} \frac{dn_{e,0}}{dx}$ is very similar to the electron diamagnetic drift, Eqn. 2.18 (different only if there is a temperature gradient along the magnetic field), $C_s = \sqrt{\frac{\gamma T_e}{m_i}}$ is the speed of sound in the plasma ($\gamma$ is the adiabatic index), $\eta$ is the resistivity and $k_\perp$ is the wavenumber perpendicular to the magentic field. In a non-resistive plasma, $\eta = 0$ and there are two branches of waves. The first branch is

$$\omega = v_A k_z, \tag{2.22}$$

which corresponds to a shear Alfvén wave. The second branch is

$$\omega - k_y v_{de} - \frac{k_z^2 C_s^2}{\omega} = 0, \tag{2.23}$$

which represents drift waves.

The ratio between the sound speed and the Alfvén velocity is

$$\frac{C_s}{v_A} = \frac{(\mu_0 n T_e)^{1/2}}{B} \approx \left(\frac{\beta}{2}\right)^{\frac{1}{2}}, \tag{2.24}$$

where $\beta = \frac{2\mu_0 p}{B^2}$ is known as the plasma-$\beta$ and is the ratio of the plasma pressure to the magnetic pressure.

## 2.5 (Kinetic) Ballooning Modes

In MHD theory, ballooning modes are similar to Rayleigh-Taylor instabilities [17]. Unlike Rayleigh-Taylor instabilities, where the destabilizing force is gravity, in ballooning modes the destabilizing forces arise due to the interplay between the force due to pressure gradients, magnetic field line curvature and restoring forces from the magnetic field line bending [18].

On the outboard midplane of the plasma, the magnetic curvature forces are pointed outwards from the centre of the plasma, hence it is known as the region of destabilizing curvature. In addition, the force due to the pressure gradient is pointed in the same direction and is therefore destabilizing also. The force resulting from the stress in bent field lines is the restoring force. When these forces are compared, if the outward forces are greater than the restoring forces, then there is an overall force in the outward direction, that acts as the Rayleigh-Taylor instability at the plasma/vacuum boundary.

In kinetic theory, the mechanics of the kinetic ballooning mode is different. The kinetic ballooning force arises due to the drifts that occur in the plasma. The magnetic curvature and $\nabla B$ drifts mentioned earlier are charge dependent and are in the north south direction as shown in Fig. 2.6. This then creates a charge imbalance, that leads to an electric field. In the presence of an electric field, a $\vec{E} \times \vec{B}$ drift arises, and in this case is directed to the outer edge of the tokamak, in the outboard region. The $\vec{E} \times \vec{B}$ drift is charge independent and so both electrons and ions move in the same direction and the plasma has a movement outwards. This is one of the reasons that a poloidal field is present in a tokamak, in order to limit the growth of such modes by allowing particles to travel parallel to the magnetic field from the outboard side to the inboard side of the tokamak. A more detailed description of kinetic ballooning modes (in a Z-pinch) is provided in Chapter 7.

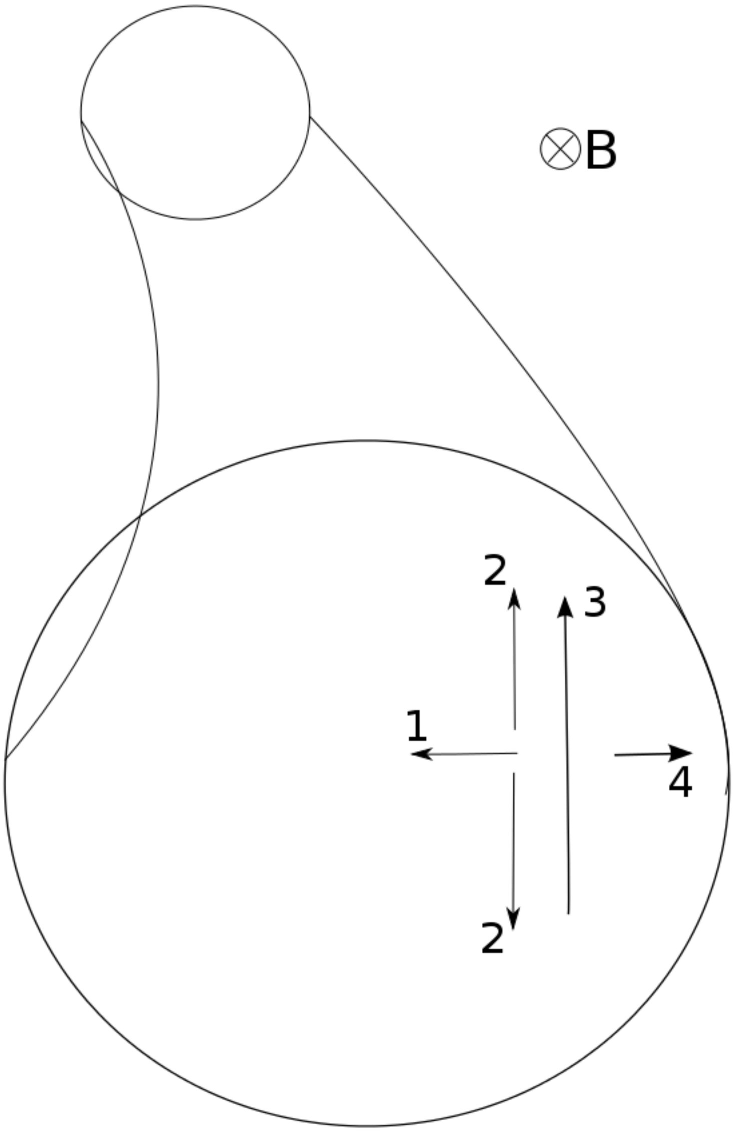

Figure 2.6: The mechanism for KBMs growing in a curved tube of plasma. 1) The $\nabla B$ and curvature forces are directed inwards. 2) This creates a drift that is dependent on the charge of the particles and therefore separates ions and electrons. 3) This creates an electric field. 4) An $\vec{E} \times \vec{B}$ drift, which is charge independent is set up that is directed outwards.

# Chapter 3

# Gyrokinetics

Kinetic theories deal with the statistical behaviour of a large number of particles in the presence of a magnetic field and describe the particles as functions of position, $\vec{x}$, velocity, $\vec{v}$ and time, $t$. Thanks to the particle trajectories, Larmor motion and drifts shown in Chapter 2, it is possible to describe the perpendicular velocity of particles as the sum of the gyromotion and drifts. The gyrokinetic equations are then made independent of the gyroangle as it is an ignorable coordinate. This results in the phase space being reduced from six coordinates to only five.

This transformation of coordinates is possible because the characteristic frequency of drift mode instabilities in the plasma is generally much smaller than the cyclotron frequency and as such drift mode instabilities grow over many gyromotions and the particles can be viewed as rings of charge.

Simply integrating over the gyroangle, the kinetic Vlasov equation [19] does not produce conservative equations of motion [20]. Therefore, methods involving derivations from the Hamiltonian were developed, [21], and implemented in numerical schemes [22].

The goal of the derivation provided in this chapter is to write the Lagrangian in a form that is invariant to the gyroangle, $\theta$, and derive equations of motion from this Lagrangian, that then results in energy conservation. This derivation is shown in more detail in Refs. [20], [23], [24] and [25].

## 3.1 Distribution function and Ordering

In kinetic theory, each particle species is described by a distribution function, $f_\alpha(\vec{x}, \vec{v}, t)$ which gives the probability of finding a particle in a small volume of space around position $\vec{x}$ with velocity in a small volume of velocity space around velocity $\vec{v}$ at time $t$.

The Vlasov equation for species $\alpha$ is

$$\frac{df_\alpha}{dt} = \frac{\partial f_\alpha}{\partial t} + \frac{d\vec{x}}{dt} \cdot \nabla f_\alpha + \frac{d\vec{v}}{dt} \cdot \nabla_{\vec{v}} f_\alpha = 0, \tag{3.1}$$

where $d/dt = \partial/\partial t + d\vec{x}/dt \cdot \nabla + d\vec{v}/dt \cdot \nabla_{\vec{v}}$ is the full time derivative and $\frac{d\vec{x}}{dt}$ and $\frac{d\vec{v}}{dt}$ describe a particle's trajectory through phase space.

The Vlasov equation must then be computed self-consistently with Maxwell's equations [26]:

$$\nabla \cdot \vec{E} = \frac{\rho}{\epsilon_0}, \tag{3.2a}$$

$$\nabla \cdot \vec{B} = 0, \tag{3.2b}$$

$$\nabla \times \vec{E} = -\frac{\partial \vec{B}}{\partial t}, \tag{3.2c}$$

$$\nabla \times \vec{B} = \mu_0 \vec{j} + \mu_0 \epsilon_0 \frac{\partial \vec{E}}{\partial t}, \tag{3.2d}$$

where $\epsilon_0$ and $\mu_0$ are the permittivity and permeability of free space and the charge density and current density for each particle species are

$$\rho_\alpha(\vec{x}, t) = q_\alpha \int d\vec{v} f_\alpha(\vec{x}, \vec{v}, t), \tag{3.3a}$$

$$\vec{j}_\alpha(\vec{x}, t) = q_\alpha \int d\vec{v} f_\alpha(\vec{x}, \vec{v}, t)\vec{v}. \tag{3.3b}$$

Full kinetic theory includes processes at fast timescales which are thought to be irrelevant for tokamak transport [27], where typical frequencies are much smaller than the cyclotron frequency $\Omega_i = qB/m_i$ and are therefore too computer intensive for simulations, especially for global simulations. The most common approaches are fluid theory (MHD) and gyrokinetic theory, where the 6D phase space $(\vec{x}, \vec{v})$ is reduced to a 5D phase space $(\vec{x}, v_\parallel, \mu)$, where $\mu = mv_\perp^2/2B$ is the magnetic moment and the gyroangle, $\theta$, is an ignorable coordinate. Since the velocity of particles can be written in terms of the Larmor motion and drifts, as shown in Chapter 2, the trajectories of the rings of charge are calculated, instead of the trajectories of the particles (whereby the circular Larmor motion would also have to be calculated). Since $\mu$ is a conserved quantity and $\frac{d\theta}{dt}$ does not need to be solved, then instead of having to calculate and solve six equations of motion for the system, only four equations of motion require solving for gyrokinetics: $\frac{d\vec{R}}{dt}$ and $\frac{dv_{\parallel}}{dt}$, where $\vec{R}$ is the position of the gyrocentre in this new coordinate system. The derivation of the equations of motion in these new coordinates are provided in this chapter.

The transformation of coordinates from generic phase space coordinates to gyrocentre coordinates is achieved in two steps: Firstly, they are transformed to guiding centre coordinates, where the $\theta$ dependence of the equilibrium Lagrangian is removed. This guiding centre coordinate tracks the movement of the gyrocentre of the Larmour motion with the $E \times B$ drift. Secondly a transformation, consisting of several small transformations, is undertaken to transform from guiding centre coordinates to gyrocentre coordinates. This is called a Lie transformation, and the generators and gauge are chosen such that the $\theta$ dependence of the perturbed Lagrangian is removed. This coordinate then includes the effects on the gyrocentre trajectory from the other drifts, which are much smaller than the $E \times B$ drift. The different coordinates are shown in Fig. 3.1.

Two small parameters are specified in order to allow for simplification of the resulting equations of motion. The standard gyrokinetic ordering is $\omega/\Omega_{ci} \approx k_{\parallel}/k_{\perp} \approx e\phi/T_e \approx \rho_i/L_n = \mathcal{O}(\epsilon)$, where $\epsilon$ is a small parameter that represents the smallness of $\rho_i$, the ion gyroradius, relative to the characteristic scale lengths of which $L_n$ is one, and $k_{\perp}\rho_i = \mathcal{O}(1)$. $\omega$ is the characteristic fluctuation frequency, $\Omega_{ci}$ is the ion cyclotron frequency, $k_{\parallel}$ and $k_{\perp}$ are the components of the wavevector parallel and perpendicular to the equilibrium magnetic field vector respectively, $\rho_i$ is the ion gyroradius, $L_n = n/\nabla n$ is the density length scale and $\phi$ is the fluctuating electrostatic potential. The second small parameter is $\epsilon_B = \rho_i/L_B$, where $L_B$ is the scale length of the magnetic field.

## 3.2 Lagrangian with general coordinates

In this section, the method for the transformation of the Lagrangian from one generic set of coordinates $\vec{z}$ to another generic set of coordinates $\vec{Z}$. This method is used for

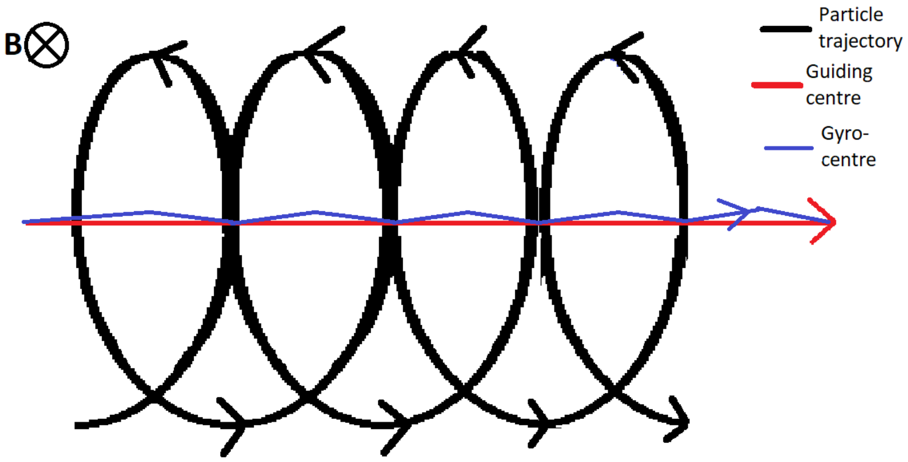

Figure 3.1: Particle, guiding centre and gyrocentre coordinates. The guiding centre trajectory represents the motion of the gyrocentre with the $E \times B$ drift, whereas the gyrocentre coordinates includes the effects from the other drifts, which are much smaller than the $E \times B$ drift.

the first transformation of coordinates, in order to decouple the $\theta$-dependence of the equilibrium part of the Lagrangian, in the derivation shown throughout this chapter.

To begin with the action-variational principle is considered. A single-particle Lagrangian is written as

$$L = \vec{p} \cdot \dot{\vec{q}} - h_c(\vec{q}, \vec{p}, t), \tag{3.4}$$

where $h_c$ is the canonical Hamiltonian of a single particle and $(\vec{q}, \vec{p})$ are the canonical variables, for example $(\vec{q}, \vec{p}) = (\vec{x}, m\vec{v})$. The Lagrangian can be written in terms of an arbitrary coordinate system $\vec{z} = \vec{z}(\vec{q}, \vec{p}, t)$ (with $\vec{q} = \vec{q}(\vec{z}, t)$ and $\vec{p} = \vec{p}(\vec{z}, t)$ by the chain rule:

$$L = \gamma_i \dot{z}^i - h \tag{3.5}$$

where $\gamma_i = \vec{p} \cdot (\partial \vec{q} / \partial z^i)$ at constant $t$ and $h = h_c - \vec{p} \cdot (\partial \vec{q} / \partial t)|_{\vec{z}=const}$ are both functions of $\vec{z}$ and $t$ and $i = 1, ..., 6$ represents the three spatial and three velocity coordinates. Note that summation is used. It is shown that the equations of motion can be derived from the variation of $\int L dt$, in the coordinate system $\vec{z}$.

It is useful to use the Poincaré-Cartan fundamental one-form, a different way of writing the Lagrangian where the transformation of coordinates are more easily seen:

$$\gamma = \gamma_\sigma dz^\sigma = \gamma_i dz^i - hdt, \tag{3.6}$$

where $z^0 = t$ and $\gamma_0 = -h$ for the $\sigma$ summation. Then, under coordinate transform, $\gamma = \gamma_\sigma dz^\sigma = \Gamma_\sigma dZ^\sigma$, with $\Gamma_\sigma = \gamma_\nu(\partial z^\nu / \partial Z^\sigma)$ and $\gamma$ will always have the same form for some $\Gamma_\mu$ in any phase space coordinate system.

The Euler-Lagrange equation, from Eqn. 3.5, is given by

$$L_{ij}\frac{dz^j}{dt} = \frac{\partial h}{\partial z^i} + \frac{\partial \gamma_i}{\partial t}, \tag{3.7}$$

where $L_{ij} = \frac{\delta\gamma_j}{\partial z^i} - \frac{\delta\gamma_i}{\delta z^j}$ are the components of the Euler-Lagrangian tensor. The Euler-Lagrange equation is independent of choice of coordinate since all terms in Eqn. 3.7 transform by multiplying by $\frac{dz^i}{dZ^\alpha}$ (the $\frac{dz^j}{dZ^\beta}$ that multiplies $L_{ij}$ cancels with $\frac{dZ^\beta}{dz^j}$ that multiplies $\frac{dz^j}{dt}$), which is non-zero and can be cancelled.

## 3.3 Electromagnetic Gyrokinetic Derivation

The canonical Hamiltonian for a single particle in the presence of an electrostatic field and a magnetic field is given by

$$h_{c,SP} = \frac{mv^2}{2} + q\phi(\vec{x}, t). \tag{3.8}$$

The Poincaré-Cartan form of this system can then be written as

$$\begin{aligned}\gamma_{SP} &= \left[q\vec{A}(\vec{x}, t) + m\vec{v}\right] \cdot d\vec{x} - \left[\frac{mv^2}{2} + q\phi(\vec{x}, t)\right] dt \\ &= \left[q\vec{A}_0(\vec{x}) + q\delta\vec{A}(\vec{x}, t) + m\vec{v}\right] \cdot d\vec{x} - \left[\frac{mv^2}{2} + q\phi(\vec{x}, t)\right] dt \end{aligned} \tag{3.9}$$

Note that $\vec{A}_0$ is the background magnetic potential and that $\delta\vec{A}$ and $\phi$ are the perturbed magnetic vector and electrostatic potentials of only order $\epsilon$. The next step is to decouple the fast gyromotion implied by Eqn. 3.9. It is simpler to perform this action through a series of steps. Firstly, a set of coordinates is chosen, such that the fast gyromotion is captured at lowest order, based on the unperturbed fields. Finally, the perturbed part is also considered resulting in a Lie transformation, explained in more detail later.

The equilibrium part of $\gamma$ is

$$\gamma_0 = \left[q\vec{A}_0(\vec{x}) + m\vec{v}\right] \cdot d\vec{x} - \frac{mv^2}{2}dt. \tag{3.10}$$

The guiding centre coordinates are defined as

$$\vec{x} = \vec{R} + \left[\frac{v_\perp}{\Omega(\vec{R})}\right]\vec{a}(\vec{R},\theta), \tag{3.11a}$$

$$\mu = \frac{mv_\perp^2}{2B(\vec{R})}, \tag{3.11b}$$

$$U = \vec{v}\cdot\vec{h}, \tag{3.11c}$$

$$\theta = \tan^{-1}\left(\frac{\vec{v}\cdot\vec{e}_1}{\vec{v}\cdot\vec{e}_2}\right), \tag{3.11d}$$

where $\vec{e}_1$ and $\vec{e}_2$ are arbitrary orthogonal vectors in the plane perpendicular to $\vec{h}$, $\vec{a} = \vec{e}_1\cos(\theta) - \vec{e}_2\sin(\theta)$, $\vec{R}$ is the location of the gyrocentre and $\Omega = qB_0(\vec{R})/m$. These new coordinates, Eqn. 3.11, are substituted into Eqn. 3.9 and a Taylor series expansion of $\vec{A}$ is taken, resulting in:

$$\gamma_{SP} = \left[q\vec{A}_0(\vec{R}) + q\delta A_\|(\vec{x},t)\vec{h} + mU(\vec{R})\vec{h}\right]\cdot d\vec{R} + \mu d\theta - \left[\frac{mU^2(\vec{R})}{2} + \mu B(\vec{R}) + q\phi(\vec{x},t)\right]dt, \tag{3.12}$$

with the application of a suitable gauge, since the Euler-Lagrange equations (and hence the One-form) are invariant under a gauge transformation in phase space, and ignoring terms of higher orders in $\epsilon_B$.

This one form can then be written in terms of the canonical parallel momentum: $p_\| = mU + q\delta A_\|$:

$$\gamma_{SP} = \left[q\vec{A} + p_\|\vec{h}\right]\cdot d\vec{R} + \mu d\theta - \left[\frac{\left(p_\| - q\delta A_\|\right)^2}{2m} + \mu B + q\phi\right]dt$$

$$= \left[q\vec{A} + p_\|\vec{h}\right]\cdot d\vec{R} + \mu d\theta - \left[\frac{p_\|^2}{2m} + \frac{q^2\delta A_\|^2}{2m} + \mu B + q\left(\phi - \frac{q\delta A_\| p_\|}{m}\right)\right]dt. \tag{3.13}$$

The $\frac{q^2\delta A_\parallel^2}{2m}$ term produced by this transformation, results in a drift of second order in the equations of motion and is therefore neglected for the rest of this derivation. The effective potential is defined as $\Phi = \phi - \frac{q\delta A_\parallel p_\parallel}{m}$. This means that the derivation of the electromagnetic equations of motion follows that of the electrostatic equations of motion, but with the effective potential replacing the electrostatic potential.

In Eqn. 3.13, the terms at $\mathcal{O}(1)$ are

$$\gamma_0 = \left[q\vec{A}_0(\vec{R}) + p_\parallel \vec{h}(\vec{R})\right] \cdot d\vec{R} + \mu d\theta - \left[\frac{p_\parallel^2}{2m} + \mu B(\vec{R})\right] dt \tag{3.14}$$

and the terms of first order:

$$\gamma_1 = e\Phi(\vec{R} + \vec{\rho})dt. \tag{3.15}$$

### 3.3.1 Lie Transformation

The Lie transformation is used to perform the coordinate transform that removes the $\theta$ dependence from the perturbed part of the Lagrangian. Since the perturbed fields are smaller in magnitude than the unperturbed quantities, more care is necessary in order to keep terms of the same order, while neglecting terms of higher order. The Lie transformation consists of a sequence of transformations at different orders [28]:

$$T = \sum_n T_n, \tag{3.16}$$

where $n$ refers to the order of that transformation.

At first order, only a single Lie transformation is required for the coordinate transform. An individual Lie transform [29] [30] [31] [32] [33] is a near-identity coordinate transformation:

$$T_n = \exp(\epsilon^n L_n) \tag{3.17}$$

Under $T$, a scalar transforms as $S = T^{-1}s$ and the operator $L_n$ acts on a scalar as

$$L_n f = g_n^\sigma(\partial f / \partial z^\sigma), \tag{3.18}$$

where $g_n^\sigma = \partial Z^\sigma / \partial \epsilon^n$ are the generators of the Lie transformation $T_n$. The generators determine how each coordinate is modified by the transformation. The Poincaré-Cartan form transforms as

$$\Gamma = T^{-1}\gamma + dS \tag{3.19}$$

where $\Gamma = \Gamma_\sigma dZ^\sigma$ and $S$ is a gauge transformation in phase space. Then the transformed oneform is given by $\Gamma_0 + \Gamma_1 + ...$, where

$$\Gamma_0 = \gamma_0 + dS_0, \tag{3.20a}$$

$$\Gamma_1 = \gamma_1 - L_1\gamma_0 + dS_1. \tag{3.20b}$$

The latter calculations then consist of choosing forms for the generators and gauge such that, at each order, $\Gamma$ has no dependence on $\theta$.

### 3.3.2 Gyrophase averaged Euler-Lagrange Equations

Now the Lie perturbation is used in order to transform from guiding centre coordinate to gyrocentre coordinates and remove the $\theta$ dependence from the new Poincaré-Cartan form. Eqn. 3.20 are applied to the $\gamma_0$ given in Eqn. 3.10. For simplicity, $dS_0 = 0$ is chosen, meaning that $\Gamma_0 = \gamma_0$. Note for the further equations that $g_n^t = 0$ since time is not transformed. Also note from Eqn. 3.9 that

$$\gamma_1 = -e\Phi(\vec{R} + \vec{a}v_\perp/\Omega)dt. \tag{3.21}$$

The nonzero terms of the Lagrangian tensor, defined in Eqn. 3.7, are used alongside Eqn. 3.20b to give

$$\Gamma_1 = -e\Phi dt + \left(q\vec{g}_1^{\vec{R}} \times \vec{B}^* \cdot d\vec{R} + \vec{g}_1^{\vec{R}} \cdot \vec{h} dp_\parallel + \mu \vec{g}_1^{\vec{R}} \cdot \nabla\Omega dt\right) + \\ g_1^\mu(-d\theta + \Omega dt) + g_1^{p_\parallel}(-m\vec{h} \cdot d\vec{R} + p_\parallel dt) + g_1^\theta d\mu + \frac{\partial S_1}{\partial \vec{R}} \cdot d\vec{R} + \frac{\partial S_1}{\partial p_\parallel} dp_\parallel + \frac{\partial S_1}{\partial \mu} d\mu + \frac{\partial S_1}{\partial \theta} d\theta, \tag{3.22}$$

where $\vec{g}_n^{\vec{R}} \equiv (g_n^{R_1}, g_n^{R_2}, g_n^{R_3})$ and $\vec{B}^* = \nabla \times \vec{A}_0 + (1/q)p_\parallel \nabla \times \vec{h}$. $dS_1$ and $g_1^\sigma$ can be chosen such that all the $\Gamma_{1\sigma}$ vanish except for $\Gamma_{1t}$:

$$\frac{\partial S_1}{\partial \vec{R}} = -q\vec{g}_1^{\vec{R}} \times \vec{B}^* + m\vec{h}g_1^{p_\parallel}, \tag{3.23a}$$

$$\frac{\partial S_1}{\partial p_\parallel} = -\vec{g}_1^{\vec{R}} \cdot \vec{h}, \tag{3.23b}$$

$$\frac{\partial S_1}{\partial \mu} = -g_1^\theta, \tag{3.23c}$$

$$\frac{\partial S_1}{\partial \theta} = g_1^\mu. \tag{3.23d}$$

As it is required that $\Gamma_{1t}$ have no $\theta$-dependence, then the following conditions are imposed: $g_1^{p_\parallel} = 0$ and $\mu\vec{g}_1^{\vec{R}} \cdot \nabla\Omega = e\Phi - e\langle\Phi\rangle$, resulting in

$$\Gamma_{1t} = -e\langle\Phi\rangle. \tag{3.24}$$

The second order terms will not be considered here. The fundamental one form is obtained by adding $\Gamma_0$ and $\Gamma_1$ (Eqn. 3.24). This results in the following equation:

$$\Gamma = \left[q\vec{A}_0(\vec{\bar{R}}) + \bar{p}_\parallel\vec{h}(\vec{\bar{R}})\right] \cdot d\vec{\bar{R}} + \bar{\mu}d\bar{\theta} - \left[\frac{\bar{p}_\parallel{}^2}{2m} + \bar{\mu}B(\vec{\bar{R}}) + e\langle\Phi\rangle\right] dt, \tag{3.25}$$

where $\langle ... \rangle$ is the average over the gyroangle and the gyromotion of particles is simply a change in the $\theta$ coordinate with time. The bars refer to the coordinates where both the original coordinate transform, for the unperturbed Lagrangian, and this Lie transformation has been applied. All further equations are in terms of these coordinates and the bars will be dropped.

The simplification of the gyromotion is only possible thanks to the assumption that the characteristic frequency was much lower than the cyclotron frequency, otherwise if $\phi$ can change rapidly enough, then $\mu$ is no longer a conserved quantity. As an example, assume that $\phi$ changes during the gyromotion such that $\nabla\phi$ always points in the direction of $v_\perp$. Then $v_\perp$ increases and $\mu$ is not conserved.

There are terms of higher order in both $\epsilon$ and $\epsilon_B$, including mixed order terms, that are neglected even in the standard, more complete to second order derivation [34]. This is due to the two step procedure in removing the $\theta$-dependence, firstly the $\epsilon_B$ ordered terms are dealt with using a Lie transformation and then a second Lie transformation is introduced in order to remove $\theta$-dependence on the turbulent fluctuations $\epsilon$. The terms of mixed order are not calculated. However, it is reasonable to expect these terms to not have a large effect since the Lagrangian for drift-kinetics given by Eqn. 2.11 from Ref. [35] has a very similar form to the resultant Lagrangian in the large wavelength limit, despite the fact that the drift-kinetic derivation does not have the same ordering issue for the electrostatic perturbations as the derivation here has.

The Euler-Lagrange equations, Eqn. 3.7, yield

$$\frac{d\mu}{dt} = 0, \tag{3.26a}$$

$$\frac{d\theta}{dt} = \Omega, \tag{3.26b}$$

$$\vec{h} \cdot \frac{d\vec{R}}{dt} = \frac{p_\parallel}{m}, \tag{3.26c}$$

$$-\left[q\vec{B} + p_\parallel \nabla \times \vec{h}\right] \times \frac{d\vec{R}}{dt} - \vec{h}\frac{dp_\parallel}{dt} = \mu\nabla\Omega + q\nabla\Phi. \tag{3.26d}$$

$d\vec{R}/dt$ and $dp_\parallel/dt$ can be written in nicer forms. Taking the cross product of Eqn. 3.26d with $\vec{h}$ and adding Eqn. 3.26c gives an equation for $d\vec{R}/dt$:

$$\frac{d\vec{R}}{dt} = \frac{1}{B^*_\parallel}\left[\frac{p_\parallel}{m}\vec{B}^* + \vec{h} \times \frac{1}{q}\mu\nabla\Omega + \vec{h} \times \nabla\Phi\right], \tag{3.27}$$

where $\vec{B}^* = \nabla \times \vec{A} + \frac{p_\parallel}{q}\nabla \times \vec{h}$. Using the definition of $\vec{B}^*$, Eqn. 3.27 can be written in a more familiar form

$$\frac{d\vec{R}}{dt} = \frac{p_\parallel}{m}\vec{h} + \frac{1}{B^*_\parallel}\left(\left[\frac{1}{q}\mu\nabla\Omega + \frac{p_\parallel^2}{qm}\right]\vec{h} \times \nabla\vec{h} + \vec{h} \times \nabla\Phi\right). \tag{3.28}$$

The term with $\mu$ is the $\nabla B$ drift as $\mu$ is proportional to $v_\perp^2$ as given by Eqn. 2.15, the term with $p_\parallel^2$ is proportional to $v_\parallel^2$ and is therefore the curvature drift as seen in Eqn. 2.17 and the final term with $\nabla\Phi$ is the $\vec{E} \times \vec{B}$ drift as $\nabla\Phi$ is the electric field. Taking the dot product of Eqn. 3.26d and $\vec{B}^*$ provides the parallel acceleration equation:

$$\frac{dp_\parallel}{dt} = -\frac{1}{B^*}\vec{B}^* \cdot (\mu\nabla\Omega + e\nabla\Phi) = -\left(\vec{h} + \frac{p_\parallel}{qB^*}\vec{h} \times \vec{h} \cdot \nabla\vec{h}\right) \cdot (\mu\nabla\Omega + e\nabla\Phi). \tag{3.29}$$

## 3.4 Gyrokinetic Vlasov-Poisson equations

In this section, the Poisson and Ampere equations are derived by transforming the coordinates in the original equations.

For the Poisson equations, the gyroaveraged density is required. The density is given by

$$n_i(\vec{x}) = \int f(\vec{z})\delta(\vec{R}+\vec{\rho}-\vec{x})d^6z. \tag{3.30}$$

Under a Lie transformation (at $\mathcal{O}(\epsilon)$ the distribution function, $f(\vec{\bar{R}})$, becomes

$$f(\vec{Z}) = T^{-1}f(\vec{z}) = 1 + L_1 f(\vec{z}) + \mathcal{O}(\epsilon^2), \tag{3.31}$$

According to Eqn. 3.18

$$L_1 f(\vec{z}) = g_1^{\sigma}\frac{\partial f}{\partial z^{\sigma}} = g_1^{\mu}\frac{\partial f}{\partial \mu} + \vec{g}_1^{\vec{R}}\cdot\frac{\partial f}{\partial \vec{R}} + g_1^{p_\parallel}\frac{\partial f}{\partial p_\parallel}. \tag{3.32}$$

Therefore the density is given by

$$n_i(\vec{x}) = \int \left[f(\vec{Z}) + g_1^{\mu}\frac{\partial f}{\partial \mu} + \vec{g}_1^{\vec{R}}\cdot\frac{\partial f}{\partial \vec{R}} + g_1^{p_\parallel}\frac{\partial f}{\partial p_\parallel}\right]\delta(\vec{R}+\vec{\rho}-\vec{x})Jd^6Z \tag{3.33}$$

where $J = \frac{\partial \vec{Z}}{\partial \vec{z}}$ is the Jacobian.

Hence, the Vlasov-Poisson equations are as follows:

$$\frac{\partial f}{\partial t} + \frac{dp_\parallel}{dt}\frac{\partial f}{\partial p_\parallel} + \frac{d\vec{R}}{dt}\cdot\frac{\partial f}{\partial \vec{R}} = 0, \tag{3.34}$$

$$\epsilon_0\nabla^2(\phi) = -\sum_\alpha q\left\{\int Jd^6Z\left[f(\vec{Z}) + g_1^{\mu}\frac{\partial f}{\partial \mu} + \vec{g}_1^{\vec{R}}\cdot\frac{\partial f}{\partial \vec{R}} + g_1^{p_\parallel}\frac{\partial f}{\partial p_\parallel}\right]\delta(\vec{R}+\vec{\rho}-\vec{x})\right\}, \tag{3.35}$$

and Ampere's Law is given by

$$\begin{aligned}\nabla^2(\vec{A}+\delta A_\parallel\vec{h}) = -\mu_0 q\Bigg[\int Jd^6\bar{Z}\left(\frac{p_\parallel}{m}\vec{h}\right)\left(g_1^{\mu}\frac{\partial f_i}{\partial \mu} + \vec{g}_1^{\vec{R}}\cdot\frac{\partial f_i}{\partial \vec{R}} + g_1^{p_\parallel}\frac{\partial f_i}{\partial p_\parallel}\right)\\ \times\,\delta(\vec{R}+\vec{\rho}-\vec{x}) - \int d\vec{v}\vec{v}f_e(\vec{x},\vec{v},t)\Bigg],\end{aligned} \tag{3.36}$$

where $g_n^\sigma$ are the generators for Lie transformation as defined earlier. Note that the quasi-neutrality equation described later is used instead of the Poisson equation due to the difference in magnitude between the polarization density and the vacuum polarization terms. The quasi-neutrality equation is derived by taking the left hand side of Eqn. 3.35 to be zero.

The Poisson equation can be derived by using the $\phi$ variation of the Lagrangian. This method is described in Ref. [36] and produces self-consistent equations for the evolution of the electromagnetic potentials alongside the Vlasov equation. However, the equations for the evolution of $\phi$ and $\vec{A} + \delta A_\| \vec{h}$ derived using the Lagrangian are the same as the equations derived here, where the Poisson and Ampere equations are transformed from generic phase space coordinates to gyrocentre coordinates.

## 3.5 Gyrokinetic Equilibrium

The control-variate method involves splitting the distribution function into an analytical time independent function $f_0$ and a time dependent part $\delta f$ [37], resolved using the Particle-in-Cell method describe in Chapter 4:

$$f(\vec{R}, p_\|, \mu, t) = f_0(\vec{R}, p_\|, \mu) + \delta f(\vec{R}, p_\|, \mu, t). \tag{3.37}$$

In this thesis, linear simulations are performed in ORB5 and so $f_0$ is important, as it is the state around which the linearisation is performed. Another, less important, reason for this split is the numerical noise, which is proportional to $(\delta f / f_0)^2$ [38] and so for good numerical performance $\delta f \ll f_0$. The Vlasov equation is fully non-linear. It is Eqns. 3.35 and 3.36 that are linearised as explicit forms for the electrostatic potential and magnetic potential.

$f_0$ is the background distribution function, it is simplest to use a function of the constants of motion, as this is a solution to the Vlasov equation in an unperturbed equilibrium:

$$\begin{aligned} f_0 &= f_0(c_1, c_2, c_3, ...), \\ \frac{dc_i}{dt} &= 0. \end{aligned} \tag{3.38}$$

The constants of motion in gyrokinetics are the canonical toroidal momentum $\psi_{can}$, the magnetic moment $\mu$ and the energy $e$ [39] [40] [41]:

$$\psi_{can} = \psi + \frac{v_{\|}\Omega_i}{B^2} f(\psi), \tag{3.39a}$$

$$\mu = \frac{v_{\perp}^2}{2B}, \tag{3.39b}$$

$$e = \frac{m_i}{2}(v_{\|}^2 + v_{\perp}^2). \tag{3.39c}$$

Recall that $\psi$ is the poloidal flux, defined in Chapter 2, with regards to coordinate systems. To lowest order, global gyrokinetic equilibria can be approximated by a local equilibria and so an approximate solution to the steady state gyrokinetic equations can be approximated by the local gyrokinetic solution [42]. It is therefore common in gyrokinetic codes to use a local Maxwellian for the background distribution function:

$$f_{i,0}(e, \mu, \psi) = \frac{n_{i,0}(\psi)}{(2\pi)^{\frac{3}{2}} v_{th,i,0}^3(\psi)} \exp\left(-\frac{e}{T_i(\psi)}\right) \tag{3.40}$$

where $v_{th,i,0} = \sqrt{T_i/m_i}$ is the thermal velocity of an ion.

The Vlasov equation, alongside the $\delta f$ ansatz, is written as [43]

$$\frac{d\delta f}{dt}(\vec{R}, v_{\|}, \mu, t) = -\frac{df_0}{dt}(\psi, v_{\|}, \mu) = \tau(\nabla\Phi), \tag{3.41}$$

where

$$\tau(\nabla\Phi) = -f_0(\psi, v_{\|}, \mu)\left(\kappa(\psi)\frac{d\psi}{dt} - \frac{q_i}{T(\psi)}\langle\nabla\Phi\rangle \cdot \frac{d\vec{R}}{dt}\right) \tag{3.42}$$

Choosing a local Maxwellian for the background distribution is the simplest choice and produces the correct density when integrated over the velocity space, but produces spurious zonal flow oscillations since it is not a true equilibrium distribution function as $df_0/dt \neq 0$ [44] [38]. However, since only linear simulations are performed in this thesis, these spurious flows do not arise, since the modes that produce these spurious flows are linearly stable [45].

## 3.6 Quasi-Neutrality

In the Poisson equation, Eqn. 3.35, for wavelengths larger than the Debye length, the vacuum term on the right hand side of the equation is much smaller than the polarization response of the plasma [46]. This means that the vacuum term on the right hand side can be neglected and the quasi-neutrality condition is used instead of the Poisson equation.

The quasi-neutrality constraint is

$$n_e = Z_i n_i. \tag{3.43}$$

The ion density is then written as $n_i = \langle n_i \rangle + n_{i,pol}$. Then, the polarization density for ions can be calculated from Eqn. 3.35 by setting the left hand side to 0, using the above relationship:

$$n_{i,pol} = \int \left\{ \frac{q_i}{m_i B}(\phi - \langle\phi\rangle)\frac{\partial f}{\partial \mu} + \frac{q_i}{mi\Omega_i^2}\nabla\left[\int d\alpha(\phi - \langle\phi\rangle)\right] \times \frac{\vec{B}}{B}\cdot\nabla f \right\}$$

$$\delta(\vec{R} + \vec{\rho}_i - \vec{x})B_{\parallel}^* d\vec{R} dv_{\parallel} d\mu d\alpha. \tag{3.44}$$

The second term on the right hand side (with the integral over $\alpha$) of Eqn. 3.44 is neglected, despite being of the same order as the first term (both $\mathcal{O}(\epsilon^2)$ for a general $f$). This is because in ORB5, when $f$ is replaced by $f_0$, when the equation is linearised, the order of the first term is further increased to $\mathcal{O}(\epsilon_B)$ whereas the second term remains at the same order. Therefore the second term is neglected. After taking the long wavelength approximation $k_\perp \rho_i \ll 1$ (only valid for low toroidal mode number simulations), the polarization density, Eqn. 3.44, is

$$\nabla_{pol} \cdot \left( \frac{n_{i,0}}{B\Omega_i} \nabla_\perp \phi(\vec{R}, t) \right). \tag{3.45}$$

with the derivation using a Taylor series expansion of $\phi$ and $\nabla_{pol} = \nabla_{R,Z}$ is the gradient in the poloidal plane.

The quasi-neutrality condition is then

$$n_{e,0}(\Upsilon) + \delta n_e = Z_i \langle n_{i,0} \rangle(\vec{R}) + Z_i \nabla_\perp \cdot \left( \frac{n_{i,0}}{B\Omega_i} \nabla_\perp \phi(\vec{R}, t) \right) + Z_i \delta n_i, \tag{3.46}$$

where $\langle ... \rangle$ is the average over the gyroangle, $\bar{\phi}$ is the flux-surface averaged potential and

$$\delta n_s = \int B_{\parallel}^{*} d\vec{R} dv_{\parallel} d\mu d\alpha \delta f_s(\vec{R}, v_{\parallel}, \mu, t)\delta(\vec{R} + \vec{\rho}_i - \vec{x}). \tag{3.47}$$

Note that the assumption is made that $\nabla_{pol} \approx \nabla_{\perp}$, which is true for a tokamak with a high safety factor, $q$. Then it is assumed that $\langle n_{i,0} \rangle = n_{i,0}$ and $n_{i,0} = n_{e,0}/Z_i$ holds for any equilibrium distribution function (although this is only approximately valid), so $n_{i,0} = n_{e,0}/Z_i = n_0$. Then the quasi-neutrality equation becomes

$$-\nabla_{\perp} \cdot \left( \frac{Z_i n_0}{B \Omega_i} \nabla_{\perp} \phi(\vec{R}, t) \right) = Z_i \delta n_i - \delta n_e. \tag{3.48}$$

On the right hand side of Eqn. 3.48 is the difference in density between ions and electrons and hence the difference in charge density between the two species. Therefore Eqn. 3.48 states that any imbalance in charge that arises in the plasma results in a polarization drift that acts to reduce the charge imbalance.

# Chapter 4

# ORB5 numerical implementation

The global gyrokinetic code, ORB5, is the main tool used in this thesis for stability analysis, so its numerical formulation will be discussed in detail.

In this chapter, the methods, used in ORB5, of performing the discretization of the global gyrokinetic equations derived in Chapter 3 are provided. This electromagnetic formalism suffers from a numerical issue known as the cancellation problem [47], and the solution used in ORB5 is explained.

The version of ORB5 used for the simulations detailed later is version 776 on Alberto's branch from the NEMORB svn repositories https://spcsvn.epfl.ch/repos/NEMORB/branches/alberto/trunk/ . There are newer versions of the code not used during this thesis, where some assumptions made in this derivation are relaxed.

## 4.1 Particle-in-Cell Method

In the Particle-in-Cell method, the markers, representing part of the particle distribution function, are tracked in a continuous phase space, but the densities and currents that are used to calculate the fields are stored on a grid so some interpolation is required, or (for ORB5) finite elements. The Particle-in-Cell method is a commonly used approach in gyrokinetic codes [22] [44] [48] [49] [50]. This method has been shown to be an effective method of performing gyrokinetic simulations, especially for parallelisation over many cores [51]. However, the sampling of markers results in statistical noise. This noise can be mitigated by increasing the number of markers, but the time for the simulations to complete increases as the number of markers increase.

## 4.2 Discretization of $\delta$f

In ORB5, each volume element, $\Omega_p$ is represent by a marker $p$. Markers are used instead of particles in order to minimise the number of objects being followed: $10^7 - 10^9$ markers are used for $10^{20}$ particles. Then for a single species, the perturbed distribution function is discretised using $N$ markers:

$$\delta f = \frac{N_{ph}}{N} \sum_{p=1}^{N} \frac{1}{2\pi B_{\|}^{*}} w_p(t) \delta(\vec{R} - \vec{R}_p(t)) \delta(v_{\|} - v_{\|p}(t)) \delta(\mu - \mu_p(t)), \tag{4.1}$$

where $N_{ph}$ is the physical number of particles (i.e. the distribution function integrated over velocity and position space) and $N$ is the total number of markers. Each marker is then characterised by its weight $w_p(t)$ and its position in the 5D phase space $(\vec{R}_p(t), v_{\|p}(t), \mu_p(t))$. For the collisionless case, due to Eqn. 3.26a, $\mu(t) = \mu(t_0)$.

To find $w_p$ in terms of $\delta f$, Eqn. 4.1 is integrated over the volume of a marker, $\Omega_p$:

$$\int_{\Omega_p} d^3R d^3v \delta f = \int_{\Omega_p} d^3R d^3v \frac{N_{ph}}{N} \sum_{p=1}^{N} \frac{1}{2\pi B_{\|}^{*}} w_p(t) \delta(\vec{R} - \vec{R}_p(t)) \delta(v_{\|} - v_{\|p}(t)) \delta(\mu - \mu_p(t_0)). \tag{4.2}$$

As $\Omega_p \to 0$, $\delta f \approx \delta f_p$ where $\delta f_p$ is the average value over the volume $\Omega_p$ and hence

$$\int_{\Omega_p} d^3R d^3v \delta f = \delta f_p \int_{\Omega_p} d^3R d^3v = \delta f_p \Omega_p. \tag{4.3}$$

Since $\Omega_p$ only includes one marker, marker $p$,

$$\begin{aligned} \delta f_p \Omega_p = \int_{\Omega_p} d^3R d^3v \frac{N_{ph}}{N} \frac{1}{2\pi B_{\|}^{*}} w_p(t) \delta(\vec{R} - \vec{R}_p(t)) \delta(v_{\|} - v_{\|p}(t)) \delta(\mu - \mu_p(t_0)) \\ = \frac{N_{ph}}{N} w_p(t). \end{aligned} \tag{4.4}$$

since delta functions, $\delta(x)$ have a value of 0 at all locations except at $x = 0$.

Therefore, since $\Omega_p$, $N_{ph}$ and $N$ are time independent ($\Omega_p$ is time independent due to Liouville's Theorem [52]), the temporal evolution of the marker weights is given by inserting Eqn. 4.1 into Eqn. 3.41

$$\frac{dw_p}{dt} = \frac{N}{N_{ph}} \tau(\vec{E})_p \Omega_p, \tag{4.5}$$

where $\Omega_p = \frac{B_{\|}^* d\vec{R} dv_{\|} d\mu d\theta}{dN}$ is the volume of a marker in phase space centred around the position of the marker and $dN$ is the number of markers in an infinitesimal volume of phase space.

## 4.3 Equations of motion

The markers are pushed using magnetic coordinates $(s, \chi, \phi)$. For the time integration of Eqns. 3.28, 3.29 and 4.5, a Runge-Kutta integrator of fourth order is used in ORB5 [53]. This results in a local error of $\mathcal{O}(h^5)$ (i.e. for each step), where $h$ is the time step which is set in the input, resulting in a total error of $\mathcal{O}(h^4)$.

When a marker leaves the plasma (when $s > 1$), it is reflected ($\chi \rightarrow -\chi$) in order to maintain even sampling of phase space. If the equilibrium is up-down symmetric, then the constants of motion are conserved from this action. However, if the equilibrium is not up-down symmetric, this leads to violations of the conservation of conserved quantities. All equilibria used in this thesis are up-down symmetric to avoid this issue. Newer versions of the code, however, allow up-down non-symmetric equilibria to be used without this problem.

## 4.4 Quasi-Neutrality Equation

In the input file, a number of grid intervals is given $N_s$, $N_\chi$ and $N_\phi$. Therefore the number of grid points, on which the fields are stored is given by $(N_s + 1)(N_\chi + 1)(N_\phi + 1)$, where due to periodic nature of $\chi$ and $\phi$, the value at the grid points $(s, 0, \phi) = (s, N_\chi, \phi)$ and similarly for $\phi$.

The quasi-neutrality equation, Eqn. 3.48 is solved with linear, quadratic or cubic B-splines finite elements [54] whose basis functions are shown in Fig. 4.1. The

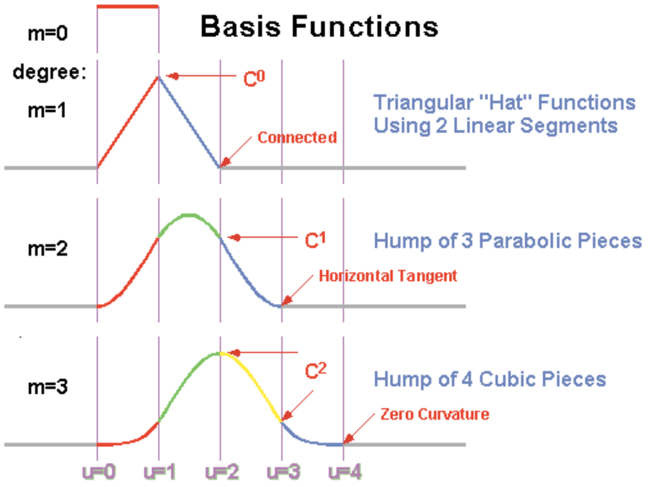

Figure 4.1: Basis functions, in a single coordinate, for B-splines of different degrees. ORB5 uses up to cubic splines (degree 3).

perturbed potential is discretised as a sum of tensor products of 1D B-splines:

$$\phi(\vec{x},t) = \sum_{\mu} \phi_\mu(t)\Lambda_\mu(\vec{x}), \tag{4.6}$$

where $\mu$ stands for $j,k,l$, $\phi_\mu$ are coefficients and $\Lambda(\vec{x})$ is the tensor products of 1D B-splines [43]. The Galerkin method [55], which involves using a test B-spline and integrating the equation over the entire space, gives a linear system for $\phi(t)$. Then, inserting Eqn. 4.6 for the fields and Eqn. 4.1 for the distribution function into the quasi-neutrality equation, Eqn. 3.48, gives

$$\sum_{\mu} A_{\mu\nu}\phi_\mu(t) = b_\nu(t), \tag{4.7}$$

where

$$A_{\mu\nu} = \int d\vec{x}\frac{n_0(\Upsilon)}{Z_i T_e(\Upsilon)}\Lambda_\mu(\vec{x})\Lambda_\nu(\vec{x}) + \frac{n_0(\Upsilon)}{B\Omega_i}\nabla_\perp\Lambda_\mu(\vec{x})\cdot\nabla_\perp\Lambda_\nu(\vec{x}), \tag{4.8a}$$

$$b_\nu(t) = \frac{N_{ph}}{N}\sum_{p=1}^{N}\frac{w_p(t)}{2\pi}\int_0^{2\pi} d\alpha\Lambda_\nu\left(\vec{R}_p + \vec{\rho}_{i,p}(\alpha)\right). \tag{4.8b}$$

The Eqn. 4.7 is then further approximated by using $\nabla_\perp \approx \nabla_{pol} = \nabla s\frac{\partial}{\partial s} + \nabla\chi\frac{\partial}{\partial\chi}$, valid when $B_{pol} \ll B_{tor}$. This is the case when $q > 1$, and as such is the case for all equilibria used in this thesis. A discrete Fourier transform on $\phi_\mu$ and $b_\nu$ is used for numerical performance reasons. The resulting equation is

$$\sum_\mu \hat{A}_{\mu\nu}\hat{\phi}_\mu^{(n)}(t) = \frac{\hat{b}_\nu^{(n)}(t)}{M^{(n),p}}, \tag{4.9}$$

where $\hat{b}^{(n)}$ are the Fourier coefficients of $b$ and $M^{(n),p}$ are computed analytically.

## 4.5 Gyroaveraging and Fourier Filter

The electric field and the perturbed distribution functions need to be integrated over the gyroangle for Eqn. 4.8b and the equations of motion. This is computed via a discrete sum with a variable number of points $N_{gc} = min(32, max(4, 4\rho_{i,p}/\rho_i))$ where $\rho_{i,p} = v_{\perp,p}/\Omega_{i,p}$ is the marker gyroradius and $\Omega_{i,p}$ is the cyclotron frequency of the marker. While only a 4-point discretization is necessary to describe perturbations up to $k_\perp\rho_i \approx 1$ [50], the noise is reduced if more points are chosen [49]. The position of the points on the Larmor ring are approximated as a circle around the gyrocentre in the poloidal plane:

The gyroaveraged electric field is given by

$$\langle\vec{E}\rangle = -\frac{1}{2\pi}\nabla\sum_\mu \phi_\mu(t)\int d\alpha\nabla\Lambda_\mu\left(\vec{R} + \vec{\rho}_i(\alpha)\right). \tag{4.10}$$

ORB5 uses a Fourier filter on the perturbed distribution function in order to keep only field-aligned modes consistent with gyrokinetic ordering [56]. $N$ and $M$ are the toroidal and poloidal mode numbers of the growing instability respectively. Modes tend to grow most rapidly for poloidal mode numbers that are given by $M/N \approx q$ as the mode is aligned with the magnetic field line and hence stabilisation of the mode is minimised. Therefore physically non-relevant modes can be removed from the simulation and specific modes can be looked for, even though they may not be the fastest growing modes in the tokamak. The filter used in the simulations detailed later is the diagonal filter. The diagonal filter takes as inputs: $N_{min}$, $N_{max}$, $M_{min}$, $M_{max}$ and $\Delta M$ and for each $N$ in the range $[N_{min} : N_{max}]$ allows the poloidal modes $[Nq \pm \Delta M] \cap [M_{min} : M_{max}]$. This centres the region where modes grow most rapidly.

## 4.6 Cancellation Scheme

### 4.6.1 Cancellation Problem

Gyrokinetic codes can use either $v_\parallel$ or $p_\parallel = mv_\parallel - qA_\parallel$, as ORB5 does, as a phase-space variable. In general, global gyrokinetic codes use the $p_\parallel$ formalism to allow an explicit time solver [57]. However there is a price to pay, the cancellation problem [58], which can give rise to large numerical errors.

In the $v_\parallel$ formalism, the equations of motion [47] are:

$$\frac{d\vec{R}}{dt} = v_\parallel \frac{\vec{B}^*}{B^*_\parallel} + \frac{1}{eB^*_\parallel}\vec{h} \times \left\{ \mu\nabla B + e\left(\nabla\langle\phi\rangle + \frac{\partial\langle A_\parallel\rangle}{\partial t}\vec{h}\right)\right\}, \tag{4.11a}$$

$$\frac{dv_\parallel}{dt} = -\frac{\vec{B}^*}{m_i B^*_\parallel}\cdot\mu\nabla B - \frac{e}{m_i}\left(\frac{\vec{B}^*}{B^*_\parallel}\cdot\nabla\langle\phi\rangle + \frac{\partial\langle A_\parallel\rangle}{\partial t}\right), \tag{4.11b}$$

and the parallel Ampere's Law is

$$-\nabla^2_\perp A_\parallel = \mu_0 \sum_\alpha j_\parallel \tag{4.12}$$

where $j_\parallel$ is the parallel gyrocentre current. The $\partial\langle A_\parallel\rangle/\partial t$ terms on the right hand side of Eqn. 4.11 for the parallel acceleration prevents the use of an explicit time solver. This is because the fields ($\phi$,$A_\parallel$) depend on the sources, calculated from the distribution function (using these equations of motion), and hence the equation cannot be solved directly.

In the $p_\parallel$ formalism, the equations of motion are as given in Eqns. 3.28 and 3.29:

$$\frac{d\vec{R}}{dt} = \left(v_\parallel - \frac{e}{m_i}\langle A_\parallel\rangle\right)\frac{\vec{B}^*}{B^*_\parallel} + \frac{1}{eB^*_\parallel}\vec{h}\times\left[\mu\nabla B + e\left(\nabla\langle\phi\rangle - v_\parallel\nabla\langle A_\parallel\rangle\right)\right], \tag{4.13a}$$

$$\frac{dv_\parallel}{dt} - \frac{m_i\vec{B}^*}{B^*_\parallel}\cdot\left[\mu\nabla B + e\left(\nabla\langle\phi\rangle - v_\parallel\nabla\langle A_\parallel\rangle\right)\right], \tag{4.13b}$$

and the parallel Ampere's Law is:

$$\sum_\alpha \frac{\beta_s}{\rho_s^2}\langle A_\parallel\rangle - \nabla^2_\perp A_\parallel = \mu_0 \sum_\alpha \frac{p_\parallel}{m}, \tag{4.14}$$

where $\beta_s = \mu_0 n_{0,s} T_{0,s}/B^2$. Note that Eqns. 4.13 no longer have the $\partial\langle A_\parallel\rangle/\partial t$ terms and so explicit time solvers can be used. However, there is now an extra term on the left hand side of the parallel Ampere's Law, Eqn. 4.14. These terms are cancelled by the modification to the right hand side, which now contains $p_{||}$ instead of $v_{||}$.

This term is cancelled by splitting the current into adiabatic and nonadiabatic parts. Consider a Boltzmann-like adiabatic perturbation of the distribution function, associated with the perturbed $p_{||}$ Hamiltonian:

$$\begin{aligned} H_{1,ad} &= e\langle \phi - v_{||}A_{||} \rangle, \\ F_{ad,s} = F_{0,s}e^{-H_{1,ad},T_s} - F_{0,s} &\approx -\frac{eF_{0,s}}{T_s}\langle \phi - v_{||}A_{||} \rangle, \end{aligned} \tag{4.15}$$

for small $v_{||}A_{||}$. This distribution function implies a parallel adiabatic current due to the second term in the perturbed Hamiltonian. This term is present in the $p_{||}$ formalism but not the $v_{||}$ formalism. Thus the parallel adiabatic currents are also unphysical and must be cancelled. This adiabatic current has the same magnitude as the skin terms:

$$\mu_0 j_{||,ad} = \mu_0 e \int v_{||} F_{ad,s} d^3v = \frac{\mu_0 n_{0,s} e^2}{m_s} A_{||} = \frac{\beta_s}{\rho_s^2} A_{||}. \tag{4.16}$$

This term then cancels with the leftmost terms in Eqn. 4.14.

The different methods of discretization means that the cancellation between the first term of the left hand side of Eqn. 4.14 and the adiabatic current term is inexact. Since the approximately cancelling terms are much larger than remaining terms in Eqn. 4.14, this leads to a numerical inaccuracy, referred to as the 'cancellation problem'. The cancellation problem occurs most strongly under certain circumstances. When there are a lower number of particles/markers, the discretization of the distribution function is less exact and so the error is larger. When the toroidal mode number, $N$, is low the instability is less localized to a single flux surface and so again there is a greater amount of interpolation between distribution and field discretization. The ratio of the two terms on the left hand side of Eqn. 4.14 is given by $\frac{\beta_s}{k_\perp^2 \rho_s^2}$ and so therefore for higher $\beta$ simulations the errors caused by the cancellation problem are greater. Finally, when the system size is large $k_\perp \rho$ is smaller for constant $N$. These conditions are seen during the global gyrokinetic simulations of low-$N$ modes, especially at the higher $\beta$ required for kinetic ballooning modes to grow as performed in Chapters 9 and 11.

### 4.6.2 Solutions to the Cancellation Problem

There are several different possible ways to mitigate the cancellation problem. The method implemented in the version of ORB5 used in this thesis involves using a control variates method discretised using a Galerkin method and is further described in Ref. [59] along with results showing its efficiency in the GYGLES code. This method involves solving Eqn. 4.14 to get an approximate value for $A_{\|}$, $A_{\|,approx}$. Then the equation is solved again, but with the second term split as $A_{\|} = A_{\|,approx} + A_{\|,correction}$. This is performed until $A_{\|}$ converges which results in the required cancellation.

Another method of solving the cancellation involves splitting $A_{\|}$ into both a sympletic part and a Hamiltonian part and is further described in Ref. [47] (i.e. only putting part of $A_{\|}$ in Eqn. 4.13). This method was implemented in ORB5 after work had already started for the project and so was not used during this PhD. However, simulations could be run in the future using this method to allow the further reduction of the number of markers and the enlarging of the system size for low-$N$ modes.

# Chapter 5

# Ballooning Mode Theory

A kinetic ballooning mode is a mode that arises from coupling between the pressure gradient and bad magnetic curvature present in a tokamak. The drifts and currents that result in the growth of kinetic ballooning modes are described in Chapter 2. Kinetic ballooning modes only appear beyond a critical-$\beta$. (The $\beta$ value can be used as a substitute for the pedestal pressure gradient, since, for a fixed pedestal width, a given $\beta$ or pedestal height gives a specific pedestal pressure gradient.) Since the growth rate of kinetic ballooning modes increases greatly as $\beta$ increases (near the critical-$\beta$), they are thought to provide a limit on the maximum pressure gradient that a pedestal can achieve. This is useful for predicting the properties of the pressure profile in the pedestal region.

In this chapter, local gyrokinetic assumptions are used and so $\vec{k}_{\|}$ is small compared to the $\vec{k}_{\perp}$, meaning that the mode is localized perpendicular to the magnetic field, but is not parallel to the magnetic field. The kinetic ballooning mode equation, derived in this section, therefore shows the dispersion relation for this mode along the field line.

This equation is then compared to the ideal-MHD ballooning equation to see what differences are expected in later simulations, Chapters 9 and 11, for the change in growth rates.

## 5.1 Ballooning Description

In order to apply the gyrokinetic equation to a tokamak, first the equation must be calculated in toroidal geometry using straight field line magnetic coordinates. Since

$\chi$ is the straight field line angle-like coordinate, all quantities must be periodic in $\chi$, as they are in $\phi$, such that $f(\chi) = f(\chi + 2\pi)$. The issue arises when trying to reconcile the periodicity in both $\chi$ and $\phi$ with using a plane wave description in the radial and toroidal coordinates. Several attempts to reconcile these properties have been made [60] [61], but these were partially successful as they lead to the introduction of an arbitrary function in the eikonal representation, but without defining the function. The way to proceed is to use the ballooning representation (usable for both MHD and kinetic ballooning modes, which both struggle with the above problem) [62], where for all perturbed quantities:

$$\Phi(\psi, \chi, \phi, t) = \sum_{p=-\infty}^{\infty} \bar{\Phi}(\psi, \chi - 2\pi p, \phi, t). \tag{5.1}$$

Note that although $\bar{\Phi}$ extends from $-\infty$ to $\infty$ in $\chi$ and is not necessarily periodic, the infinite sum is. To ensure that the sum converges, $\bar{\Phi}$ must vanish sufficiently fast as $\chi \to \pm\infty$.

Note that the superposition principle states that if $\mathcal{L}$ is a linear operator, then $\mathcal{L}\Phi = \mathcal{L}\left(\sum_{p=-\infty}^{\infty} \bar{\Phi}(\psi, \chi - 2\pi p, \phi, t)\right) = \sum_{p=-\infty}^{\infty} \mathcal{L}\bar{\Phi}(\psi, \chi - 2\pi p, \phi, t)$. Therefore, if $\mathcal{L}\bar{\Phi} = 0$ for all $\bar{\Phi}$, then $\mathcal{L}\Phi = 0$. Therefore, the problem changes from solving the perturbed quantities with periodicity to solving the perturbed quantities over an infinite range in $\chi$ with no periodicity constraint.

The perturbations of interest are characterized by short perpendicular, $k_\perp \rho_i \sim 1$, and long parallel, $k_\parallel \rho_i \sim \epsilon$ wavelengths. Hence, it is possible to adopt an eikonal representation, which involves making an educated guess for the solution of a differential equation of the form $\epsilon \frac{d^2 y}{dx^2} = Q(x) y$ as $y = A(x) e^{\pm i S(x)/\epsilon}$ with $S(x) = \pm \int_{x_0}^{x} \sqrt{Q(x')}$ and $A(x) = C/\sqrt{Q(x)}$. In this case the parameters can be written using the eikonal representation:

$$\begin{pmatrix} \delta \bar{f} \\ \bar{\Phi} \\ \vec{\bar{A}} \end{pmatrix} = \begin{pmatrix} \delta \hat{f} \\ \hat{\Phi} \\ \vec{\hat{A}} \end{pmatrix} \exp(iS(\chi, \phi)/\epsilon) \exp(-i\omega t) \tag{5.2}$$

where $S$ is the eikonal accounting for the rapid cross-field variations. In this case the specific form of $S$ is determined by the requirement $k_\parallel \rho_i \sim \epsilon$. Therefore

$$\vec{h} \cdot \nabla S = 0, \tag{5.3}$$

with $\vec{h} \equiv \frac{\vec{B}}{B}$. Using the gradient operator and Eqn. 2.8 and the fact that all perturbations can be Fourier-decomposed in the ignorable coordinate $\phi$, Eqn. 5.3 gives

$$\frac{1}{BJ}\left(\frac{\partial}{\partial\chi} + iN\frac{IJ}{R^2}\right) S = 0, \tag{5.4}$$

with $N$ being the toroidal mode number. The most general form of $S$ is then

$$S = \left[\phi - \int_0^{\chi} d\chi' \frac{IJ}{R^2} + \int^{\psi} k(\psi) d\psi\right], \tag{5.5}$$

with $k(\psi)$ being determined separately [63].

## 5.2 Linearised gyrokinetic equation

The linearised local gyrokinetic equation is derived from the gyrokinetic Vlasov equation. This results in Eqn. 50 of Ref. [19], where the distribution function is given as a perturbed and unperturbed equilibrium part, $\delta f$ and $F$. In this section the equation for electrons will be considered.

This equation is then written in terms of straight field line coordinates [19] [64], by using Eqns. 2.6 and 2.7 and the ballooning representation. The terms of similar order are subsequently collected.

The lowest order terms give:

$$\delta\hat{f} = \hat{g}\exp(-iL) + \frac{Zef_0}{T}\Phi \tag{5.6}$$

where $L \equiv \frac{kv_\perp}{\Omega}$ and the adiabatic part of the perturbed distribution function is separated (the second term on the right hand side). The next order equation, then provides the electron linearised gyrokinetic equation (equation 2.17 in Ref. [28]) [64] [19]:

$$\begin{aligned} \frac{v_\parallel}{JB}\frac{\partial}{\partial\chi}\hat{g} - i\hat{g}\left(\omega - \vec{k}_\perp \cdot \vec{v}_D\right) &= -\frac{-ie}{T} f_0 \left(\omega - \omega_*^T\right) \\ &\times \left[J_0(\alpha)\left(\hat{\Phi} - v_\parallel \hat{A}_\parallel\right) + J_1(\alpha)\frac{v_\perp}{k_\perp}\delta B_\parallel\right], \end{aligned} \tag{5.7}$$

where $\vec{v}_D = \frac{1}{\Omega}\vec{h} \times \left(\mu\nabla B + v_\parallel^2 \vec{h} \cdot \nabla h\right)$, $\omega_*^T = \omega_{*p}\left[1 + \eta\left(\frac{mE}{T} - \frac{3}{2}\right)\right]$ with $\eta = \frac{d\ln T}{d\ln n_0}$ and the diamagnetic frequency $\omega_{*p} = \frac{nT}{e}\frac{d}{d\psi}\ln n_0$, $J$ are Bessel functions and $\alpha = \frac{k_\perp}{v_\perp}\Omega$. Note that, in future equations, all Bessel functions are functions of $\alpha$. The boundary for Eqn. 5.7 is

$$\hat{g} \to 0 \text{ as } \chi \to \pm\infty$$

for circulating particles and the forward and backward stream of particles match at the turning points for trapped particles.

The usual procedure for solving Eqn. 5.7 is to use an integrating factor of the form

$$I_b^a = \int_a^b d\chi' \left(\omega - \omega_D\right) \frac{JB}{|v_\parallel|} \tag{5.8}$$

with $\omega_D \equiv \vec{k}_\perp \cdot \vec{v}_D$. The general solution is then given by

$$\hat{g}_\pm(\chi) = \mp \frac{ie}{T} f_0 \left(\omega - \omega_*^T\right) \int_{\mp\infty}^{\chi} d\chi' \left(\frac{JB}{|v_\parallel|}\right) \exp\left(\mp i I_\chi^{\chi'}\right)$$

$$\times \left[J_0(\alpha)\left(\hat{\Phi} \mp |v_\parallel| \hat{A}_\parallel\right) + J_1(\alpha)\frac{v_\perp}{k_\perp}\delta\hat{B}_\parallel\right]. \tag{5.9}$$

## 5.3 Kinetic ballooning mode theory

The solution to the linearised gyrokinetic equation provided in Eqn. 5.9 can then be inserted into three different equations to derive an overall equation for KBMs.

The first of these equations is the quasi-neutrality equation. This results in

$$0 = \sum_\alpha \frac{n_0 q_\alpha^2}{T_\alpha}\hat{\Phi} + \sum_\alpha \frac{q}{\epsilon_0}\int dE d\mu \frac{B}{|v_\parallel|}\left(\hat{g}_+ + \hat{g}_-\right) J_0(\alpha) \tag{5.10}$$

where the summation is over particle species.

The second equation is the parallel current equation, the component of Ampere's Law parallel to the magnetic field:

$$k_\perp^2 \hat{A}_\parallel = \frac{1}{\mu_0}\hat{j}_\parallel, \tag{5.11}$$

where $\hat{j}_\parallel$ is a function of $\hat{g}_\pm$.

The final equation is the radial current equation, one of the two perpendicular components of Ampere's Law:

$$\delta\hat{B}_{\|} = -\frac{1}{k_\perp \mu_0}\sum_\alpha \frac{q}{\epsilon_0}\int dE d\mu \frac{B}{|v_\||} v_\perp \left(\hat{g}_+ - \hat{g}_-\right) J_1(\alpha). \tag{5.12}$$

In order to simplify and combine these equations to derive an equation describing kinetic ballooning modes, a low-frequency mode limit, where the mode frequencies are taken to be much lower than the transit and bounce frequencies of both electrons and ions, is taken. In Ref. [28], a different regime is also shown, where the frequency is between the electron and ion transit frequencies. However, this regime, although more applicable to modes studied in Chapters 9 and 11, is more complicated and has similar comparisons with the equivalent MHD ballooning equation.

In the low-frequency limit, $\omega \ll \omega_b, \omega_t \approx v_T/L_c$ where $v_T$ is the thermal velocity and $L_c$ is the connection length, and so $\omega L_c/v_T$ can be used as a small parameter. In lowest order, the solution of the linearised gyrokinetic equation, Eqn. 5.7, for circulating particles reduces as

$$\frac{1}{2}\left(\hat{g}_+ + \hat{g}_-\right) = \frac{q}{T} f_0 \left(1 - \frac{\omega_*^T}{\omega}\right)\hat{\psi}_\| \tag{5.13}$$

where $\hat{\psi}_\| = \frac{i\omega}{2}\left[\int_{-\infty}^{\chi} d\chi' JB\hat{A}_\| - \int_{\chi}^{\infty} d\chi' JB\hat{A}_\|\right]$.

Then the derived kinetic ballooning mode equation, ignoring trapped particles, is

$$\frac{L_c^2}{JB^2}\frac{\partial}{\partial\chi}\left(\frac{b}{J}\frac{\partial}{\partial\chi}\hat{\psi}_\|\right) + \left(\frac{\omega}{\omega_A}\right)^2 \left\{\frac{\omega_{*p}\left(\omega_K + \omega_B\right)}{\omega^2}\hat{\psi}_\| + \frac{\omega_{*p}}{\omega}\delta\tilde{B}_\| + \left[1 - \frac{\omega_{*i}(1+\eta_i)}{\omega}\right] b\hat{\phi}\right\} = 0 \tag{5.14}$$

where $b = k_\perp^2\rho_i^2/2$, $\omega_K = (\vec{h}\times(\vec{h}\cdot\nabla\vec{h})\vec{k}_\perp)(T/m\Omega)_i$ and $\omega_B = (\vec{h}\times\nabla B\cdot\vec{k}_\perp)(T/m\Omega B)_i$ are frequencies associated with the curvature and grad-B drifts respectively, $\tilde{B}_\| = \frac{T_i}{m_i\Omega_i}\delta\hat{B}_\|$ and $\omega_A^2 = v_A^2/L_c^2$ is the Alfven frequency, where $v_A = B^2/\mu_0 n_0 m_i$ is the Alfven velocity.

The radial current equation can then be simplified by taking $\beta$ as an expansion parameter [65]. Then the perturbed parallel magnetic field component, ignoring trapped particles, is given by

$$\delta\tilde{B}_\| = \frac{\omega_K - \omega_B}{\omega}\hat{\psi}_\|. \tag{5.15}$$

This means, when $\delta B_{\|}$ effects are included, the kinetic ballooning mode equation (ignoring trapped particles) is given by

$$\frac{L_c^2}{JB^2}\frac{\partial}{\partial\chi}\left(\frac{b}{J}\frac{\partial}{\partial\chi}\hat{\psi}_{\|}\right)+\left(\frac{\omega}{\omega_A}\right)^2\left\{2\frac{\omega_{*p}\omega_K}{\omega^2}\hat{\psi}_{\|}+\left[1-\frac{\omega_{*i}(1+\eta_i)}{\omega}\right]b\hat{\phi}\right\}=0. \quad (5.16)$$

This same equation can be derived, by taking a high-$\beta$ expansion of the linearised gyrokinetic equation, Eqn. 5.7, instead of solely the equation for $\delta\tilde{B}_{\|}$.

## 5.4 Comparison with MHD

Eqn. 5.16 is the ideal-MHD ballooning equation [66] [67], except with a diamagnetic drift. The first term is due to field line bending, the second term is due to curvature and the final term, which is zero in the MHD limit, is the diamagnetic drift correction.

The MHD equation can therefore be recovered, by taking $\omega_{MHD}^2 = \omega(\omega-\omega_*)$. Therefore the local gyrokinetic growth rate can be estimated by taking the MHD $N \to \infty$ growth rate [68] and applying the above formula. This will be shown by the simulations in Chapter 9. Other kinetic effects do not appear to have a large effect on the observed growth rates.

# Chapter 6

# MHD Equations and the Energy Principle

MHD is one of the simplest models for describing the interactions between a conducting fluid and a magnetic field. Ideal MHD is the simplest form of MHD and is applicable under the following circumstances:

- The plasma is strongly collisional and so the particle distributions are close to a Maxwellian.
- Resistivity is small.
- Length scales are much longer than the ion skin depth and the Larmor radius.
- Time scales longer than the ion cyclotron period.
- The plasma must move at speeds much lower than the speed of light (non-relativistic).

MHD was first mentioned in 1942 [69], and is the most understood theory describing plasmas. Therefore, in this thesis, ORB5 simulations, see Chapter 4, are compared to MHD simulations in the appropriate limits. In this chapter, the ideal MHD equations will be shown and the Energy Principle, used in the MHD code MISHKA, will be derived.

## 6.1 Moments of the Vlasov Equation

The MHD equations can be derived from the Vlasov equation by taking velocity moments [70] for each species and then summing the equations together to describe the whole system as a single fluid. The different moments produce the different equations of MHD. Take the Vlasov equation for generic coordinates:

$$\frac{\partial f}{\partial t} + \vec{v} \cdot \nabla f + \left[\frac{q}{m}\left(\vec{E} + \vec{v} \times \vec{B}\right)\right] \cdot \nabla_v f = 0. \tag{6.1}$$

Since the coordinates are taken to be independent of each other then the Vlasov equation can be rewritten in the following way:

$$\frac{\partial f}{\partial t} + \nabla \cdot (\vec{v} f) + \nabla_v \cdot \left(\left[\frac{q}{m}\left(\vec{E} + \vec{v} \times \vec{B}\right)\right] f\right) = 0. \tag{6.2}$$

Take the first moment of the distribution function, Eqn. 6.2,

$$\int d^3v \left[\frac{\partial f}{\partial t} + \nabla \cdot (\vec{v} f) + \nabla_v \cdot \left(\left[\frac{q}{m}\left(\vec{E} + \vec{v} \times \vec{B}\right)\right] f\right)\right] =$$

$$\frac{\partial n}{\partial t} + \nabla \cdot (n\vec{V}) = 0, \tag{6.3}$$

where $n = \int d^3v f$, $n\vec{V} = \int d^3v \vec{v} f$ and $\int d^3v \nabla_v \cdot \left(\left[\frac{q}{m}\left(\vec{E} + \vec{v} \times \vec{B}\right)\right] f\right) = 0$ since the integral is over the total volume of the plasma. This is the continuity equation and states that the density is constant if the plasma is non-compressional.

The second moment of the Vlasov equation, multiplied by the mass, produces Newton's 2nd Law:

$$\int d^3v m\vec{v} \left[\frac{\partial f}{\partial t} + \nabla \cdot (\vec{v} f) + \nabla_v \cdot \left(\left[\frac{q_\alpha}{m_\alpha}\left(\vec{E} + \vec{v} \times \vec{B}\right)\right] f\right)\right] =$$

$$\int d^3v \vec{v} \left[m\frac{\partial \vec{v} f}{\partial t} + m\nabla \cdot (\vec{v}\vec{v} f) + m\vec{v}\nabla_v \cdot \left(\left[\frac{q}{m}\left(\vec{E} + \vec{v} \times \vec{B}\right)\right] f\right)\right] =$$

$$m\frac{\partial n\vec{V}}{\partial t} + m\nabla \cdot \left(n\vec{V}\vec{V} + \frac{\vec{P}}{mn}\right) - qn\left(\vec{E} + \vec{V} \times \vec{B}\right) = 0, \tag{6.4}$$

where $\vec{P} = \int d^3v \left[\vec{v} - \vec{V}\right]\left[\vec{v} - \vec{V}\right] f$ is the pressure tensor, given as $P\vec{I}$ for an isotropic pressure.

The third moment can be calculated in the same way, but each moment introduces a new variable into the set of equations and so this method cannot solely produce a closed set of equations. Normally a different equation is used for the evolution of the pressure and Maxwell's equations are used for the evolution of the electromagnetic fields.

## 6.2 Ideal MHD equations

The ideal MHD equations are as follows [71]

$$\rho \frac{d\vec{v}}{dt} = -\nabla p + \vec{J} \times \vec{B}, \tag{6.5}$$

$$\vec{J} = \frac{1}{\mu} \nabla \times \vec{B}, \tag{6.6}$$

$$\frac{\partial}{\partial t} \vec{B} = -\nabla \times \vec{E}, \tag{6.7}$$

$$\vec{E} = -\vec{v} \times \vec{B}, \tag{6.8}$$

$$\frac{\partial}{\partial t} p = -\vec{v} \cdot \nabla p - \Gamma p \nabla \cdot \vec{v}, \tag{6.9}$$

$$\frac{\partial}{\partial t} \rho = -\vec{v} \cdot \nabla \rho - \rho \nabla \cdot \vec{v}, \tag{6.10}$$

where $\vec{v}$ is the macroscopic fluid velocity, $\vec{B}$ is the magnetic field, $p$ is the pressure and $\rho$ is the mass density. These four variables describe the state of the system and the MHD equations describe how these variables evolve with time. $\Gamma = 5/3$ is the ratio of specific heats for an ideal gas with three degrees of freedom.

Eqn. 6.5 represents the acceleration of the fluid due to local forces and is Newton's second law $ma = F$ and is derived from the 2nd moment of the Vlasov equation, Eqn. 6.4. The first term on the right hand side is the force resulting from a difference in pressure on opposite sides of the fluid element. The second term on the right hand side is the Lorentz force, summed over all the particles in the fluid element.

Eqn. 6.6 is Ampere's Law, with the displacement current neglected. This magnetostatic assumption is valid if the Alfven velocity $v_A = B/(\mu_0 \rho)^{1/2}$ is much lower than the speed of light [72].

Eqn. 6.7 is Faraday's Law for the evolution of the magnetic field. Eqn. 6.8 is the ideal MHD Ohm's Law and is derived from the Galilean invariance of Faraday's Law and the assumption that the electric field moving with the plasma is zero.

The motion of the plasma changes the magnetic field from Faraday's Law, Eqn. 6.7, and Ohm's Law, Eqn. 6.8. Meanwhile, the magnetic field then acts on the motion of the plasma through Eqn. 6.6 and Eqn. 6.5.

The evolution of the pressure and density are given by the thermodynamic equations 6.9 and 6.10. The first term on the right hand side of each of these equations shows the effect of convection. If only these terms were present, then the pressure and density of the fluid element would not change over time. The second term on the right hand side of each of these equations represents the compression and expansion of the pressure and density of the fluid element. The density evolution is derived from Eqn. 6.3, the first moment of the Vlasov equation.

There are a couple of boundary conditions necessary for conservation of some important quantities. For instance, conservation of mass means that there must be no fluid velocity across the boundary of the simulation:

$$\vec{v}_\perp = 0. \tag{6.11}$$

In order to conserve energy the Poynting flux [73] (directional energy flux) must be zero at the boundary so:

$$(\vec{E} \times \vec{B})_\perp = 0. \tag{6.12}$$

To conserve magnetic flux, then the parallel electric field at the boundary must be zero:

$$E_\parallel = 0. \tag{6.13}$$

## 6.3 Linearised MHD equations

To create the linearised MHD equations, all the parameters are written in terms of equilibrium quantities, which have no time dependence, (denoted by a subscript 0) and perturbed quantities (denoted by a subscript 1) multiplied by a small parameter $\epsilon_{MHD} \ll 1$:

$$\vec{v} = \vec{v}_0 + \epsilon_{MHD}\vec{v}_1 = \epsilon_{MHD}\vec{v}_1, \tag{6.14a}$$

$$\vec{B} = \vec{B}_0 + \epsilon_{MHD}\vec{B}_1, \tag{6.14b}$$

$$p = p_0 + \epsilon_{MHD}p_1, \tag{6.14c}$$

$$\rho = \rho_0 + \epsilon_{MHD}\rho_1, \tag{6.14d}$$

where $\vec{v}_0 = 0$ since $(\partial/\partial t)_0 = 0$ and $\vec{v} = \partial \vec{x}/\partial t$. The time independence of the equilibrium quantities and Eqn. 6.5 also leads to the force balance equation:

$$\nabla p_0 = \vec{J}_0 \times \vec{B}_0. \tag{6.15}$$

Keeping the terms at first order give the linearised MHD equations:

$$\rho_0 \frac{\partial \vec{v}_1}{\partial t} = -\nabla p_1 + \vec{J}_0 \times \vec{B}_1 + \vec{J}_1 \times \vec{B}_0, \tag{6.16}$$

from Eqn. 6.5 and Eqn. 6.6 where $\vec{J}_0 = \frac{1}{\mu}\nabla \times \vec{B}_0$ and $\vec{J}_1 = \frac{1}{\mu}\nabla \times \vec{B}_1$,

$$\frac{\partial \vec{B}_1}{\partial t} = \nabla \times \left(\vec{v}_1 \times \vec{B}_0\right) \tag{6.17}$$

$$\frac{\partial p_1}{\partial t} = -\vec{v}_1 \cdot \nabla p_0 - \Gamma p_0 \nabla \cdot \vec{v}_1. \tag{6.18}$$

Note that the equations governing the evolution of the perturbed density is not necessary, as the perturbed density does not appear in any of the other equations, since $\vec{v}_0 = 0$.

Then all perturbed quantities are written as exponentials in time: $v_1 = v_1(x)\exp(-\omega t)$, which removes time derivatives and allows for the calculation of growth rates.

## 6.4 Displacement Vector $\vec{\xi}$

It is useful to write the linearised MHD equations in terms of the displacement vector

$$\vec{\xi}(\vec{x}, t) = \int_o^t \vec{v}_1(\vec{x}, t^{'})dt^{'}. \tag{6.19}$$

Eqns. 6.17 and 6.18 can be integrated to give

$$\vec{B}_1(\vec{x}, t) = \nabla \times (\vec{\xi} \times \vec{B}_0) \tag{6.20}$$

$$p_1(\vec{x}, t) = -\vec{\xi} \cdot \nabla p_0 - \Gamma p_0 \nabla \cdot \vec{\xi} \tag{6.21}$$

The constants of integration can be eliminated by the choice of initial conditions.

Eqn. 6.16 can then be combined with Eqns. 6.20 and 6.21 to give

$$\rho_0 \frac{\partial^2 \vec{\xi}}{\partial t^2} = \vec{F}(\vec{\xi}) = \nabla(\vec{\xi} \cdot \nabla p_0 + \Gamma p_0 \nabla \cdot \vec{\xi}) +$$

$$\frac{1}{\mu}(\nabla \times \vec{B}_0) \times [\nabla \times (\vec{\xi} \times \vec{B}_0)] + \frac{1}{\mu}(\nabla \times [\nabla \times (\vec{\xi} \times \vec{B}_0)]) \times \vec{B}_0. \tag{6.22}$$

The boundary condition can then either be $\vec{\xi}_\perp = 0$ on the last magnetic flux surface around the plasma, or a vacuum region with a perfectly conducting outer wall.

## 6.5 The Energy Principle

The Energy Principle is a useful tool for determining the stability of an MHD plasma. The first step of the derivation is to multiply Eqn. 6.22 by the time derivative of $\vec{\xi}$ and integrate over the volume of the plasma:

$$\int d^3x \rho_0 \frac{\partial \vec{\xi}}{\partial t} \cdot \frac{\partial^2 \vec{\xi}}{\partial t^2} = \frac{\partial}{\partial t} \int d^3x \frac{1}{2} \rho_0 \left( \frac{\partial \vec{\xi}}{\partial t} \right)^2 = \int d^3x \frac{\partial \vec{\xi}}{\partial t} \cdot \vec{F}(\vec{\xi}). \tag{6.23}$$

Ref. [74] gives the steps from Eqn. 6.23 to

$$\frac{\partial}{\partial t} \left[ \int d^3x \frac{1}{2} \rho_0 \left( \frac{\partial \vec{\xi}}{\partial t} \right)^2 - \frac{1}{2} \int d^3x \vec{\xi} \cdot \vec{F}(\vec{\xi}) \right] = 0. \tag{6.24}$$

The first term within the bracket of the left hand side of Eqn. 6.24 is the total perturbed kinetic energy and the second term is the total perturbed potential energy $\delta W = \frac{1}{2} \int d^3x \vec{\xi} \cdot \vec{F}(\vec{\xi})$ and so Eqn. 6.24 states that the total perturbed energy is constant in time. Since $\xi(\vec{x}, t) = \xi(\vec{x}) \exp(-\omega t)$, the time derivatives can be simplified and only $\xi(\vec{x})$ needs to be solved for.

It can be seen from the conservation of total perturbed energy, that if an instability is to grow the kinetic energy must increase and hence the potential energy must decrease. This is the energy principle, where the potential energy of the system with a given perturbation will decrease and hence whether the system is unstable. If all possible perturbations lead to an increase in the potential energy, then the system is stable.

The energy principle can be written in more useful forms. In Ref. [72], it is shown that $\delta W = \delta W_F + \delta W_V + \delta W_S$ where $\delta W_V$ is the potential energy in the vacuum region surrounding the plasma, $\delta W_S$ is the integral over the surface of the plasma and $\delta W_F$ is the potential within the plasma. Then $\delta W_F$ can be written in the following form:

$$\delta W_F = +\frac{1}{2}\int_{plasma} d^3x \Bigg\{ \frac{1}{\mu_0}|B_\perp^1|^2 + \mu_0 \left| \frac{1}{\mu_0}B_\parallel^1 - B^0\xi \cdot \nabla p^0/|B^0|^2 \right|^2$$
$$+\Gamma p^0 |\nabla \cdot \xi|^2 + \frac{J_0 \cdot B_0}{|B^0|^2} B^0 \times \xi \cdot B^1 - 2\xi \cdot \nabla p^0 \xi \cdot \kappa \Bigg\}, \tag{6.25}$$

The first three terms within the integral represent the potential energy in several different stabilising effects, including field line bending and plasma compression. These are effects that instabilities have to overcome in order to start growing. The fourth term can drive kink instabilities, or current driven instabilities, when it is negative. The final term in the integral is the most important for this thesis and can drive interchange or ballooning instabilities, instabilities driven by the pressure gradient and/or curvature.

## Chapter 7

# The MHD and Drift Models.: A comparison in Z-pinch cylindrical geometry

In order to visually understand ballooning mode mechanics and understand the forces that drive this instability, the ballooning instability is first considered in a simple geometry, a Z-pinch.

## 7.1 Force Comparison

Consider a Z-pinch (where the equilibrium current runs along the Z-direction) which is axisymmetric about the Z-axis. The background field is then given by $\overline{B_0} = B(R)\hat{\phi}$, where $\hat{\phi}$ is the angle coordinate, and the pressure is given by $p = p_0(R)$. In an MHD equilibrium, force balance is given by $0 = \overline{J_0} \times \overline{B_0} - \nabla p_0$, which in a Z-pinch is then given by $\hat{R}(-J_0 B_0 - \partial_R p_0) = 0$. Since $\mu_0 \overline{J_0} = \nabla \times \overline{B_0}$, then $\overline{J_0} = \hat{Z}(\mu R)^{-1}\partial_R(RB_0)$.

Assume that a region of increased pressure is introduced into the plasma as shown in Fig. 7.1. In order to retain axisymmetry, this region of increased pressure will be assumed to be a solid of rotation, which leads to the magnetic field still being solely in the $\hat{\phi}$-direction. However, there is now a variation in the Z-direction. This leads to an imbalance in the forces and as such, in MHD theory, the region of increased pressure is expected to expand so the pressure inside and outside the region balance. This expansion leads to a modification of the magnetic field and the potential to further motion due to the resulting magnetic forces.

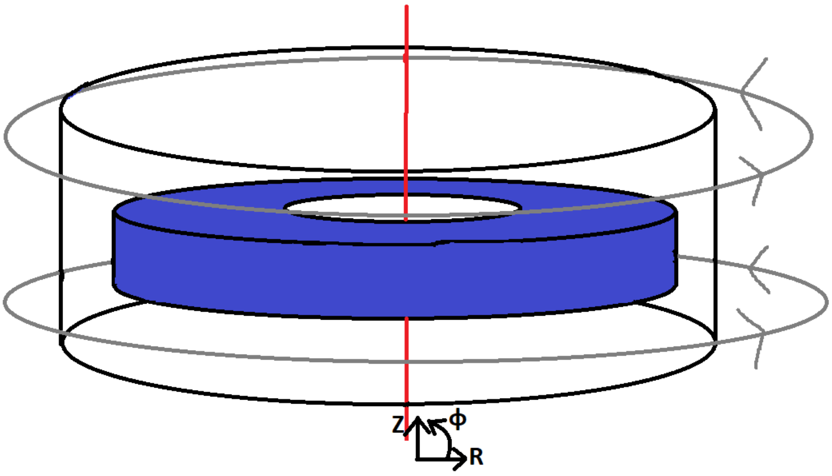

Figure 7.1: Z-pinch, with the region of increased pressure shown in blue. The red line is the axis of the cylinder and the grey lines represent the magnetic field $\overline{B_0} = B(R)\hat{\phi}$.

This motion may be complicated. However, the assumption will be made that the high pressure region is elongated in the R-direction, as seen in a finger of Rayleigh-Taylor instability or a ballooning perturbation, which leads to the pressure being balanced more rapidly in the Z-direction than in the R-direction. In this geometry, the curvature forces only act in the R-direction, so force balance requires that $B_0^2 = B_1^2 + 2\mu_0 p_1$, with $p_1$ being the pressure in the higher pressure region (now expanded slightly) an $B_1$ is the magnetic field in the higher pressure region.

This results in force balance in the Z-direction, but not in the R-direction. The radial component of the force can be calculated from the elements of the force balance equation, $\overline{F}.\hat{R} = -\partial_R(p_0+p_1)-B_1(\mu_0 R)^{-1}\partial_R(RB_1) = -\partial_R p_1-(\mu_0)^{-1}(B_1^2/R+\partial_R B_1^2/2) = 2p_1/R$. This is a classic curvature-driven Buoyancy force, similar to a Rayleigh-Bernard convection, but with pressure replacing gravity. Note that this force does not depend on the background magnetic or plasma pressure. Proof that interchange instabilities are driven by only the currents that result from curvature is given for more general geometries in textbooks on MHD theory [75] from the energy principle.

Now consider the same situation, but using the gyrokinetic drift model. Currently in ORB5, electromagnetic fluctuations are only allowed via $A_{\|}$. This means that there are only $B_\perp$ fluctuations and hence $\delta B_\parallel = 0$. Therefore, the perturbed $J \times B$ force is given by $\delta(J \times B) = \delta J \times B + J \times \delta B_\perp$. Therefore, since the system is axisymmetric (the magnetic field is solely in the poloidal direction) and that the perturbation is in the R-direction, no field line bending is expected so $\delta B_\perp = 0$ and the dynamics are purely electrostatic and depend solely on $\delta J_\perp$. This is unexpected as MHD requires perturbed magnetic fields in order for a perturbed $J \times B$ force to arise, but the electromagnetic forces still arise in drift models without perturbed magnetic fields due to the rise of currents from the drift motions. The drift motion and polarisation equation can be seen as a consequence of force balance: a gyrokinetic plasma is automatically in perpendicular force balance on gyration time scales, but can have acceleration arise on longer time scales as the electric fields build up.

By quasi-neutrality, $\nabla \cdot J = 0$ and so $\partial J_z/\partial z = 0$. Since $J_z = 0$ outside the region of increased pressure, then $J_z = 0$ within the region of increased pressure. Therefore, the perturbed drift currents $J = e(n_0 + n_1)(v_{\nabla B} + v_{B\times\nabla B})$, summed over electrons and ions, must be balanced by the current due to the polarisation drift $v_p = \partial_t E/B\Omega_i$ and so the resulting electric field is given by $n_0 e \partial_t E = -\Omega_i B(n_0+n_1)(v_{\nabla B}+v_{B\times\nabla B})$. This polarization drift, separates positive and negative charges perpendicular to the magnetic field and hence creates an electric field. The resulting $E \times B$ drift is given by $\partial_t v_E = -\Omega_i \tilde{J}/en_0$. Since the $E \times B$ drift is in the radial direction, by inserting the definition of the curvature and grad-B drifts into the current term, an effective radial force can be found:

$$\overline{F}.\hat{R} =< nv_\perp^2 > \frac{\nabla\overline{B}}{2qB^2} + < nv_\parallel^2 > \frac{\overline{B}.\nabla\overline{B}}{qB^2} \tag{7.1}$$

and assuming an isotropic background plasma

$$\overline{F} \cdot \hat{R} = p_1 \left( \frac{\nabla\overline{B}}{qB^2} + \frac{\overline{B}.\nabla\overline{B}}{qB^2} \right). \tag{7.2}$$

This mechanism is shown in Fig. 7.2. This force is charge independent and hence all charged species are expelled from the core of the plasma.

Note that for a $\beta = 0$ plasma , $v_{\nabla B}$ can be rewritten. This is due to Ampere's Law and that $\hat{J} \times \hat{B} = 0$, $\nabla \times B = 0$. In cylindrical coordinates, with $\phi$ being the angle coordinate, this means that $\nabla \times B = \frac{1}{R}\frac{\partial}{\partial R} B_\phi \hat{z}$. Since $RB_\phi$ is constant, that means that $\nabla B = B\frac{\vec{r_C}}{r_C^2}$. Hence the $\nabla B$ and curvature drifts can be written in an equivalent form and therefore $\vec{F}.\hat{R} = 2p_1/R$, which is equivalent in the MHD model. However, if this is not the case, then the MHD and gyrokinetic models differ, as is the case for gyrokinetic codes such as ORB5, where a $A_{||}$ formalism is used. Note that if the $\nabla B$ drift is replaced with the curvature drift, then this difference disappears and the MHD and gyrokinetic results match again in a $\beta \neq 0$ plasma.

This difference is unexpected, as we expect to recover MHD in the fluid limit. The most obvious point of disagreement is in the variation of the magnetic field amplitude that arises in the MHD model, whereas in the gyrokinetic $A_{||}$ formulation this is neglected. Therefore, any forces arising from the $J_0 \times B_1$ are neglected in the $A_{||}$ model. The perturbed parallel field in the expression for drifts is needed to correctly predict the force acting on a blob of plasma, and this directly leads to incorrect growth rates.

## 7.2 MHD Energy Principle

If there is a perturbation allowing the sum of the terms in Eqn. 6.25 to be negative, then there must be an instability. However, the solution minimising the energy may not be a solution of the linearised local MHD eigenfrequency equation. Nevertheless, it is common to use the estimate $-\omega^2 = 2\delta W_F / \int d^3x\rho\zeta^2$, with $\zeta$ given by the perturbation that minimises the energy equation.

For ballooning type perturbations, the destabilising term is the final term on the right hand side of Eqn. 6.25. Assuming that all the stabilising terms can be ignored, the growth rate estimate is then given by

$$\omega^2 = \frac{2\int \zeta.\nabla p^0 \zeta.\kappa}{\int \rho\zeta^2} \tag{7.3}$$

which for uniform density, curvature and pressure gradient, results in $\gamma = (2\nabla p_0.\kappa/\rho)^{1/2}$ for an optimally aligned mode. This can be viewed as the curvature drive strength in the absence of stabilising effects. This is in agreement with the analysis provided earlier for the Z-pinch, with $\kappa = 1/R$, which is approximately correct for a tokamak. Note that because of the helical field lines in a tokamak, the stabilising terms become more important, due to the field line bending. Hence the minimisation of the energy equation becomes a race between the curvature drive (destabilising) and field line bending (stabilising).

## 7.3 $\delta B_{\|}$ effects

In the drift theory, perturbed currents in the plasma arise due to drifts, flow along the field lines and as a magnetisation current, due to gyration. The quasi-neutrality equation, equation 2.31 from Ref. [28], arises from the fact that the divergence of the currents in the plasma is zero. When $\delta B_{\|}$ is neglected in gyrokinetics, the magnetisation currents do not play an explicit role as they do not lead to parallel currents and therefore they do not modify the quasi-neutrality equation as their divergence is equal to zero. However, the magnetisation current is still crucial for calculating the perturbed current distribution, as it modifies $\delta B$, leading to a $J \times \delta B$ force, and hence the $J \times B$ force when $\beta \neq 0$. This is the reason that electromagnetic forces arise even where the polarisation current cancels the perpendicular current as happens when $\delta B_{\|}$ is neglected.

However, when $\delta B_{\|}$ is present, then electromagnetic forces arise from the interaction with the parallel perturbed magnetic field and perpendicular currents.

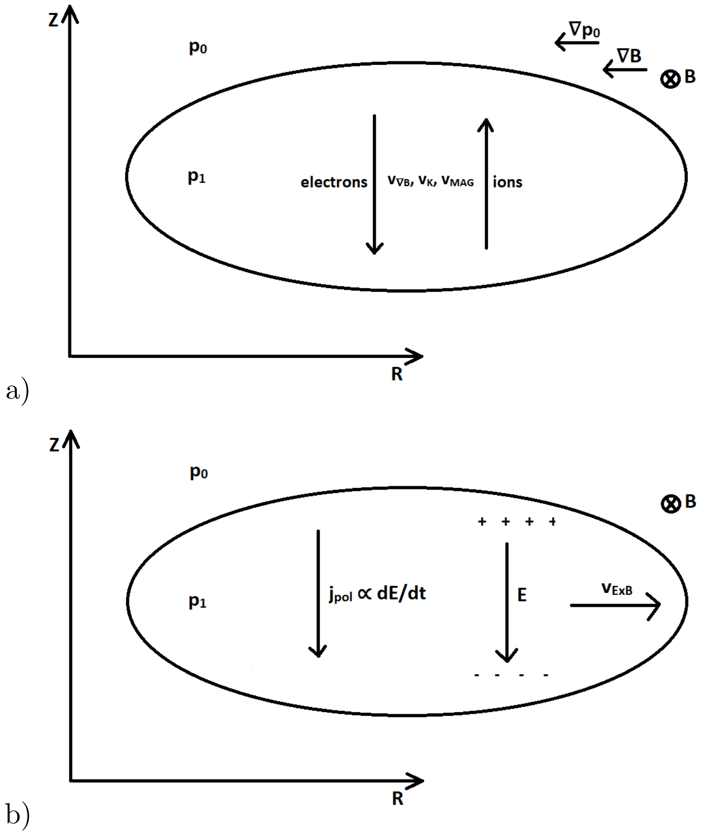

Figure 7.2: Mechanism of the kinetic ballooning mode in a Z-pinch using drift kinetic theory. The oval region represents the region of increased pressure as shown in Fig. 7.1, in the $R$-$Z$ plane. Firstly, the $\nabla B$, curvature and magnetisation drift create a current due to the opposite movement of electrons and ions. This creates an electric field that then results in an $E \times B$ drift which is charge independent and is orientated in the $R$ direction as shown. The acceleration, and hence the force, can be calculated, as a polarization drift must arise to balance the other drifts due to quasi-neutrality.

# Chapter 8

# Grad-Shafranov Equation: Derivation and Implementation

The first task in running a simulation of an axisymmetric toroid is to create the equilibrium that the simulation will be run over. In order to accomplish this $\psi$, the poloidal flux within a magnetic flux surface, must be calculated as a function of $R$ and $Z$ (from cylindrical coordinates). This can be accomplished by using the Grad-Shafranov Equation [76] [77], the derivation and implementation of which, in CHEASE and HELENA, will be provided in this chapter.

## 8.1 Grad-Shafranov Equation

For the derivation of the Grad-Shafranov Equation, a cylindrical coordinate system, ($R$,$Z$,$\phi$) whose axis coincides with the centre line of the toroid is used. Since $\phi$ is an ignorable coordinate ($\partial/\partial\phi = 0$), the poloidal magnetic field can be written in terms of the toroidal component of the vector potential alone:

$$\vec{B} = \nabla \times (A_\phi \hat{\phi}) + B_\phi \hat{\phi}. \tag{8.1}$$

It is customary to use a stream function $\psi$, that is proportional to the poloidal flux $\psi = \psi_{pol}/2\pi$, which gives

$$\begin{aligned} \vec{B} &= \nabla \times (\psi \nabla \phi) + R B_\phi \nabla \phi \\ &= \nabla \psi \times \nabla \phi + B_\phi \hat{\phi} \\ &= \frac{1}{R}\frac{\partial \psi}{\partial Z}\hat{R} - \frac{1}{R}\frac{\partial \psi}{\partial R}\hat{Z} + B_\phi \hat{\phi}. \end{aligned} \tag{8.2}$$

The current density is then given by

$$\mu_0 \vec{J} = \nabla \times B = \frac{1}{R} \triangle^* \psi + \nabla(RB_\phi) \times \nabla\phi, \tag{8.3}$$

where $\triangle^*$ is defined by

$$\triangle^* \psi \equiv R\frac{\partial}{\partial R}\frac{1}{R}\frac{\partial\psi}{\partial R} + \frac{\partial^2\psi}{\partial Z^2}. \tag{8.4}$$

For the plasma to be in equilibrium, the forces acting on it must balance., $0 = -\nabla p + J \times B$. The parallel component of force balance, $\vec{B} \cdot \nabla p = \vec{B} \cdot \vec{J} \times \vec{B} = 0$, means that pressure is a flux surface quantity and so

$$p = p(\psi). \tag{8.5}$$

Inserting Eqns. 8.2, 8.3 and 8.5 into the force balance equation, results in

$$\mu_0 p'(\psi)\nabla\psi = -\frac{1}{R^2} \triangle^* \psi\nabla\psi - RB_\phi \frac{1}{R^2}\nabla(RB_\phi), \tag{8.6}$$

which means that $\nabla(RB_\phi)$ is in the direction of $\nabla\psi$ and so $RB_\phi$ is a surface quantity:

$$RB_\phi = F(\psi). \tag{8.7}$$

This variable $F$ is actually proportional to the total poloidal current

$$F(\psi) = \frac{\mu_0}{2\pi}\int_{S_{pol}} d\vec{S}.J_{pol} = \mu_0\frac{I_{pol}(\psi)}{2\pi}, \tag{8.8}$$

where $S_{pol}$ is a cut surface spanning the centre of the toroid.

The Grad-Shafranov equation then follows from Eqn. 8.6:

$$- \triangle^* \psi = R^2\mu_0 p'(\psi) + FF'(\psi). \tag{8.9}$$

This is essentially another way of writing the force balance equation, with the term on the left hand side of Eqn. 8.9 representing that part of the confinement that comes from the toroidal current crossed with the poloidal magnetic field and the $FF'$ term representing the confinement from the poloidal current crossed with the toroidal magnetic field.

## 8.2 Implementation

The normal procedure for computing an axisymmetric tokamak equilibrium is, firstly, to provide $p' = p'(\psi)$, $F = F(\psi)$ and either a boundary condition of $\psi$ or an externally imposed condition on $\psi$. Then the operator $\triangle^*$ is inverted and $\psi = \psi(R, Z)$ is calculated. For nonlinear profiles and/or boundary conditions, the procedure is iterated until $\psi$ converges to a consistent solution. Note that in general it is not possible to specify $\psi(R, Z)$ first and then calculate $p(\psi)$ and $F(\psi)$ [78].

The documentation for CHEASE is provided in Ref. [79] and the documentation for HELENA is provided in Ref. [80].

There are several ways that $p(\psi)$ and $F(\psi)$ can be provided. Early forms of solving the Grad-Shafranov equation were made by individually specifying $p'(\psi)$ and $FF'(\psi)$ [81]. This, however, makes it difficult to control other equilibrium quantities such as the safety factor, $q(\psi) = \frac{F(\psi)}{2\pi} \int_{\psi=const} \frac{dl}{R|\nabla\psi|}$ where $dl$ is the line element along a constant poloidal flux surface, or the current density profile. This problem was solved by specifying some form of averaged current density [82] [83] in place of $FF'(\psi)$.

## 8.3 Implementation in CHEASE

CHEASE solves the Grad-Shafranov Equation, Eqn. 8.9, for toroidal MHD equilibria as mentioned previously, by specifying the profiles $p'(\psi)$ and $F(\psi)$ and the outermost flux surface.

In CHEASE, $\psi \equiv 0$ is chosen for the boundary, and $\psi < 0$ everywhere inside the plasma. CHEASE then assumes that there is solely one magnetic axis, a region where $\nabla\psi = 0$ and that the total plasma current, $I = \int_\Omega j_\phi dS$ is positive.

### 8.3.1 Free function specification

The first profile required is the pressure gradient, given as a function of $s = \frac{\psi - \psi edge}{\psi_0 - \psi_{edge}}$, where $\psi_{edge}$ and $\psi_0$ are the flux at the plasma boundary and magnetic axis respectively.

The second profile is the current that can be given in three forms.
Firstly, it can be provided as $FF'(s)$.

Secondly it can be provided as the surface averaged current density

$$I^*(s) = \frac{\int_{s=const} j_\phi (J/R) d\chi}{\int_{s=const} (J/R) d\chi} = -\frac{C_1}{C_0} p'(s) - \frac{C_2}{c_0} FF'(s). \tag{8.10}$$

Thirdly, it can be provided as the parallel current density

$$I_\parallel(s) = \frac{\int_{s=const} \vec{J}.\vec{B} J d\chi}{\int_{s=const} \vec{B}.\nabla\phi J d\chi} = -\frac{C_1}{C_2} p'(s) - FF'(s) \left(1 + \frac{1}{F^2(s)} \frac{C_3}{C_2}\right) \tag{8.11}$$

where

$$\{C_0(s), C_1(s), C_2(s), C_3(s)\} = \oint_{s=const} \left\{ \frac{1}{R}, 1, \frac{1}{R^2}, \frac{|\nabla\psi|^2}{R^2} \right\} J d\chi. \tag{8.12}$$

The last closed flux surface can then be provided as either a set of parameters, for solving several formulae, or can be provided as a set of co-ordinates in $(R, Z)$.

## 8.4 Implementation in HELENA

Instead of calculating $\psi$, HELENA calculates $\hat{\psi} = \frac{\psi - \psi_{magaxis}}{\psi_{edge} - \psi_{magaxis}}$ such that $\hat{\psi}_{edge} \equiv 1$ and $\hat{\psi}_{magaxis} \equiv 0$. As with CHEASE, HELENA only allows one magnetic axis. However, unlike with CHEASE, the current can be in both directions.

### 8.4.1 Free function specification

HELENA can accept two different profiles from the $p'(\psi)$ and $FF'(\psi)$ mentioned earlier. These are

$$\begin{aligned} \frac{1}{2} AB\Pi(\hat{\psi}) &= -p'(\hat{\psi}) \\ A\Gamma(\hat{\psi}) &= -\frac{1}{\epsilon} \left(p'(\hat{\psi}) + FF'(\hat{\psi})\right) \end{aligned} \tag{8.13}$$

with $\Pi(0) = \Gamma(0) = 1$. $\epsilon$ is an inverse aspect ratio, $\epsilon = \frac{a}{R_0}$, between the geometric major and minor radii. $A$ and $B$ are then parameters that define the amplitudes of the input profiles. However, only $B$ is specified in the input; $A$ is determined by the fact that $\hat{\psi} = 1$ on the boundary. Using these profiles and normalized co-ordinates,

$y = \frac{Z}{a}$ and $x = \frac{R-R_0}{a}$, the Grad-Shafranov equation, Eqn. 8.9, is written

$$\triangle^* \hat{\psi} = \frac{\partial^2 \hat{\psi}}{\partial x^2} + \frac{\partial^2 \hat{\psi}}{\partial y^2} - \frac{\epsilon}{1+\epsilon x}\frac{\partial \hat{\psi}}{\partial x} = A\left(\Gamma(\hat{\psi}) + Bx\left[1 + \frac{\epsilon x}{2}\right]\Pi(\hat{\psi})\right). \tag{8.14}$$

The two functions $\Pi$ and $\Gamma$ are also specified in the input.

Alternatively, HELENA can accept $I^*(\psi)$ as CHEASE can or calculate this value such that the parallel current profile is consistent with $\langle j \cdot B \rangle_{BS} + E_{\|}\eta(\chi)$ (the parallel component of the bootstrap current and the inductively driven current).

Unlike in CHEASE, the outer boundary (for $\hat{\psi} = 1$) cannot be given as a series of grid points. There are several methods of providing this outermost flux surface.

In this thesis, the method used to provide the outermost flux surface is a truncated Fourier series

$$r = \sum_{m=0}^{M_2} f_m \cos(m\theta), \tag{8.15}$$

where both the Fourier coefficients $f_m$ and the total number of Fourier terms $M_2$ have to be specified.

## 8.5 Limitations

CHEASE and HELENA can both only generate flux surfaces that are nested within the specified outer boundary. This means that the region that can be simulated is limited to within the last closed flux surface. This can cause problems when running realistic tokamak equilibria, where the large pressure gradient region tends to be very close to the last closed flux surface. Attempts to combine scrape-off layer profiles with a created equilibrium have been made [84].

Also, CHEASE and HELENA require that the outer boundary be sufficiently smooth. This is evident in HELENA where the outer boundary must be provided as parameters of an equation, or as Fourier coefficients. This means that the X-point must be smoothed out for an equilibrium.

There are free boundary codes that can overcome these limits, allowing simulation of open field line regions, such as EFIT [85]. However, ORB5 takes equilibria data in a specific format, a format provided by CHEASE. Hence, for simplicity, CHEASE (or HELENA equilibria files run through CHEASE to provide the correct format) was used to provide the equilibrium files for the ORB5 simulations.

## 8.6 ORB5 normalisation

In order to perform simulations in ORB5, the profiles and physical parameters must be converted from the units given by CHEASE, SI units, into ORB5 units.

The basic time scale in ORB5 is $\Omega_{ci} = q_i B_0/m_i$ where $B_0$ is the magnetic field at the axis, $q_i$ is the ion charge and $m_i$ is the mass of the ion, all in SI units. The basic length unit in ORB5 is $\rho_i = c_s/\Omega_{ci}$, the ion sound gyroradius, calculated from the electron temperature since the speed of sound is given by $c_s = \sqrt{T_e/m_i}$. The parameter $\rho^* = \frac{\rho_i}{a}$, where $a$ is the geometric minor radius (half of the diameter of the device), is used to set the size of the device.

ORB5 uses a normalised temperature and density profile. They are normalised to the value at a specified location. For the circular outer boundary equilibrium, analysed in Chapter 9, the location of greatest pressure gradient $s = 0.5$ is the location that is normalised to, with $T_e(s = 0.5) = 836$eV as can be seen in Fig. 9.2. This means that the value of pressure in ORB5 is actually determined by a parameter $\beta$. The definition used in ORB5 is $\beta = \mu_0 n_e T_e/B_1^2$ in SI units, with $n_e$ and $T_e$ being the normalising density and temperature as mentioned previously (at $s = 0.5$, for the equilibrium in Chapter 9), $\mu_0$ is the permeability of free space and $B_1$ is the normalising magnetic field on the axis. This results in $\beta = 0.0135$ for the base circular equilibrium. This differs from the $\beta_{CHEASE}$ parameter provided by CHEASE in the equilibrium output file. The definition of $\beta_{CHEASE}$ is calculated using pressure values and magnetic values from other locations in the equilibrium, with $\beta_{CHEASE} = \langle p\rangle/\langle B^2/2\mu_0\rangle$, where $\langle ...\rangle$ refers to average values. The definition of $\beta$ in ORB5 also has a factor of 2 missing from the definition used in CHEASE, since $\beta$ used only the electron temperature and density, whereas $\beta_{CHEASE}$ used the overall plasma pressure, since it creates MHD equilibria where the plasma is treated as a fluid. Hence forth all reference to $\beta$ will be the value used in ORB5.

# Chapter 9

# Modelling Kinetic Ballooning Modes in a Simplified Equilibrium

Instabilities that occur in tokamaks are usually divided conceptually into two different groups, macroscopic instabilities and micro-instabilities [86]. Macroscopic instabilities are those which have perpendicular wavelengths comparable in size to perpendicular characteristic length scales of the device and are treated using fluid theory, since the mode structures are large enough that FLR and other kinetic effects can usually be ignored for the instabilities of interest. Microscopic instabilities are those which act on the basic plasma scales, such as $\rho_i$, and are treated using either gyrokinetics or drift kinetics. A local gyrokinetic code can be used if the mode structure is small enough to avoid interacting with characteristic system length scales, if not, a global version is required.

For MHD, the only length scales are macroscopic: for example the temperature scale length $L_{T_i}$. Therefore MHD agrees with global gyrokinetics for wavelengths much larger than $\rho_i$ [87]. This is the case, in ORB5, for small toroidal mode number $N$, where the wavelengths are closer to the scale lengths of the profiles and hence are too wide to be analysed using a local gyrokinetic approach, and for small $\rho^*$, where the FLR effects are small since they are not present in MHD.

However, for local ion scale gyrokinetics, the characteristic length scale is the ion gyroradius $\rho_i$, such that $k_\parallel \rho_i \approx O(\epsilon) \ll 1$ and $k_\perp \rho_i \approx O(1)$, where $k_\parallel$ is the parallel wavenumber and $k_\perp$ is the perpendicular wavenumber. The perpendicular system scale lengths are not present in local gyrokinetics, due to the limit of an infinite space with constant gradients in the perpendicular direction. For agreement with local gyrokinetics, the ORB5 simulations must be run with small $\rho^* = \rho_i/a$, such that the Larmor radius is small compared to the system scale lengths. For our case, this means that more gyroradii fit within the pressure gradient region, so locally, the plasma resembles the infinitely wide homogeneous pressure gradient region of local gyrokinetics. For similar reasons, global gyrokinetics agree with local gyrokinetics at the short wavelength, high $k_\perp$, where the mode width is small enough to fit within the pressure gradient region and does not reach the region of low pressure gradient and weak drive for the instabilities.

This means that global gyrokinetics agree with these two theories in different limits. To determine whether ORB5 simulations agreed with a local gyrokinetic code GS2 and an MHD code MISHKA, global gyrokinetic simulations of a simplified MHD equilibrium were run and checked for agreement in the appropriate limits. This was undertaken to confirm the value of the drive terms present and show that the drive terms depend on the curvature, as is shown theoretically for a Z-pinch in Chapter 7.

These simulations show how well the underlying global gyrokinetic formulations and numerics present in ORB5 can match with the theory explained in Ref. [28] and how well it converges with MHD and local gyrokinetics. This yields understanding of the physics of global MHD-type modes in the global gyrokinetic framework and shows what global gyrokinetics can achieve and in what limits it is applicable.

## 9.1 Drive Strengths between MHD and Gyrokinetics

The main issue in comparing drive strength between MISHKA and ORB5, as shown in Chapter 7, is that the $\delta B_{||}$ effects are missing in the gyrokinetic formalism used in ORB5, which results in the effective curvature drive being reduced for the instability at finite $\beta$. The existing code does not include $\delta B_{||}$ fluctuations and there was not enough time during this project to include them. There are recent papers that emphasise the importance of compressibility and that finite-$\beta$ compression effects are as important as finite-$\beta$ equilibrium effects (of the same order of magnitude) [88] [89]. In GTC (Gyrokinetic Toroidal Code) the extra $\delta B_{||}$ is calculated from the electron adiabatic response in an extra step at the end of each iterative step and is then used in a modified continuity equation [90].

In the drift regime, the currents in the plasma can be decomposed into magnetisation currents, drift currents, polarisation currents and parallel currents. Since only $\delta B_\perp$ is kept, then the parallel currents are the only currents necessary for Ampére's law. The perpendicular currents are still important for setting up these parallel currents and for determining the evolution of the charge density. The divergence of the currents gives the rate of change of the local charge density (charge conservation). This is then related to the electric field evolution through the Poisson equation, Eqn. 3.35.

In the gyrokinetic equations, the particle motion is a direct consequence of Newton's laws. The moments of the gyrokinetic equations leads to the fluid relations (at high wavelength and ignoring certain higher order effects) such as $mndv/dt = J \times B - \nabla p$, where $J$ is the sum of all currents excluding magnetisation currents (Note that this means that $J \neq \nabla \times B$ using this $J$). For the ORB5 $A_\|$ formalism, the magnetisation current doesn't lead to a change in the parallel magnetic field as there is no $B_\|$ perturbation allowed. For low $\beta$, $\delta B_\|$ doesn't lead to any forces, since $J_\perp = 0$ for force-free plasmas. This is violated for a finite-$\beta$ tokamak, but we will at least have pressure balance in the wavevector direction which gives equal currents and thus forces for the MHD and the drift regime.

However for higher $\beta$, the gyrokinetic $A_\|$ formalism tends to underestimate the drive compared to MHD as the $\nabla B$ drift reduces to zero on the outboard midplane as a result of the Shafranov shift compression of the field lines as seen in Fig. 9.1. Curvature, however, is not strongly modified by the finite-$\beta$ equilibrium effects and is dominated by the toroidicity so the radius of curvature is close to $1/R$. This results in the perpendicular current arising from pressure perturbations being lower than the corresponding MHD value. What should compensate for this is the finite-$\beta$ perpendicular currents interacting with the $B_\|$ perturbation, leading to a force that enhances this drive: this is missing in ORB5.

An adhoc method of "fixing" this is to impose that the total curvature and $\nabla B$ drifts are compensated so that the current driven by these drifts is just proportional to curvature and matches the MHD drive. The difference that occurs when $\delta B_\|$ is included in the derivation, is the replacing of the effective drive term $2\omega_k$ by $\omega_k + \omega_B$ as seen in Eqn. 5.16. Since $v_k = v_B + K\nabla p$ (Eqn. 3.15 from Ref. [28]), where $K$ is a constant, in order for $2\omega_k$ to be equivalent to $\omega_k + \omega_B$, the pressure gradient must be doubled, so that $v_k + v_B = 2v_k$. Note that the pressure gradient should

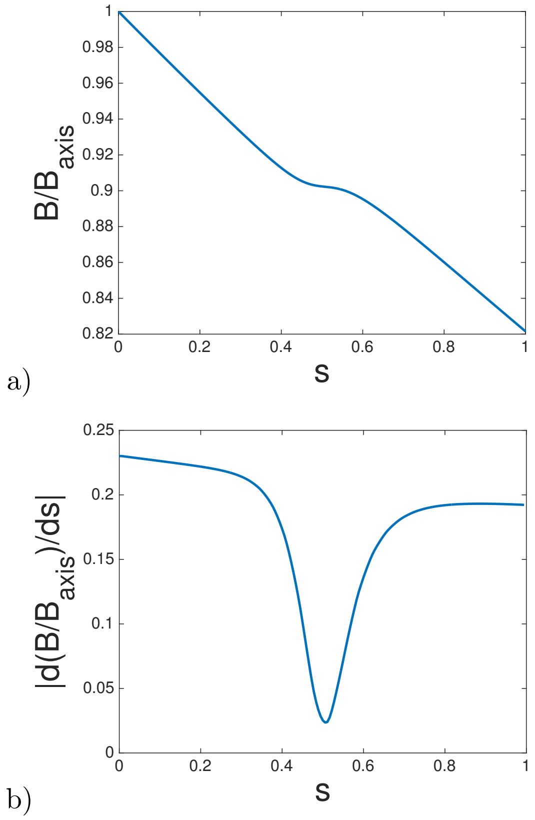

Figure 9.1: a) Magnetic field and b) $\nabla B$ along the outboard midplane.

only be doubled for this use (Other uses of the pressure gradient still require the correct value). In ORB5, this can be achieved by doubling the pressure gradient in the input equilibrium file, increasing the curvature drift to balance the decrease in the $\nabla B$ drift. Note that a separate input file, with the information about profiles, has the correct pressure gradient profile that is used for all other uses of the pressure gradient. The drifts can be seen in the equation of motion used in ORB5, Eqn. 3.28.

## 9.2 Gyrokinetic Ballooning Theory in General Geometry

In Ref. [28], a general derivation of gyrokinetic ballooning theory for large toroidal mode number, $N$, modes is provided in certain limits. This paper is self-contained except for the derivation of the linear gyrokinetic equation, which is given in Ref. [63]. For the pedestal region, the steep pressure gradients imply that the diamagnetic drift, $v_{dia} = \nabla p_0 \times B/qnB^2$, is much greater than the curvature and ∇B drifts, as $\frac{v_{dia}}{v_{curv}} \approx \frac{\nabla p/p}{\nabla B/B}$, and, since ideal-MHD theory indicates that near marginal stability $\omega \to 0$, the mode frequency is much larger than the ion transit frequency, but much smaller than the electron transit frequency. This means that the kinetic effects can be written in a simpler form: adiabatic response for the electrons and gyrofluid response for the ions. Therefore good agreement is expected between ORB5 and the analytic theory in the large $\rho^*$ limit for high $N$ modes. For low $N$ modes, the global profile effects cannot be ignored.

For low frequency modes, with frequencies lower than the electron and ion transit frequencies, equation 3.24 from Ref. [28] (ignoring trapped particles) is derived by placing solutions to the linearised gyrokinetic equation (in an extra step at the end of each iterative step in equation 2.18 from Ref. [28]) in the quasi-neutrality equation (equation 2.31 from Ref. [28]):

$$\frac{L_c^2}{JB^2}\frac{\partial}{\partial\chi}\left(\frac{b}{J}\frac{\partial}{\partial\chi}\Phi\right) + \left(\frac{\omega}{\omega_A}\right)^2\left[\frac{2\omega_{*p}\omega_k}{\omega^2}\Phi + (k_\perp^2\rho^2/2)\left(1 - \frac{\omega_{*p}}{\omega}\right)\Phi\right] = 0, \tag{9.1}$$

where $\omega_{*p} = \frac{NT_0}{e}\frac{d}{d\Psi}ln(n_0T_0)$, $L_c$ is the connection length, $\omega_A^2 = v_A^2/L_c^2$ is the Alfvén frequency ($v_A$ is the Alfvén velocity) and $k_\perp$ is the perpendicular wave number. The MHD limit corresponds to setting the final term to zero, with the first term corresponding to field line bending stabilisation, and the curvature is the first term in the straight brackets. (Since we are in SI units, factors of $c$ are absent). The only difference between this formula and the MHD result is the replacement of $\omega^2$ by $\omega(\omega - \omega_{*p})$, when FLR and kinetic effects are ignored. Therefore it should be possible to reproduce the local and large-$N$ global results, where global effects are negligible, using this analytical formula.

The equivalent equation for the $A_\parallel$ in ORB5 can be derived by setting $\delta B = 0$ in Eqn. 5.14. This then results in Eqn. 9.1, but modified by replacing the effective drive term $2\omega_k$ by $\omega_k + \omega_B$ (such that the first term in the square brackets in Eqn. 9.1 can be written $[\omega_{*p}(\omega_k + \omega_B)/\omega^2]\Phi$ , where $\omega_k$ is the frequency of the curvature drift and $\omega_B$ is the frequency of the $\nabla B$ drift, as can be seen from Eqn. 5.16.

One of the conditions for this equation, $\omega << v_{Te}/R$, is always valid since typical growth rates are smaller than $c_s/R$. However, except near marginal stability, growth rates are found such that $\gamma >> v_T/R$, where $v_T$ is the thermal velocity, (due to large pressure gradients) and so we can ignore ion kinetic effects due to parallel streaming along field lines and we are at the intermediate regime rather than the low frequency regime mentioned above, except in low $N$ where frequencies are small and growth rates tend to zero. However, the same issue with the drive strengths (where the $\delta B_{\parallel}$ contributions are ignored) also applies in the intermediate regime [28]. The low frequency regime has been used to show the difference between MHD and gyrokinetic theory as this regime is explored in further depth in Ref. [28]. It is also simpler, since the electrons and ions are in the same regime and different approaches are not required for each species.

## 9.3 Equilibrium

The base case is a relatively simple equilibrium designed to exhibit similar pressure-driven instabilities to a plasma pedestal with a moderate aspect ratio, $R/a = 10/3$, for a deuterium plasma. To simplify the numerics and interpretation, an equilibrium with a circular outermost flux surface was chosen. In order that pressure gradient driven instabilities grow, a pressure profile was chosen such that the pressure gradient is significant enough to be MHD unstable and the pressure profile is almost flat except for a sharp step at mid-radius to simulate a pedestal-like region. Unlike in a physical pedestal case, where the pedestal is very close to the outer last closed flux surface, this provides a substantial buffer region between the large pressure gradient region and the boundary.

However, for the gyrokinetic simulations, the temperature and density profiles had to be specified. It was specified that $T_e = T_i$ and that the density was constant, which means that the pressure profile was solely determined by the temperature profile. When simulations with this calculated temperature profile were run, non-physical modes were noticed growing in the region of zero pressure beyond the pedestal-like region. This is due to the fact that $T_e = 0$ is problematic for the global gyrokinetic code and so, in order to avoid this issue, 387eV was added to the temperature profile (approximately half the pedestal height). This does not affect the shape of the equilibrium, since the pressure gradient is not affected and the magnitude of the pressure does not affect the Grad-Shafranov equation, Eqn. 8.9. The equilibrium parameters appear in Table 9.1.

CHEASE is the code used to prepare the equilibrium, where the flux surfaces are calculated by solving the Grad-Shafranov equation, Eqn. 8.9. It takes the pressure gradient and current profiles as the input profiles. Along with the shape of the last

| Parameter | CHEASE value | ORB5 value |
|---|---|---|
| $q$ at axis | 1.05 | 1.05 |
| Minor radius | 0.3m | 70 |
| Major radius | 1.0m | 233 |
| $B$ at axis | 0.956T | 1 |
| $T_e$ at axis | 1144eV | 1.368 |
| $T_e$ pedestal height | 757eV | 0.947 |
| $n_e$ | $7.37 \times 10^{19}\mathrm{m}^{-3}$ | 1 |
| $q_i$ | $+e$ | 1 |
| $m_i$ | $2m_p$ | 1 |

Table 9.1: Profile parameters for the benchmark base case described in this chapter. $m_p$ is the mass of a proton and $e$ is the absolute value of the electron charge. The temperature pedestal height is defined as the difference between the core temperature and the edge temperature. As can be seen in Fig. 9.2, the electron temperature is flat except in the pedestal for this equilibrium.

closed flux surface, this is enough to solve the Grad-Shafranov equation and to provide the equilibrium. The original equilibrium has a uniform toroidal current and the pressure gradient associated with the temperature profile in Fig. 9.2. CHEASE then provides the pressure and shape in SI units in the output equilibrium file, i.e. pressure in Pascals (Pa), dimensions in metres (m) and magnetic field in Tesla (T) and must then be converted into ORB5 units.

The simplest choice to drive the growth of kinetic ballooning modes is to specify zero global magnetic shear, $s = \frac{r}{q}\frac{dq}{dr}$ which can be expected to be the most unstable given the cylindrical stability criteria [72], but MHD equilibria of this form are stable due to the strong Shafranov shift that leads to a large local shear at the outboard mid-plane, where the drive is strongest.

Therefore an equilibria with small local magnetic shear, $s_{local} = 2\pi\vec{n}.\nabla \times \vec{b}$ where $\vec{n} = \frac{\nabla\psi}{|\nabla\psi|} \times \frac{\vec{B}}{|\vec{B}|}$, was created, in order to ensure robust instability growth, since the field lines are aligned and do not inhibit the motion of other field lines. The phase of a field-aligned mode may be written as $P = N(\zeta - q\chi) + K$, where $\psi$, $\chi$, $\zeta$ are straight field line magnetic co-ordinates, such that $\psi$ is the poloidal flux within a magnetic flux surface, $\chi$ is the poloidal angle-like coordinate and $\zeta$ is the toroidal angle, and $K = 0$ is for a mode with zero radial wavenumber at the outboard mid-plane. Note that $s = \sqrt{\frac{\psi}{\psi_{end}}}$ can be used instead of $\psi$ and more closely reflects the radial coordinate $r$ in a tokamak and as such is used instead of $\psi$ for some future

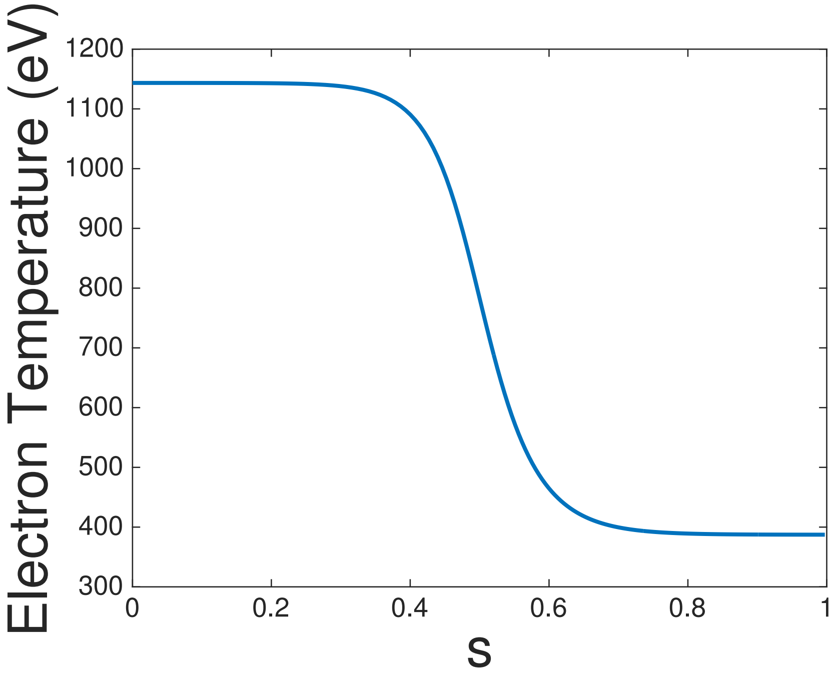

Figure 9.2: The temperature profile for $\beta = 0.0135$.

figures. In these equilibria, lines of constant phase, in the poloidal plane, of field-aligned modes at some fixed toroidal mode number $N$ are nearly perpendicular to the flux surfaces for a range of $\chi$ near the outboard midplane.

The current profile in the equilibrium is modified such that $\nabla[q(R,Z)\chi(R,Z)].\nabla s = 0$ in the outboard quarter ($\chi = -\pi/4$ to $\chi = \pi/4$), which results in straightening of lines of constant $q\chi$ on the outboard side as can be seen in Fig. 9.4, which requires iteration of the CHEASE equilibrium code with the correction based on the approximate relation between the $q$ and toroidal current $I$ profiles. In order to achieve this change in q, the current must be changed as the Grad-Shafranov Equation only depends on the pressure gradient, last closed flux surface and current profile and the pressure profile and last closed flux surface are chosen to remain constant. The toroidal current is changed in order to reduce the local magnetic shear at the outboard midplane for the original equilibrium. Then CHEASE is run with the corrected current in order to recalculate the equilibrium profiles to match the new current. This procedure results in a lower local magnetic shear on the low field side. Note that this iteration was performed once, as a second reduction of the local shear, resulted in CHEASE not being able to find an equilibrium.

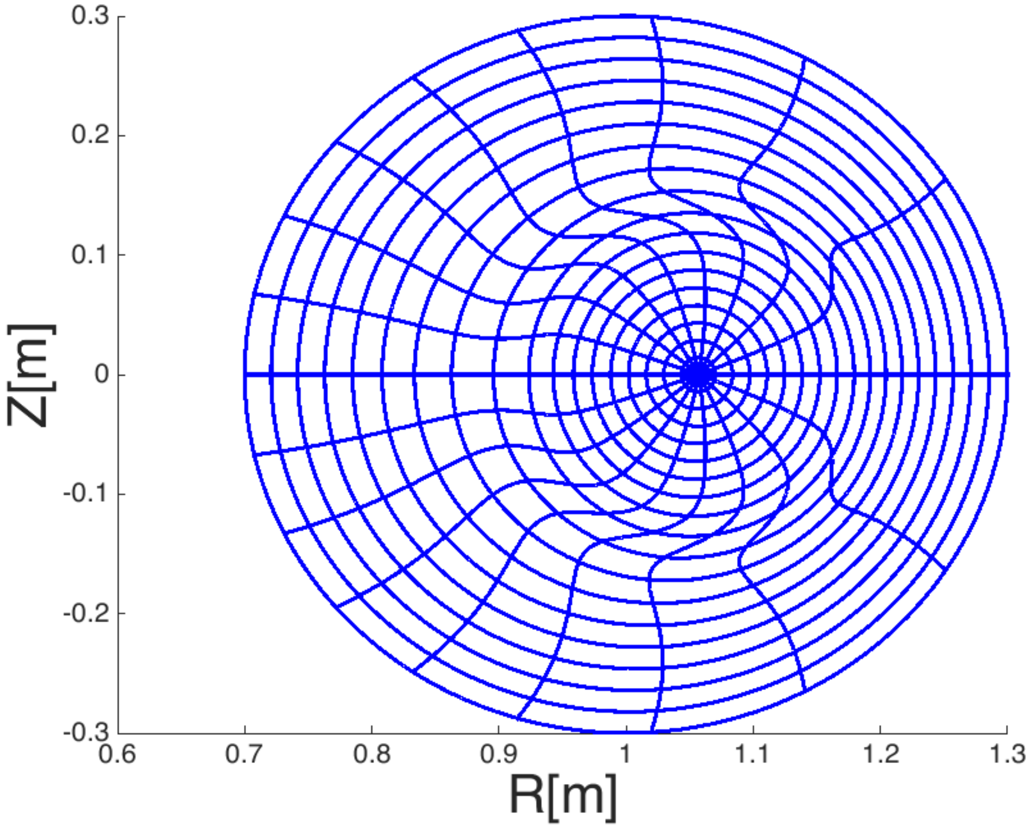

Figure 9.3: The $\chi$ and $s$ grids for the benchmark equilibrium. The grid lines are plotted with constant intervals in $\chi$ and $s$ (The actual numerical grid is much finer).

Note that this means that lines of constant $\chi$ are strongly bent as seen in Fig.9.3. It is the combination of $q$ and the shape of $\chi(R, Z)$ that allows MHD modes which are elongated along the field line but have little bending energy, which is a stabilising effect.

As mentioned in the introduction to this chapter, the global gyrokinetic formalism is expected to agree with MHD and local gyrokinetics for small $\rho^*$ in the appropriate opposite limits (low-$N$ for MHD and high-$N$ for local gyrokinetics). This means that $\rho^*$ is reduced from the equilibrium value of $\rho^* \approx \frac{1}{70}$ to values of $\frac{1}{800}$. To simplify the comparison between the MHD and gyrokinetic growth rates, when a series of equilibria with varying values of $\rho^* = \rho_i/a$ were created, the MHD instability growth had to be kept constant in SI units (seconds). Similarity requires that the other dimensionless parameter, $\beta$, remains constant also. The MHD growth

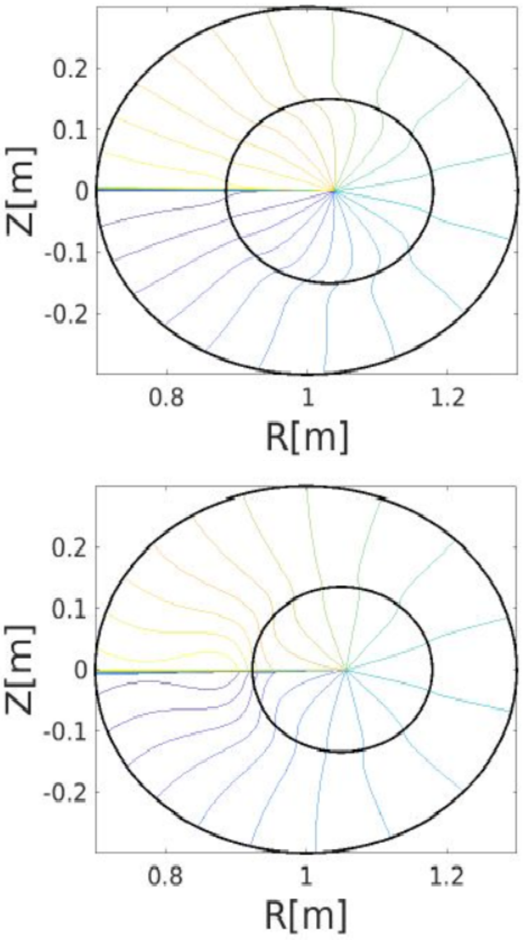

Figure 9.4: Lines of constant $q\chi$ for (a) the original and (b) the modified (with $\nabla[q\chi].\nabla s = 0$ equilibrium with black lines at $s = 0.5$ and 1.

rates scale with the Alfven time, so $v_A/R = (T/m)^{1/2}/R\beta^{1/2}$ is kept fixed. If $T$ and $R$ are kept constant, but $B$ is scaled proportional to $1/\rho^*$ and density is scaled proportional to $1/\rho^{*2}$, both $\beta$ and $v_A/R$ are kept fixed.

## 9.4 Numerical Parameters

Simulations were undertaken with times step of $\Omega_{ci}$, to avoid numerical instability. KBM simulations were undertaken with lower time steps to assure that the time step of $\Omega_{ci}$ had converged. The grid sizes, chosen for the three spatial coordinates, were $N_\psi = 256$, $N_\chi = 256$ and $N_\phi = 256$, for $N = 20$. As toroidal mode numbers were increased, the number of grid points in the $\chi$ and $\phi$ directions also had to be increased, such that the value was more than 4 times the toroidal/poloidal mode

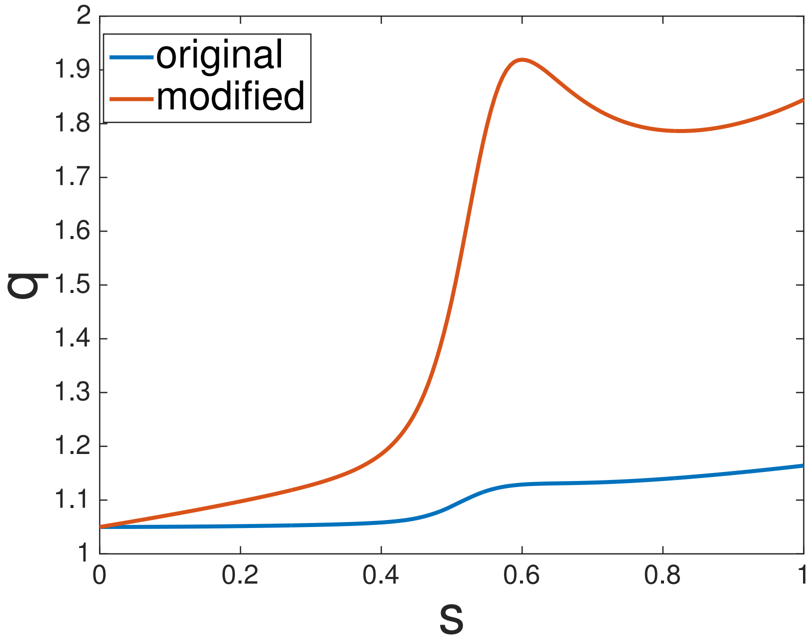

Figure 9.5: Safety factor before and after the procedure to minimise the local shear.

number (Since more than four points per wavelength are required to describe a wave [91]). For each simulation, the toroidal mode filter was selected, such that a particular mode number was kept. However, the poloidal mode filter was chosen such that the mode numbers allowed were three times larger than the toroidal mode number. This was chosen as the safety factor increases to around two and we wanted to avoid suppressing growth rates. For a $N = 30$ simulation, the poloidal filter was $M_{min} = -90$ and $M_{max} = 90$.

## 9.5 Modified Drive Term

To verify that the basic interchange method has the right strength in the gyrokinetic formulation, electron-ion simulations were run with the standard drift terms active and with a 'corrected' drift term for which the $\nabla B$ drift was replaced by the curvature drift to make sure that the MHD drive strength was recovered. This increased drive strength would be provided by $\delta B_{||}$ in a self-consistent simulation. This was accomplished, as previously mentioned, by doubling the pressure gradient in the ORB5 equilibrium input file. The simulation results were then compared to a similar simulation performed in MISHKA, a linear MHD stability code to compare the results.

ORB5 simulations run without the modified drive term showed no mode present, even though a strong MHD instability was verified using MISHKA. With the modified drive terms, however, a mode can be seen growing as indicated in Fig. 9.6.

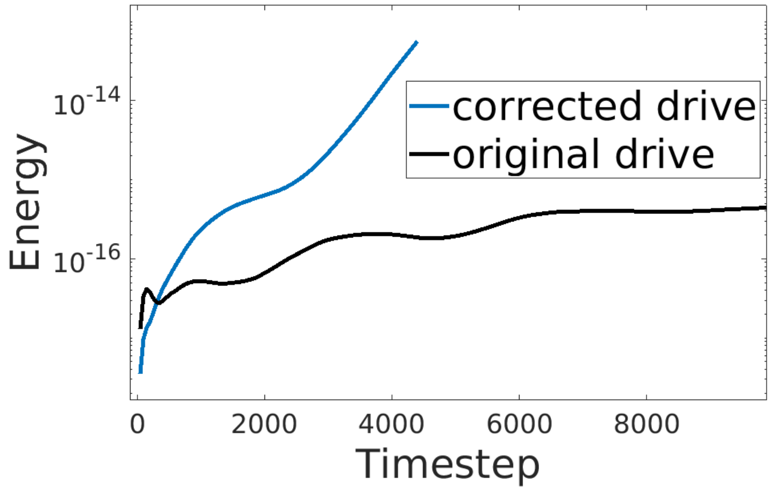

Figure 9.6: Energy vs time for two simulations, with $N = 30$ and $\rho^* = \frac{1}{800}$ with original drive and with additional drive term to correct for $\delta B_{||}$ effects.

## 9.6 Mode Structure

In Fig. 9.7, a poloidal slice of the electrostatic potential, $\phi$, is plotted for $N = 30$ and $\rho^* = \frac{1}{800}$. As can be seen from the plot, the ORB5 simulations were undertaken on a smaller section of the annulus, in order that the simulations be more efficient as the ORB5 simulations are costly to perform, as all global gyrokinetic simulations are. In addition, the mode is centred on the outboard midplane at the region of greatest pressure gradient as expected for kinetic ballooning modes and is similar to the mode structure observed in MISHKA, with the mode being situated on the outfield side and centred on the same flux surfaces. As can be seen from the grey lines, which represent the same flux surfaces in both simulations, both modes grow in the same region (the pedestal-like region). The magnitude of the electrostatic potential is not useful for these plots as they are both linear runs and as such the amplitude has no physical significance and as such a qualitative comparision is all that can be accomplished from these plots and simulations in terms of comparing the electrostatic potential.

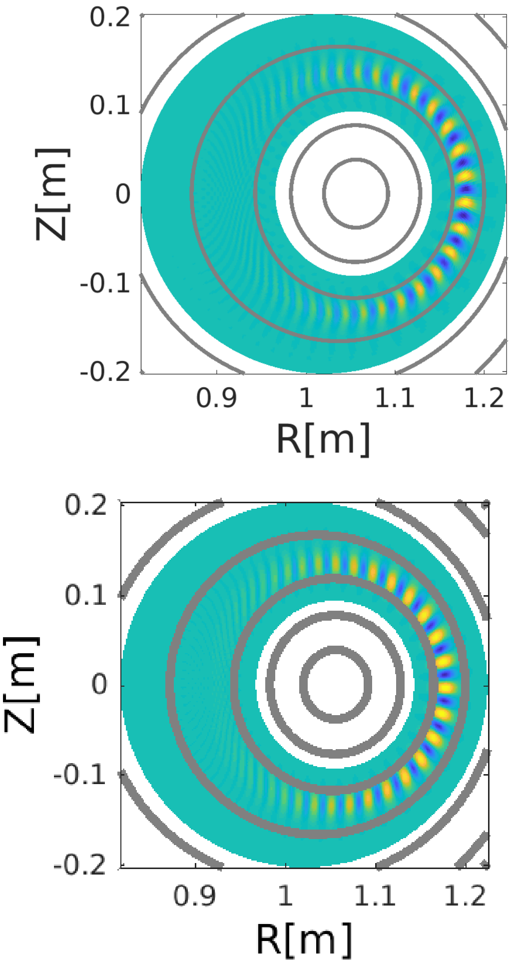

Figure 9.7: 2D density plot of the electrostatic potential versus $R$ and $Z$ for (a) ORB5 and (b)MISHKA where $N = 30$ and $\rho^* = \frac{1}{800}$. The grey lines represent equivalent flux surfaces between the two plots.

As can be seen in Fig. 9.8, regions of strong electrostatic potential are concentrated in the pedestal-like region of the plasma, centred at the point of greatest pressure gradient. Also as we decrease $N$, the mode widens until it extends beyond the region of pressure gradient as seen in $N = 10$. This due to the increase in perpendicular wavenumber and hence decrease in perpendicular wavelength.

In order to further confirm that the correct mode was growing, $E_{\|}$ was calculated and compared in magnitude to $\frac{dA_{\|}}{dt}$. Since MHD instabilities have $E_{\|} = -\vec{h} \cdot \nabla\phi + \frac{\partial A_{\|}}{\partial t} \approx 0$, due to the freedom of movement that electrons have parallel to the magnetic field.

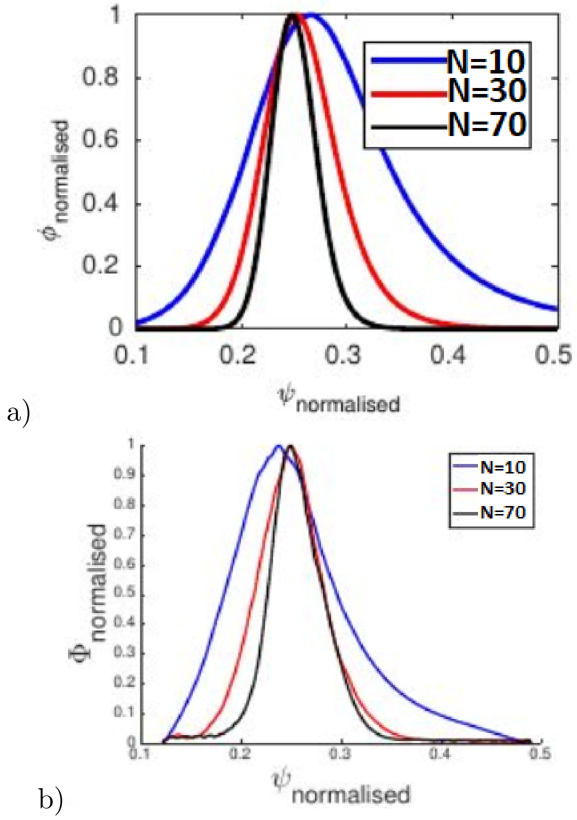

Figure 9.8: Maximum $\phi$ for each flux surface for three different values of $N$ in a) MISHKA and b) ORB5 with $\rho^* = 1/800$. (The peak value is normalised to one)

Therefore $E_\parallel \ll \frac{dA_\parallel}{dt}$ as the two terms on the right hand side cancel each other. As can be seen from 9.9, this is the case for these modes as $E_\parallel / \frac{dA_\parallel}{dt} \ll 1$. This is consistent with an MHD instability as expected.

## 9.7 $N$ Scan

Shown in Fig. 9.10 are the growth rates of kinetic ballooning modes for the benchmark case in both MISHKA and ORB5. In the ORB5 graph are the plots for three $\rho^*$ that scans were performed over. In order to negate the finite Larmor radius effects, and therefore match with MHD results, a sufficiently small value of $\rho^*$ was needed. ORB5 cannot run with zero $\rho^*$, so scans for $\rho^* = \frac{1}{800}$, $\frac{1}{400}$ and $\frac{1}{200}$ where performed to make sure that the runs had converged with respect to $\rho^*$. As can

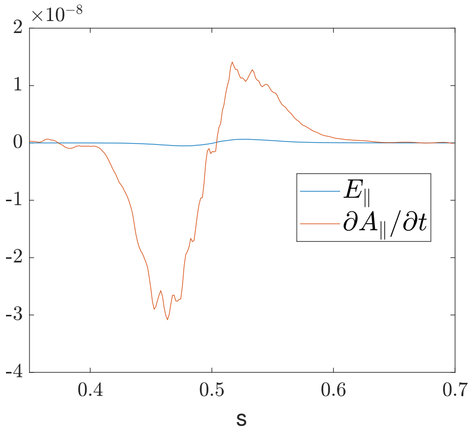

Figure 9.9: Plots of $E_{\parallel}$ and $\frac{dA_{\parallel}}{dt}$, for $N = 30$, $\rho^* = \frac{1}{800}$ and $t = 2900\Omega_{ci}$, in comparable ORB5 units.

be seen from Fig. 9.10, the three ORB5 curves appear to match closely for low $N$ and so it can be concluded that convergence had been achieved and that the results should not differ from the MISHKA curve due to finite Larmor radius effects. As can be seen from the plot the ORB5 growth rates have a similar magnitudes and qualitative behaviour to the MHD growth rates for low $N$, with the maximum growth rate increasing towards the MHD growth rate as $\rho^*$ decreases. This shows the importance of correcting the drive term and gives us the confidence in the reliability of the ORB5 simulations as the expected result is that as $\rho^*$ decreases, the plot approaches the MHD limit, where the $N$, for which the maximumal growth rate lies, increasing. Possible reasons for the differences between the MHD growth rates and ORB5 growth rates at low-$N$ are given in the conclusions of this chapter.

A curved line with a maximum in the centre is expected for kinetic ballooning mode growth rates. The low-$N$ drop off in growth rate is due to global effects due to the finite width of the pedestal, absent in local gyrokinetic simulations. This effect can also be expected from the mode structure shown in Fig. 9.7, since the mode structure is comparable in size to the region of large pressure gradient. For higher-$N$, the growth rate decreases due to the diamagnetic drift as explained in Ref. [28], an effect which also appears in the local gyrokinetic results. This is due to the replacement of $\omega_{MHD}^2$ by $\omega(\omega - \omega_{*p})$ in the equivalent equations (Eqn. 9.1 is the gyrokinetic version of this equation).

As can be seen from the shape of the curve, the ORB5 growth rates go to zero for low-$N$, as they do for MISHKA growth rates, but also tend to zero for high-$N$ as

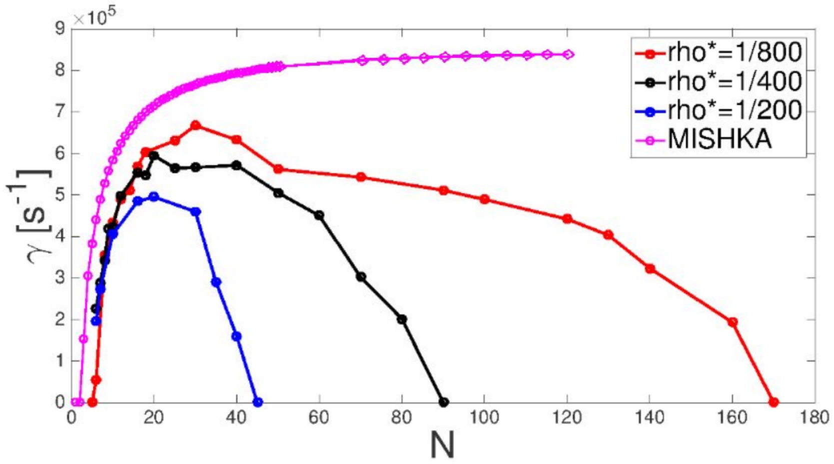

Figure 9.10: Growth rate vs $N$ for $\rho^* = \frac{1}{800}, \frac{1}{400}, \frac{1}{200}$ and the MISHKA scan for the same equilibrium.

expected due to kinetic effects, such as the diamagnetic drift. The low-$N$ modes are too large to fit into the region with a pressure gradient and even reach into the region with zero drive (small pressure gradient).

## 9.8 $\beta$ Scan

The $\beta$ scan can be seen in Fig. 9.11. This $\beta$ scan was achieved, by changing the maximum pressure gradient that the region of large pressure gradient could achieve. Given the same value beyond the pedestal region, this resulted in a lower pressure in the core region and hence a change in the value of $\beta$. In this scan, the expected behaviour for both kinetic ballooning modes and ideal ballooning modes from MHD is observed. There is a critical-$\beta$, below which ballooning modes do not grow. This critical-$\beta$ is vitally important as it dictates what is the maximum pressure gradient that can be achieved for a given equilibrium shape. The critical-$\beta$ is the same for the ORB5 simulations and the MISHKA simulations. As $\beta$ increases the growth rate increases, but at a decreasing rate. The drift kinetic theory scan however, has a higher critical-$\beta$. This agreement is only verified for simulations with low $\rho^*$ and could be broken for larger values of $\rho^*$.

## 9.9 Local Comparison

One effect that is missing from MHD formalism compared to gyrokinetic formalisms is diamagnetic drift stabilisation. This is not a drift that occurs due to a force acting

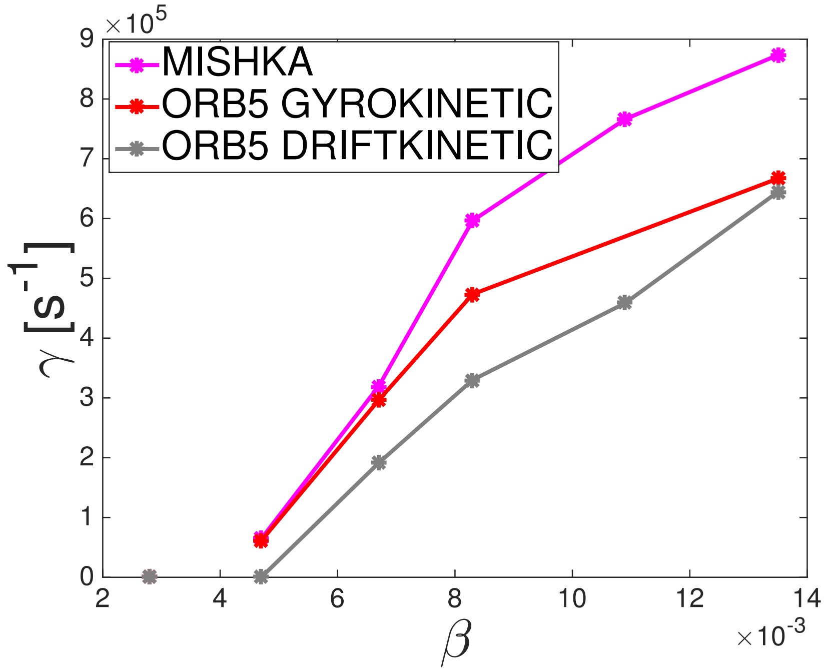

Figure 9.11: Growth rate vs $\beta$ for $N = 30$, $\rho^* = \frac{1}{800}$ in MISHKA and in ORB5, using both the gyrokinetic model and the drift kinetic model.

on individual particle gyrations such as the $\nabla B$ and curvature drifts, but occurs due to an imbalance of pressure in regions in the plasma resulting from the pressure gradient and acts counter to the $\nabla B$ and curvature drifts. There is a parallel current associated with the pressure perturbation due to thermal conduction. This then gives rise to an electric field that would tend to displace the pressure perturbation toroidally and therefore competes with the electromagnetic effects. The frequency associated with the diamagnetic frequency (the velocity divided by the wavenumber) is proportional to $N$, which results in an effect that causes the growth rate to reduce as $N$ increases (the diamagnetic drift is opposite to the $\nabla B$ and curvature drifts that drive the instability, as shown in Fig. 2.6). In this section, it will be shown that the diamagnetic drift can explain the differences in growth rates between MHD and local gyrokinetic simulations for larger $N$ as well as account for a large amount of the high $N$ behaviour of the ORB5 growth rates.

A formulation of the diamagnetic drift frequency is given in Eqn. 2.18, as

$$\omega_{*p} = \frac{NT_0}{e}\frac{d}{d\psi}ln(n_0T_0). \tag{9.2}$$

The diamagnetic drift can therefore be calculated just from the equilibrium quantities and is given by $-N \times 1.0895 \times 10^5 \mathrm{s}^{-1}$ for the base equilibrium, at the point of largest temperature gradient. Note that the values are negative, as the diamagnetic drift acts opposite to the driving drifts. As can be expected from the definition of the diamagnetic drift frequency, Eqn. 9.2, the diamagnetic frequency increases as the pressure gradient increases and as $N$ increases.

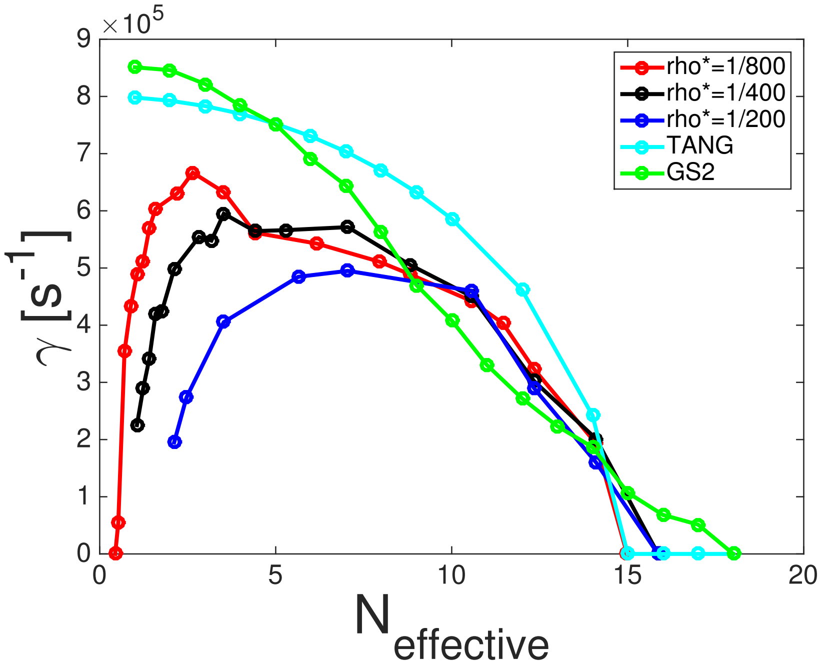

Figure 9.12: Growth rate vs Effective N ($N_{effective} = N\ (\rho^*/\rho_0^*)$) for several different values of $\rho^*$ in ORB5, the theory described in Ref. [28] and the GS2 simulations.

Using the relationship $\omega_{MHD}^2 = \omega(\omega + \omega_{*p})$, from Eqn. 5.16, gives the expected local gyrokinetic results (the Tang curve in Fig. 9.12). As can be seen from Fig. 9.12, the growth rates, provided by both ORB5 and GS2, match closely the theory (For ORB5 this is the case for the higher values of $N_{eff}$. Note that the global results are expected to match the local results for the same value of $k_\theta \rho_i$ and as such Fig. 9.12 plots growth rate vs an effective $N$, which is proportional to $k_\perp \rho_i$, since this is the relevant parameter in the small $\rho^*$ limit. Note also that as $\rho^*$ decreases, the maximum growth rate increases, meaning that the Tang theory can be viewed as the limit as $\rho^* \to 0$ for the ORB5 simulations, as stated at the start of this chapter. This means that gyrokinetic growth rates of KBMs at short wavelength can be estimated by using this simple formula and MHD simulations. For large $N$, short wavelength, and small $\rho^*$ the ORB5 results closely match the GS2 results as expected. The decrease in growth rates for low-$N_{eff}$ for the ORB5 simulations is due to the global effects (the size of the mode relative to the size of the pedestal region, for example).

## 9.10 Conclusions

Firstly, the correction of the drive strength in ORB5, by doubling the pressure gradient, does provide growth rates that are comparable in magnitude to growth rates observed in MISHKA and GS2 in the appropriate limits. This approach allows KBMs to be simulated in $A_{\|}$ formalism codes. This can also be seen in other simulations undertaken in other codes [88] [89] [90].

Secondly, all the evidence provided indicates that the mode growing in these simulations are consistent with kinetic ballooning modes. The MHD equilibrium defined is sufficiently pedestal-like to serve as a good proxy for a true pedestal while getting around the problems with using a real pedestal equilibrium, such as the boundary effect.

In the local gyrokinetic limit (short wavelength and small $\rho^*$), the ORB5 results match the GS2 growth rates and therefore the results are as expected. As can be seen from Fig. 9.12, the growth rate at high toroidal mode number is well approximated by using the theory provided in Ref. [28], which involves applying a diamagnetic drift correction to the MHD growth rate. On this basis, other kinetic effects appear to be not important. This conclusion must be checked in other gyrokinetic codes to see whether the other kinetic effects play no major part in those simulations either.

For the MHD limit (long wavelength), there is a larger difference between MISHKA and ORB5 growth rates. There are several reasons why this might be so:

- These ORB5 simulations use an unshifted local Maxwellian as the equilibrium distribution function. This means that the background parallel current in the plasma is not consistently included and hence forces and drifts arising from $J_{0\|} \times \delta B_{\perp}$ are not accurately calculated.

- The long wavelength limit of the gyrokinetic equation could be fundamentally not appropriate.
- The $B_{\parallel}$ effects could have been included in a way that is only valid for sort wavelengths.
- Trapped particles, may play an important role under these conditions, or the approximations used to show that MHD and gyrokinetics should agree under these conditions are only valid at short wavelength.
- MISHKA uses an approximation for the plasma inertia (although this does not effect the critical-$\beta$).
- A seemingly innocuous approximation used in ORB5, such as approximation of the perpendicular wavenumber as the poloidal wavenumber, which is actually important.

# Chapter 10

# Extended Equilibria

In Chapter 11, a JET equilibrium will be analysed. However, as previously stated in Chapter 8, the equilibria created by HELENA may only have one magnetic axis and nested flux surfaces. This was not a problem for the circular outer flux surface equilibrium, analysed in Chapter 9, as the region of steep pressure gradient was chosen to be far from the simulation boundary. However, for a JET equilibrium with realistic profiles and flux surfaces, the steep pressure gradient region is near the simulation boundary.

The goal of this chapter is to create an equilibrium which has the same pressure gradient and current as in the experiment and retains the equilibrium parameters (especially around the outboard midplane in the pedestal region), but create a buffer region between the simulation boundary and the large pressure gradient region.

The first step to creating such an equilibrium, is to artificially extrapolate the closed flux surfaces beyond the last smoothed closed flux surface, such that the newly created outermost flux surface is still usable for HELENA and ORB5. Then the profiles need to be shifted such that the pedestal region of the profiles sits in the new location of the pedestal region (in terms of the new definition of $\psi_{norm}$).

A range of equilibria were created and compared to the original equilibrium in the pedestal region (focusing on the outboard midplane where KBMs grow).

## 10.1 The X-point

One important feature of the JET H-mode equilibrium is the X-point, where the poloidal field is zero. The flux surface which the X-point is part of is the last closed flux surface (LCFS) as seen in Fig. 10.1.

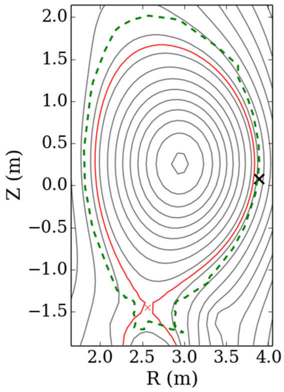

Figure 10.1: Flux surfaces of JET along with the JET wall, depicted from the dashed green line. The flux surface containing the X-point is shown in red. The X-point is located at the bottom of the device, shown by the red cross. This figure is taken from Ref. [92]

The temperature and density profile of the JET discharge # 79503 just before an ELM is given by Fig. 10.2. As can be seen, the region of steep pressure gradient is near the LCFS (The profile does not flatten again in the region shown in Fig. 10.2). ORB5 has a Dirichlet boundary condition at both boundaries of the simulation region. This then leads to suppression of modes that extend to the outer boundary, such as modes growing in the pedestal region. This issue arises from any artifical boundary condition applied to the external boundary, since all boundary conditions rely on setting the value of the electrostatic potential and other parameters to fixed values (or their derivatives). This is especially apparent for low toroidal mode number modes, as the mode extends beyond the area of large pressure gradient and is therefore suppressed by the boundary, since $\psi$ will be normalised to the new flux surfaces. This was accomplished by $p_{new}(\psi) = p_{old}(\psi + 0.1)$. Then a low constant value is assumed in the region beyond the pedestal region.

Since the outer boundary in HELENA or CHEASE must be smooth, the equilibrium near the X-point must be smoothed or a flux surface closer to the magnetic axis chosen. This does not directly affect any growing kinetic ballooning modes, as they

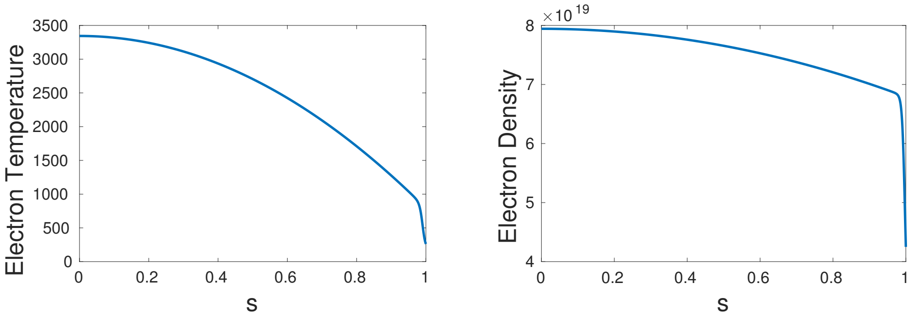

Figure 10.2: JET Temperature (in eV) and density (in m$^{-3}$) profiles for shot # 79503, just before an ELM. The plasma is a deuterium plasma, where $T_e = T_i$. $s^2 = \psi$ as described in Chapter 2.

are centred around the outboard mid-plane and the smoothing of the X-point has little effect on the equilibrium surfaces near the outboard midplane [93] for MHD simulations. The impact of this change for ORB5 simulations will be examined later.

## 10.2 Extrapolation

For the global gyrokinetic analysis, JET shot # 79503 was chosen as the local gyrokinetic analysis for this shot was already undertaken in Ref. [93]. Some modifications were made to this equilibrium. The equilibrium was made up-down symmetric, with the top half of the equilibrium being mirrored by the $Z = 0$ line. This process then removes the X-point that exists in the bottom half of the equilibrium, and has been used in the past to achieve this goal [94]. The temperature and density profiles used are from JET shot # 79503, provided in Fig. 10.2. As can be seen the large pressure gradient region is very near the LCFS.

The extrapolated equilibrium had to retain several features of the base equilibrium. Firstly, the new equilibrium has to have a smooth outer boundary. Secondly, the surfaces within the original boundary must remain largely unchanged, especially in the large pressure gradient region on the outboard midplane, when run through a Grad-Shafranov solver, so that the plasma behaviour is unchanged in this region.

The original equilibrium provides two functions for the spatial positions of the flux surfaces: $R_{orig}(\psi, \chi)$ and $Z_{orig}(\psi, \chi)$ for $\psi \in [0, 1]$ and $\chi \in [0, 2\pi]$. For each value of $\chi$, $R_{orig}$ and $Z_{orig}$ can be written as solely a function of $\psi$.

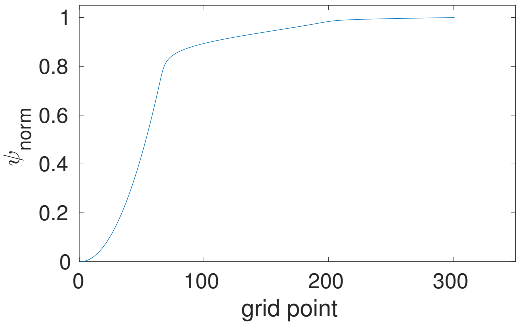

Figure 10.3: Plot of the $\psi$ grid values for the unextrapolated equilibrium.

In Fig. 10.3, the $\psi_{norm}$ grid, which is the value extrapolated over, is shown. As can be seen, the majority of grid points are concentrated in the region of large pressure gradient. There are 301 grid points in total, where $\psi_{norm} = 0.8$ occurs at grid point 69. The increased density of grid points means that more complicated extrapolation procedures are less accurate, as a larger number of grid points have to extrapolated over in order to create a large enough zone beyond the pedestal to ensure the boundary has no effect on modes growing in the pedestal region.

Several methods were considered for the extrapolation. Firstly, cubic spline extrapolation with the not-a-knot condition. Splines are piecewise polynomial approximations connected to each other with various continuity equations. This is where the not-a-knot condition comes in, as this just means that at the connection between different cubic polynomials, the third derivatives must also match. For extrapolations, a cubic polynomial is created for the final few grid points and is then continued to the next grid point, with this system continuing until the required grid is covered.

The second method considered was shape-preserving piecewise cubic interpolation. This method calculates a polynomial between the grid points that has the following properties: it has specified derivatives at both ends (the derivatives are fixed at the original grid points) and the slopes are chosen such that the shape of the data is preserved (if the data is monotonic, so is the curve, and if there is a local extremum, so does the curve). This method is similar to the spline method mentioned above, but is not continuous in the second and third derivatives. The extrapolation occurs in the same way as for the cubic spline extrapolation.

The final method considered was a simple linear extrapolation, which involves drawing a line between the last two points and extrapolating beyond the last point, using this gradient. This method is normally not particularly accurate, but is robust.

Using one of these three methods, the two functions $R_{orig}(\psi, \chi)$ and $Z_{orig}(\psi, \chi)$ are extrapolated, from $\psi \in [0, 1]$ to $\psi_{new} \in [0, 1 + \epsilon]$, separately for each value of $\chi$ to give the extrapolated functions: $R_{extended}(\psi_{new}, \chi)$ and $Z_{extended}(\psi_{new}, \chi)$ for $\psi_{new} \in [0, 1 + \epsilon]$ and $\chi \in [0, 2\pi]$. Then the outermost flux surface, corresponding to $\psi = 1 + \epsilon$ is used as the new outermost boundary in HELENA to calculate the new extended equilibrium.

## 10.3 Extrapolation Results

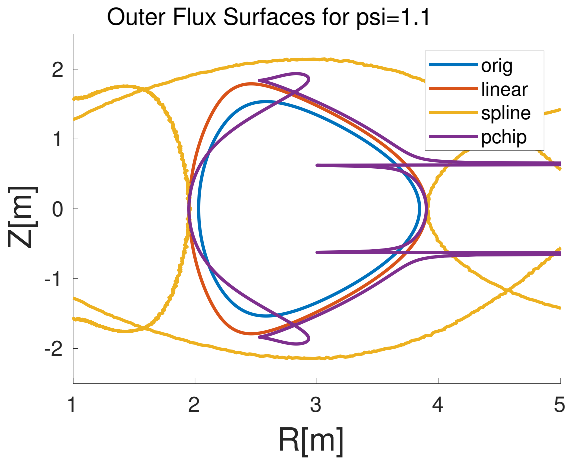

Figure 10.4: Outermost flux surfaces for the three different methods (where linear signifies a linear extrapolation, spline signifies the cubic spline interpolation and pchip refers to the piecewise cubic interpolation) for an extrapolation of 10% ($\psi_{norm} = 1.1$).

Fig. 10.4 shows the outer boundaries provided by the three different extrapolation methods mentioned above for an extrapolation of 10%. As can be seen, the only method of the three methods that extrapolates to a suitable outer boundary is the linear extrapolation. The other methods provide outer boundaries that are not smooth and as such are not suitable for HELENA.

For the two cubic extrapolation methods, the final few points are written as a cubic polynomial, $a_1(x - x_0) + a_2(x - x_0)^2 + a_3(x - x_0)^3$. Therefore, for $x$ near

$x_0$, the extrapolation is approximately linear. However, the expected shape beyond the last closed flux surface, along a line of constant $\chi$, is not expected to be cubic. Therefore, one would expect that when $x$ is sufficiently far from the last closed flux surface, $x_0$, then the extrapolation would produce a surface that is not suitable for HELENA. This happens when $\frac{a_3(x-x_0)^3}{a_1(x-x_0)} \ll 1$. The question then becomes whether the required extrapolation is within this range for the cubic extrapolations. Notice that this problem does not occur for the linear extrapolation and therefore the linear extrapolation method is more robust for larger extrapolations, with the limitations on the new outer boundary.

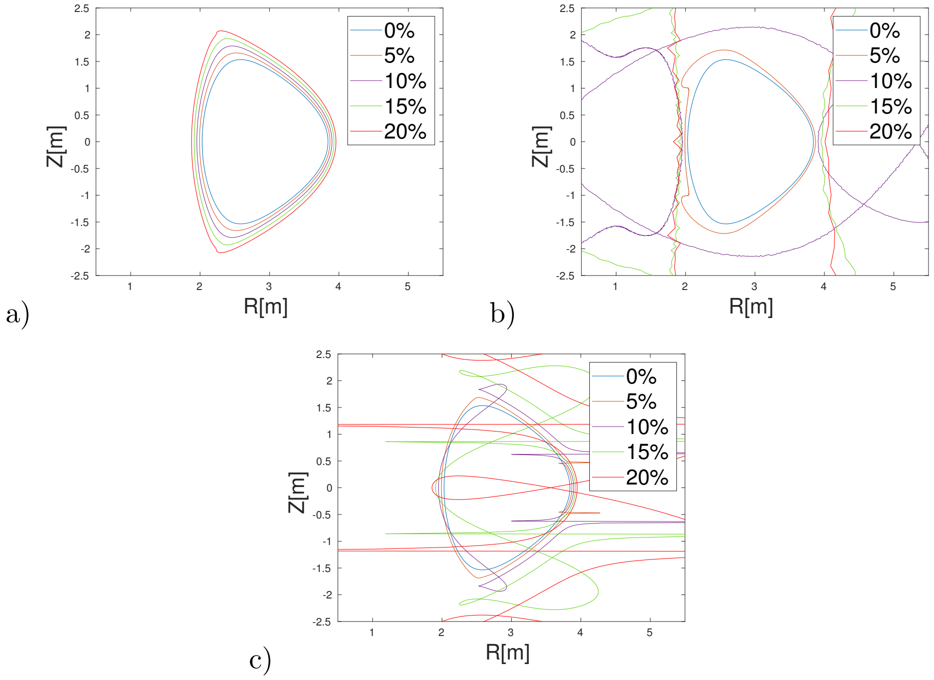

Figure 10.5: Outer flux surfaces for a) linear extrapolation, b) cubic spline extrapolation and c)piecewise cubic interpolation for various values of the extrapolation parameter $\epsilon$, shown here as percentages (10% is equivalent to an extrapolation to $\psi_{norm} = 1.1$).

Fig. 10.5 show the outer surfaces created by all three extrapolation methods, when extrapolated to different values of $\psi_{norm}$. As can be seen, all three methods provide outer flux surfaces that could be used in HELENA, when the extrapolation is carried out over a very small region (for about 5% extrapolation). However, as the region over which extrapolation occurs increases, the outer flux surfaces produced become less reasonable and unusable by Grad-Shafranov solvers (HELENA for this case), as stated previously. As expected, this effect is minimised by the linear extrapolation method for an equivalent increase in $\psi_{norm}$ compared to the other two extrapolation methods.

Fig. 10.6 shows plots of $\psi_{norm}$ vs $R$ for $\chi = 1.84$, 4.91 and 5.52, values at or near the X-points. The green dashed line is at $\psi_{norm} = 0.96$ and shows the region for which there is a shape change in the gradient. This means that especially in this region, the extrapolation for both the second and third methods can only be reliable up to a 4% extrapolation. As can be seen in Fig. 10.5, problems start arising for these extrapolations at 5% extrapolation. However, linear extrapolation does not have the same limitation and can be used for further extrapolations than the other two methods. For this reason the linear extrapolations are more stable than the other two methods.

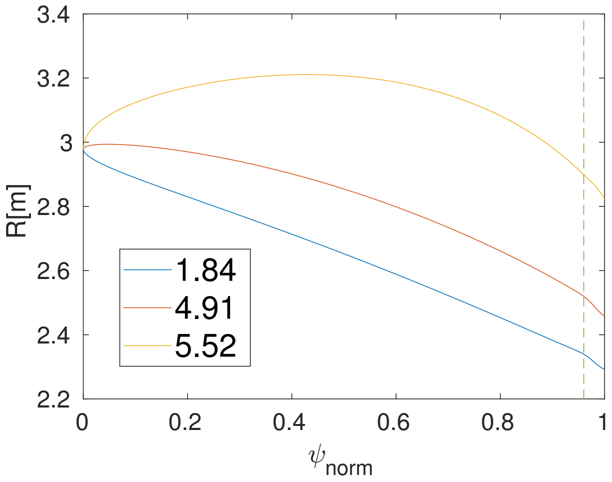

Figure 10.6: $\psi$ vs $R$ for $\chi = 1.84$, 4.91 and 5.52 (around the X-points) for the original equilibrium. The green dashed line is at $\psi_{norm} = 0.96$, where there is a sharp change in the position of $R$ as a function of $\psi_{norm}$.

This warping of the outermost flux surface is most severe at the X-point regions. This can be seen clearly in Fig. 10.5a since the outer flux surface for a 15% increase in $\psi_{norm}$ shows a warping of the flux surfaces at only the X-points. This can be seen more clearly in the greatest linear extrapolation flux surface in Fig. 10.5 a), which is a 20% increase. This warping of the outermost flux surface is due to the fact that the original JET equilibrium, despite the smoothing of the X-points, is still strongly shaped in this region as shown by Fig. 10.7. These figures show $\nabla\psi$ for the original equilibrium and as such show that the equilibrium is strongly shaped in the aforementioned region.

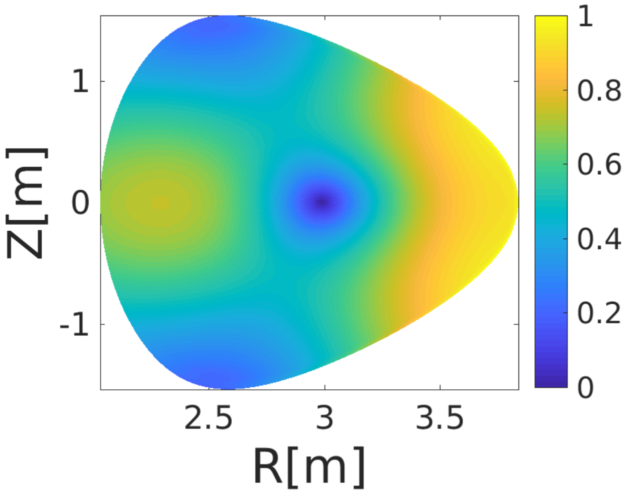

Figure 10.7: $|\nabla\psi|$ for the original equilibrium. The colour scale is in arbitrary units.

Linear extrapolation was chosen as the method for determining the new outermost flux surface, as an extrapolation of more than 5% was required in order to not suppress low-$N$ modes, given the location of the region of large pressure gradient. Linear extrapolation of 10% results in a smooth outer flux surface. Hence the 10% linear extrapolation was chosen as the new outer most flux surface for HELENA, since it was further out than 5%, and did not affect modes in the pedestal region, and the new outer boundary was useable by HELENA.

The second step involves shifting the profiles, such that they are the same within the region inside the last closed flux surface, but extend beyond this region without going negative. The existing temperature and density profiles are shifted, setting $t_{new}(\psi) = t_{old}(\psi - 0.1)$ with a small constant value in the region beyond the pedestal, so that they only cover the existing region. Then the region beyond the original boundary are covered with a constant small non-zero value.

The current profile can be calculated in HELENA, based on resistive steady state and the known inductive electric field. In order for this to occur, a first estimate must be provided. This is just an extrapolated version of the original equilibrium's self-consistent current, with the number of iterations low to ensure that there is not a large difference between the original and extended current profiles.

## 10.4 Linear Extrapolation

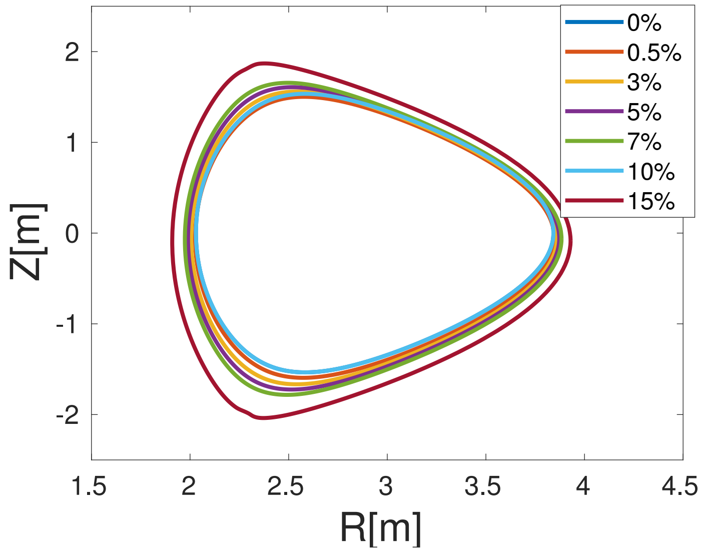

Figure 10.8: Plot of the new extended outermost surface for a selection of different extrapolation amounts.

As can be seen in Fig. 10.8, the flux surfaces created by linearly extrapolating $\psi$ all have smooth outer flux surfaces except for 15% extension in $\psi$. This meant that HELENA ran well with the created outer flux surfaces, except for 15% extension,.

In Fig. 10.9, the same flux surface ($\psi_{norm} = 1$) is plotted for each of the extended equilibria, as well as the original. As can be seen, the flux surface is very similar for all these equilibria. This statement is further supported by Fig. 10.10 a, which is a plot of the difference between the original outermost flux surface and the nearest flux surface for each equilibrium on the outboard midplane ($\theta = 0$). As expected, the difference increases as the extrapolated region is increased. This is due to several reasons. Firstly, as the region is further extrapolated, the equilibrium becomes less accurate, since the original outermost flux surface is the last closed flux surface in the original JET boundary. Secondly, the plot shows only the nearest flux surface on the $\psi$ grid, which varies somewhat with $\epsilon$. However, the change in the position of the outermost flux surface at the outboard midplane for the original and extended equilibria is an error of less than 1/30 of the minor radius.

The magnetic axis of the different equilibria are plotted in Fig. 10.10 b. The difference is again very small relative to the actual position ($\approx$ 2cm on a position of $\approx 2.9m$).

Due to the minimal change in the position of the original last closed flux surface and the magnetic axis in the extended equilibrium, the shape of the magnetic flux surfaces in the extended equilibria is very similar to the original and so the change in the MHD stability should be small.

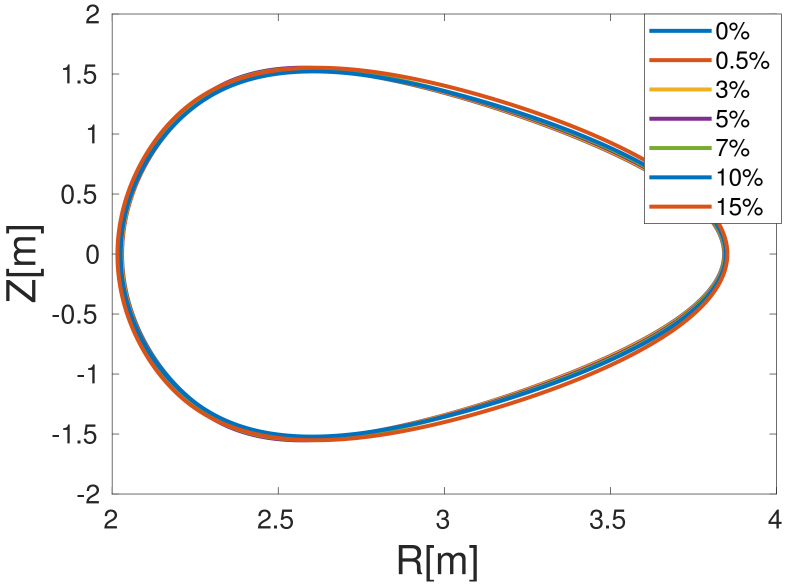

Figure 10.9: Plot of the original outerflux surface ($\psi_{norm} = 1$) for several different extrapolation amounts.

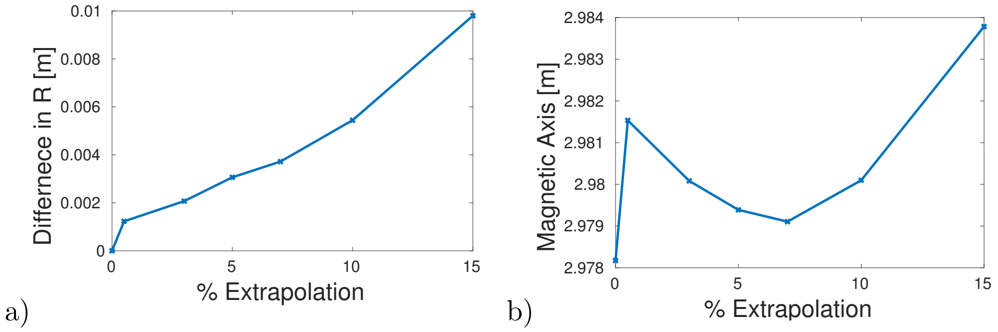

Figure 10.10: Plots for a) the maximum difference between the original outermost flux surface and the nearest equivalent flux surface on the new $\psi$ grid for each extrapolation, between $\chi = -\pi/4$ and $\chi = \pi/4$ (the outboard quarter) and b) the position of the magnetic axis in metres for a variety of extrapolations.

The important quantities for determining the motion of particles in the plasma are the drifts, specifically the curvature and $\nabla B$ drifts. The curvature drift is proportional to the inverse of the radius of curvature, $R_c$. The $\nabla B$ drift is proportional to $\frac{dB}{d\psi}$ on the outboard midplane, provided in Fig. 10.11, which has the same properties as the original: $dB/d\psi$ tends to zero until the region of large pressure gradient, where it peaks at the same flux surface for all these extrapolated equilibria, representing the region where the drive is maximised, before heading back to zero beyond the plasma edge. The peak is larger for the extrapolated surfaces and therefore the drive from the $\nabla B$ drift is expected to be larger for the extrapolated cases. This could lead to a larger growth rate than expected for KBMs. Since both the codes (GS2 and ORB5) were simulated with the expanded code, then the same effect is expected for both codes and so the comparison between both codes performed in Chapter 11 is not affected. Also present in Fig. 10.11, for the largest extrapolation, 15%, is an extra feature in the region before the pedestal region and so might have modes driven by the $\nabla B$ drift in this region.

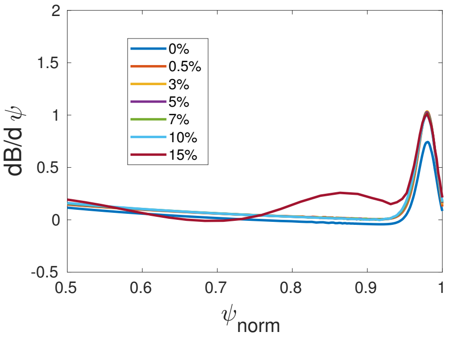

Figure 10.11: $dB/d\psi$, from the magnetic axis to the outboard midplane, for different extrapolations.

## 10.5 Extended Equilibrium

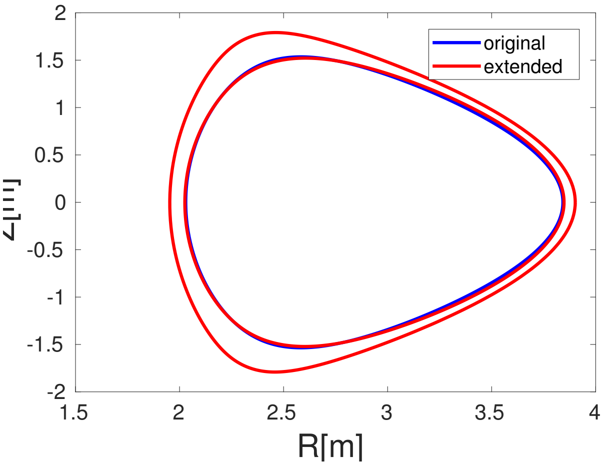

Figure 10.12: Plot of the new extended outermost surface and the equivalent surface with the original equilibrium.

As can be seen from Fig. 10.12, in the region of the outboard midplane, the extended equilibrium has left the original outer flux surface shape unchanged. The profiles are also similar and so the physics of the kinetic ballooning mode should be unaffected by this change. However, now there is a buffer region between the simulation boundary and the region of large pressure gradient and modes growing within the pedestal region on the edge of the plasma are not suppressed by the boundary condition. Note that all the extended equilibria are up-down symmetric since the original equilibrium was up-down symmetric and the extrapolation method does not affect this characteristic.

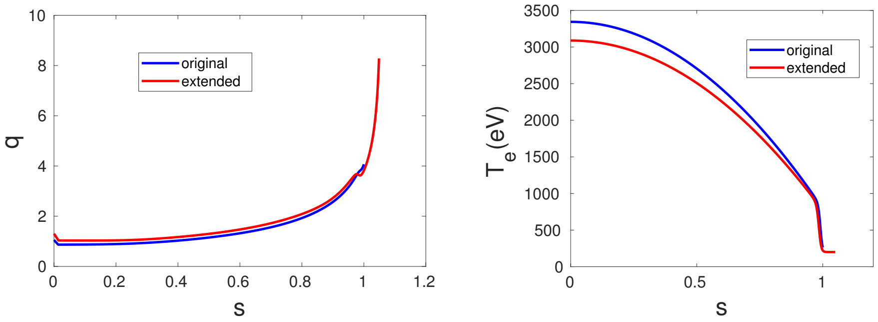

Figure 10.13: Comparisons of the (a) q profile and (b) temperature profile for the original and extended equilibria.

In Fig. 10.13, the q and electron temperature profiles are shown for both the original and extended equilibria. In the pedestal region the temperatures match very closely, but deeper within the core the differences are greater. This is due to the method of extrapolation. The temperature and current profiles should have been kept constant in the original region, either by using a simple extrapolation of the original profiles or by setting the temperature and current profiles to zero (or near zero) beyond the LCFS. Here, the new profiles were created by shifting the position of the pedestal, while keeping the pressure gradient (in terms of $\psi_{norm}$) constant. However, since KBMs grow in the pedestal region, the core region is less important. The q profiles differ more significantly in the pedestal, emphasised in the extended version, due to the large peak in the bootstrap current in this region. Even for minor values of $\epsilon$ (the extrapolation parameter) this profile can change significantly. The effect of this region of negative q gradient is expected to have an effect on the growth rates of KBMs, but this effect will be reduced for global simulations, as the modes extend beyond this region, into the region where the q gradient is positive as for the original profile (such as seen for balllooning modes in Ref. [95]). However, further work should be performed to improve the extrapolation method and avoid such inconsistencies.

# Chapter 11

# JET Equilibrium

Most of this chapter is simply a summary of the results in Ref. [1] with some extra information on the equilibrium and the setting up of the simulations.

In Chapter 9, kinetic simulations (both local and global) were compared in a simplified circular equilibrium. This task was undertaken to compare the results and see whether the results from ORB5 agreed with the theory given in Ref. [28] and with simulations from both GS2 and MISHKA in the appropriate limits.

In Chapter 10, the procedure for creating a JET-like equilibrium that would function correctly for ORB5, while overcoming several of the issues that arise, such as the position of the boundary and the requirement that the simulation only be undertaken over the area that contains closed flux surfaces, was shown.

In this chapter, firstly, the motivation for the current study of kinetic ballooning modes will be shown with the methodology behind the EPED model, that gives predictions for the pedestal height and width.

Secondly, the results from the simulations undertaken in ORB5 with the extended equilibrium will be presented. Then, they will be compared with simulations undertaken in GS2, which has been used in the past to develop the EPED model, further described in Section 11.1. At the top of the pedestal, the local $\rho_i/a$ for JET is $1/600$. Under this condition, the local gyrokinetic theory would be assumed to be sufficient. However, $\rho_i/\Delta$ is a more useful measure, where $\Delta$ is the pedestal width, since the pressure gradient is larger in this region. In JET $\rho_i/\Delta = 1/15$ and therefore, global effects can be expected to have an effect. Therefore global effects are expected to modify the local results.

## 11.1 EPED Model

The EPED model [11] is a predictive model for the pedestal height and width in a tokamak device. The EPED model uses two constraints that together determine the two desired variables.

The first constraint is the peeling-ballooning constraint, based on the peeling-ballooning model and is well understood and tested [14], [96]. In general, in a tokamak, the pedestal height and width evolve together until an ELM is triggered. One prevailing theory as to the mechanism of ELMs is that they are triggered by the large pressure gradient and the resulting bootstrap current in the edge region of the plasma. Therefore, this constraint produces a limit on the possible pedestal height for a given width.

However, in order to predict both the pedestal height and width, a second constraint between the two is required. The second constraint arises from an argument regarding the onset of KBMs near a critical value of $\beta$. Hence, this constraint leads to the dependence of the pedestal height on the poloidal $\beta$ (the $\beta$ using the poloidal magnetic field component solely) at the top of the pedestal. Let the pressure gradient be near the limit for KBM onset $\nabla p \approx \nabla p_{KBM}$, then the average value of $\nabla p$ is proportional to the pedestal height over the pedestal width:

$$\langle \nabla p \rangle = \langle \nabla p_{KBM} \rangle \approx \frac{\beta_{pol,ped}}{\Delta}, \tag{11.1}$$

where $\langle \nabla p \rangle$ is the average pressure gradient across the pedestal, $\beta_{pol,ped}$ is the poloidal beta at the top of the pedestal, and is a measure of the pedestal height, and $\Delta$ is the width of the pedestal. The average pressure gradient can be written in terms of the local magnetic shear [12]: $\nabla p_{KBM} \approx 1/s^{1/2}$. Since the current is majority bootstrap current then $1/\langle j \rangle \approx 1/\beta_{pol,ped}$. Therefore $\Delta = c_1 \beta_{pol,ped}^{0.5}$ [13]. This constraint was the original version of the KBM constraint used in the EPED model. In later versions, the EPED model uses stability calculations [97] for the KBM constraint. This, along with the peeling ballooning mode constraint, provide the prediction for the pedestal height and width.

Previous versions of the EPED model have been created using local gyrokinetic simulations from GS2 to provide the critical beta for kinetic ballooning modes. In this thesis, these simulations are compared with ORB5 simulations to give the global gyrokinetic simulation critical beta.

## 11.2 Original Local Analysis

In Ref. [93], local gyrokinetic simulations of the JET and MAST pedestal were undertaken. These simulations showed that the local gyrokinetic simulations were unstable in the same region as predicted by comparing the pressure gradient to the $N = \infty$ ballooning limit criterion (As MHD ballooning modes become more unstable as $N$ increases, an equilibrium can be tested to see whether it is stable to ballooning modes by testing as $N$ tends to $\infty$).

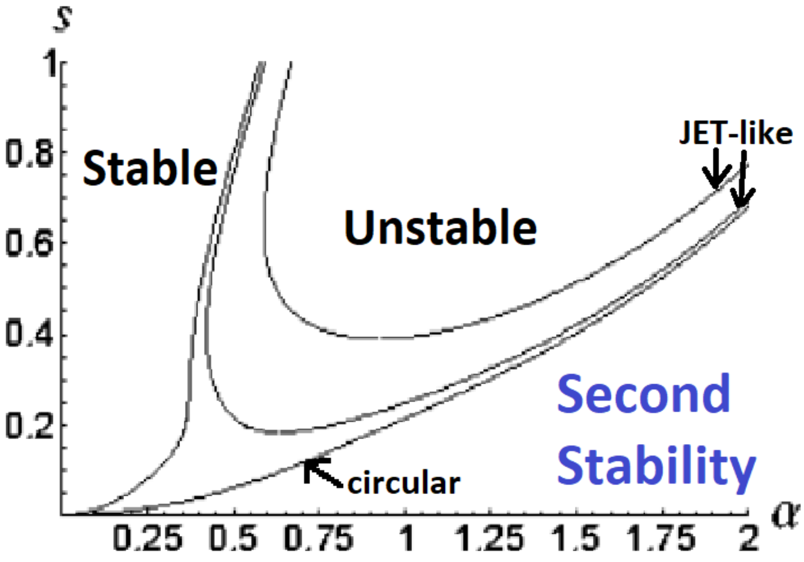

Figure 11.1: $s-\alpha$ diagram for kinetic ballooning modes. The different lines represent differently shaped plasmas.

These simulations also showed that, for low collisionality plasmas, kinetic ballooning modes had access to second stability [98] [99], a second region where KBMs were stable as shown in Fig. 11.1, if the current was high enough to flatten the $q$ profile [93]. Therefore, the plasma was unstable for kinetic ballooning modes if the bootstrap current was artificially removed, but if the bootstrap current was present, kinetic ballooning modes were stable.

Second stability only occurs if the current is high enough to reduce the shear, which then allows the plasma to travel from the stable region in the top left of Fig. 11.1 to the second stability region (the bottom right of Fig. 11.1) without having to pass through the unstable region, which would cause the mode to grow. As can be seen from Fig. 11.1, this could not occur for circular outer boundary plasmas, but can occur for a JET-like plasma.

## 11.3 Equilibrium

In order to compare the global gyrokinetic simulations with previously established local gyrokinetic and MHD results, the same equilibrium as used in Ref. [93] was used in this analysis.

The equilibrium was created from JET shot # 79503, just before an ELM, in order to simulate the kinetic ballooning mode that would limit the pedestal gradient before the ELM.

| Parameter | Value |
|---|---|
| Poloidal Current | 2.5MA |
| Magnetic field at axis | 2.7T |
| q at axis | 1.053 |
| Minor radius | 0.91m |
| Major radius | 2.94m |
| Electron temperature at axis | 3344eV |
| Electron Density at axis | $7.9 \times 10^{19}\text{m}^{-3}$ |

Table 11.1: Profile parameters for the JET simulations used in the ORB5 and GS2 simulations.

For the purpose of these simulations, the equilibrium is the equilibrium originally shown in Chapter 10 for the 10% extrapolation using the linear extrapolation method. The upper half is copied to the lower half in order to ensure that the outer boundary is up-down symmetric. This procedure does not have a large effect on the properties of the equilibrium at the outboard midplane, where kinetic ballooning modes grow [93]. Then the equilibrium underwent the extrapolation which ensures that the pedestal region is further from the simulation boundary, which is more similar to the physical case as a region of vacuum exists between the edge of the plasma and the tokamak walls. This does not have a large effect on the equilibrium properties

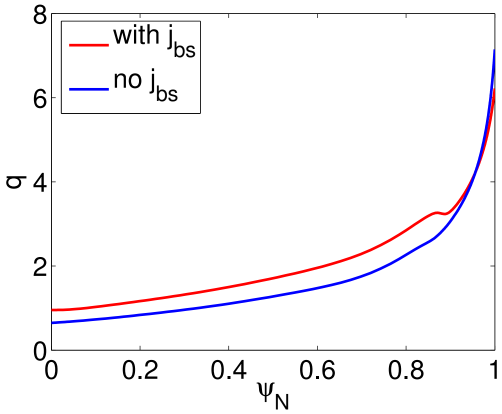

Figure 11.2: q profile for the extended JET simulation with and without the bootstrap current.

as shown in Chapter 10.

In order to study the effect of the bootstrap current on the stability of the equilibrium, two equilibria were created. One involved increasing the bootstrap current by an extra 100% in order to maximise the effect of flattened shear on the stability. The bootstrap current was calculated in HELENA, using the Sauter bootstrap model [100]. The second equilibrium had the bootstrap current set to zero. The current is then assumed to be a combination of the inductively induced current and the bootstrap current. As can be seen in Fig. 11.2, the bootstrap current flattens the q profile in the pedestal region.

The profiles used are those provided by the high resolution Thompson scattering diagnostic, HRTS, system on JET, described in Ref. [101] and then fitted to a tanh function as described in Ref. [102]. The temperature is then increased in order to increase the temperature in the vacuum region. Having such a small temperature in the vacuum region resulted in modes that grew in the vacuum region beyond the pedestal, which had much higher growthrates than any physical modes growing in other regions of the plasma. This is assumed to have been because any small perturbations in this region are a larger percentage of the equilibrium value, and hence the noise is much larger (since the noise is proportional to $\left(\frac{\delta f}{f_0}\right)^2$). These modes were not observed when the constant value was added to the region beyond the pedestal region. The ion temperature is then assumed to be equal to the electron temperature. The resulting pressure profile is given in Fig. 11.3.

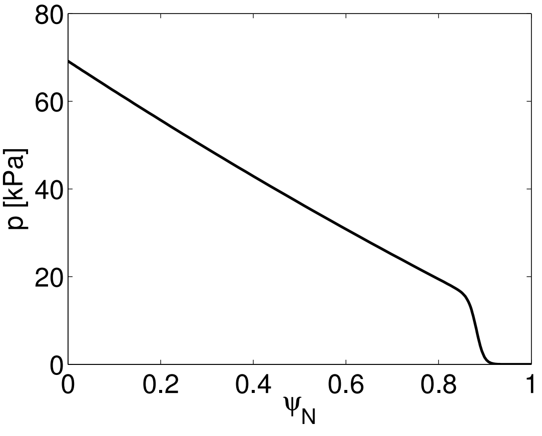

Figure 11.3: Pressure profile for the extended JET simulation.

In order to perform the $\beta$ scan required to calculate the pressure gradient below which KBMs do not grow, the equilibrium was recreated for each separate value of $\beta$. This was accomplished by increasing the temperature value in the core, meaning that the pedestal height was increased, as the vacuum temperature was kept constant. This increased the pressure gradient in the pedestal as the pedestal width was kept constant and the gradient is given by the ratio of the height to the width of the pedestal.

The modifications to the equilibrium in the region of interest are small as shown in Chapter 10. However, local gyrokinetic simulations were undertaken with this modified equilibrium, ensuring that the comparisons given here are valid. These simulations can then also be used to see the effectiveness of using local gyrokinetic simulation results to set the kinetic ballooning mode constraint for the EPED model.

## 11.4 GS2 results

GS2 simulations of the extrapolated equilibrium were undertaken by Dr. Samuli Saarelma, as stipulated in the Declarations. This allowed for both comparison with the ORB5 results with the same equilibrium, but also comparison of the simulation results between the original equilibrium and the extrapolated equilibrium. GS2 was run in the linear mode without collisions and only growing instabilities with long perpendicular wavelength were considered. Only the equilibrium without the bootstrap current has KBMs growing, in accordance with Ref. [93] and the KBMs

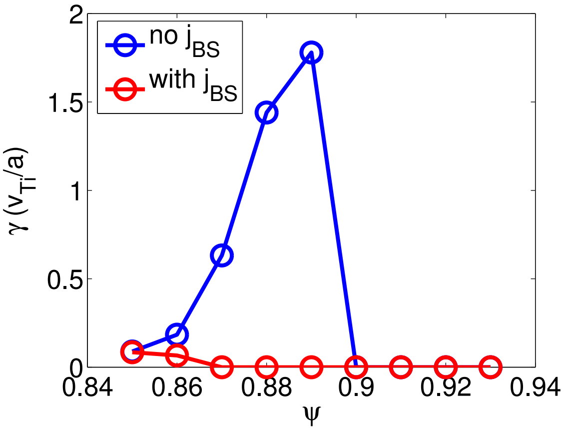

Figure 11.4: Local gyrokinetic growth rates for $\beta = 0.21\%$ for KBMs in the pedestal region with and without the bootstrap current. With the bootstrap current present, the plasma reaches second stability and hence no KBMs grow. These simulations include $\delta B_{||}$ and were performed in the shifted equilibrium.

grew in the region where the MHD $n = \infty$ ballooning mode constraint on the pressure gradient is fulfilled. The GS2 results for the equilibrium pressure, $\beta = 0.21$, are shown in Fig. 11.4.

## 11.5 Numerical Parameters

Simulations were undertaken with time steps of $0.5\Omega_{ci}$, shorter than the time steps used in Chapter 9. Again, simulations were undertaken with a variety of time steps and convergence was observed for this time step. The grid sizes were $N_\psi = 300$, $N_\chi = 1024$ and $N_\phi = 256$. The poloidal grid is greater, compared to the equilibrium in Chapter 9, increased to ensure the more complex shape of the equilibrium is sufficiently covered. Again, as toroidal mode numbers were increased, the number of grid points in the $\chi$ and $\phi$ direction were increased to provide at least four points per wavelength in the toroidal and poloidal directions [91]. As the safety factor is much higher for this equilibrium, than for the equilibrium used in Chapter 9, the poloidal filter was much larger compared to the toroidal filter also.

## 11.6 $N$ Scan

Fig 11.5 shows the $N$ scan for both ORB5 and GS2 without the bootstrap current. With the bootstrap current, GS2 showed no KBMs growing as mentioned earlier. For the GS2 simulations, the peak of the curve is at $N \approx 20$. However, for ORB5 the peak of the $N$ scan is higher and is actually at $N \approx 40$. There could be several reasons why the local simulations in the JET equilibrium have a peak, even thought the simulations for the circular outer boundary (shown in Fig. 9.12) do not. Firstly, this could be because this $N$ scan was undertaken at a lower $\beta$ (nearer the critical-$\beta$), whereas the circular equilibrium was simulated at a much larger $\beta$ in order to encourage KBMs to grow. Secondly, this could be due to kinetic resonances, since the circular equilibrium used in Chapter 9 was chosen to be be closer to an MHD case.

More unexpectedly, however, is the result that the simulations with the bootstrap current and without the bootstrap current simulations, both have the same results. In GS2, the bootstrap current suppresses the KBM. This means that in global gyrokinetics, KBMs do not access second stability [104], due to the presence of the bootstrap current. Note that the bootstrap current was doubled in magnitude, in order to exaggerate its effect on the growth rates. This could be due to the fact that, while the parts of the pedestal region where shear is very low allow access to second stability, the mode extending over larger regions of the pedestal may not be able to access second stability [1]. This effect has also been observed for MHD ballooning modes [103].

The ORB5 growth rates are an order of magnitude larger than the growth rates for GS2. This lead to the work performed with the simulations shown in Chapter 9, with the work where the drive terms were tested and KBMs were considered in a simplified geometry. However, the reason for this difference was not discovered. It could have been due to the normalisation between the different codes, which is why this has been included in Chapter 8.9. However, this has not been confirmed. The reason for this difference was not discovered during the course of this PhD.

## 11.7 $\beta$ Scan

The $\beta$ scan undertaken in ORB5 is shown in Fig. 11.6a). Also shown in Fig. 11.6b) are $N$ scans performed in GS2, for various different values of $\beta$. The bootstrap current has little effect on the critical-$\beta$ for the global gyrokinetic simulations, as it remains near $\beta_{crit} \approx 0.1\%$. This means that the critical-$\beta$ is similar when compared to the local value without the bootstrap current, but, due to KBMs accessing second stability as can be seen in Fig. 11.4, the critical-$\beta$ is much lower than the value calculated for local gyrokinetic simulations with the bootstrap current.

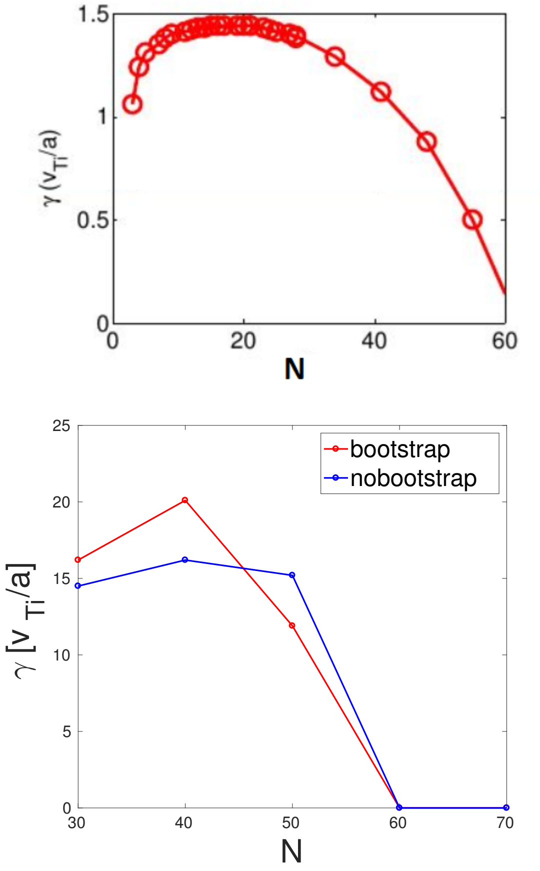

Figure 11.5: Toroidal mode number scans, with the equilibrium $\beta$, for a) GS2 without the bootstrap current, where the maximum growth rate over the surfaces in the pedestal was chosen, and b) ORB5 both with the bootstrap current and without.

## 11.8 Conclusions

In global simulations, second stability is no longer accessed for KBMs growing in the pedestal of JET and MAST [1], despite being present in local simulations for the same equilibrium when the bootstrap current was present [104]. The critical-$\beta$ for the global simulations is found to be close to the value discovered through the local simulations. Furthermore, the peak of the $N$ scan is shifted to higher $N$ for the global simulations compared to the local simulations. This is due to the size of the modes compared to the size of the pedestal, which is not a factor in local gyrokinetics.

The main effect of this work is establishing that second stability access is not present for global gyrokinetics. This could be due to the path that the plasma takes through

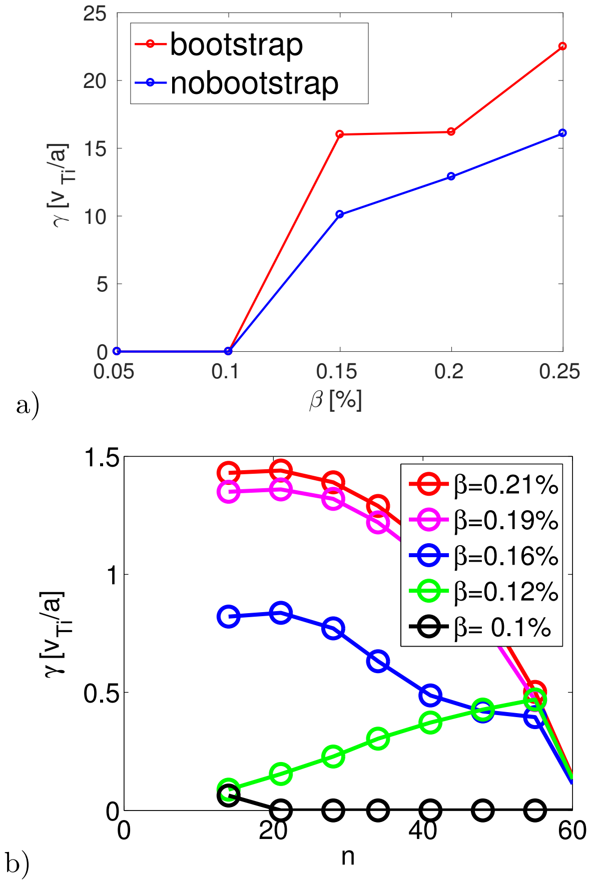

Figure 11.6: a) $\beta$ scan for ORB5 simulations, both with the bootstrap current and without, and b)toroidal mode number scans, with a selection of $\beta$s, for GS2 simulations without the bootstrap current, where the maximum growth rate over the surfaces in the pedestal was chosen.

the $s - \alpha$ diagram, no longer traveling through the stable region due to the high-shear. The global nature of these simulations could mean that the mode extends into regions which cannot access this second stability, meaning that KBMs grow, even though at the position of peak pressure gradient the conditions are met for second stability. As such the EPED model should not use equilibria with the bootstrap current if local simulations are used to establish the KBM constraint for the EPED model. Instead, equilibria should be used that have the bootstrap current artificially suppressed, as this gives a similar critical-$\beta$ to the global gyrokinetic simulations.

# Chapter 12

# Conclusions and Further Work

## 12.1 Conclusions

The pedestal region of the tokamak strongly influences the confinement time of the plasma and hence, whether Lawson's criterion, Eqn. 1.2, can be fulfilled for viable fusion energy production. The purpose of this work was to study pedestal stability, specifically instabilities that have a major effect on pedestal performance. This was accomplished by studying how global effects, observed in MHD simulations, combined with FLR/kinetic effects, observed in local gyrokinetic simulations, for KBMs. This combination was achieved by using ORB5, a global gyrokinetic code.

A simplified circular outer boundary equilibrium was created in order to study KBMs in ORB5, in a simplified geometry, where the magnetic shear was chosen to be small by adjusting the current profile and the pedestal-like region was placed far from the boundary to avoid stabilisation from the boundary wall. This simplified equilibrium is a useful test case that can also be employed by other global codes, in order to test the physics that drives KBMs. Simulations of KBMs were undertaken in this equilibrium, to measure the drive terms relative to local gyrokinetic simulations, magnetohydrodynamic simulations and local gyrokinetic ballooning mode theory [28], to confirm that the drive was being calculated correctly in ORB5. What was discovered, was that the $A_{||}$ formalism used in ORB5 resulted in the drive being reduced in ORB5. A method for correcting the drive was explained and used in several simulations, resulting in the expected growth rates compared to the local gyrokinetic and MHD simulations in the appropriate limits. It was also discovered that, for pedestal-like parameters, the main 'kinetic' effect beyond MHD is simple diamagnetic drift stabilisation. Therefore, it may be enough to use a simple diamagnetic drift stabilisation formula to calculate stability boundaries. A good understanding of the physics of KBMs in the pedestal was achieved, through the use of these simulations. Finally, this testcase shows that ORB5 can be used in further cases, with more confidence that the physics is correct.

Then a method for creating a JET equilibrium for use in ORB5 was explained, in order to prevent the simulation boundary suppressing modes within the pedestal region. The equilibrium also needed to be comprised of closed flux surfaces, which do not appear in reality beyond the LCFS. A simple linear extrapolation scheme was found to be the most effective extrapolation method, while allowing sufficient extrapolation to avoid unphysical stabilisation from the simulation boundary. The properties of the outboard midplane, where KBMs grow, are compared between the extrapolated equilibrium and the original. The magnetic differences are found to be very small on the outboard midplane and as such KBMs are not expected to be strongly unphysically affected by the changes to equilibrium geometry in this region.

Then simulations are shown with the extended equilibrium and comparisons are performed with local gyrokinetic simulations, performed in GS2. Firstly, GS2 simulations show no changes between the original equilibrium [93] and the extended equilibrium simulations shown in this thesis. In ORB5, simulations were undertaken with the bootstrap current and without the bootstrap current. This was to compare with GS2 simulations, which had shown that the presence of the bootstrap current suppressed KBMs. However, the ORB5 simulations show that in global gyrokinetic simulations, the bootstrap current has no effect on the critical-$\beta$, and that the critical-$\beta$ is similar in value to the value measured in the GS2 simulations without the bootstrap current. This is further validated by simulations for a MAST equilibrium in [1].

The results for the critical-$\beta$, provided in Chapter 11, mean that for the EPED model, a model for predicting the pedestal height and width, the KBM constraint could actually be calculated by using GS2 simulations, which are less intensive than ORB5 simulations, but in an equilibrium without the bootstrap current. This model can then be compared to experimentally measured pedestals and finally used to predict the pedestal height and width in future experiments, such as ITER or ARC [105], to compare the profiles presented in papers such as Ref. [106].

## 12.2 Further Work

Some areas of this study that could use further work include:

- Although minor changes in the profiles, for the extended JET equilibrium, did not have an effect on GS2 simulations, further work on the extrapolation method could be useful, in order to avoid any changes that occur in the profiles, especially in the core region, to see if that had any effect on the global simulations undertaken in MISHKA and ORB5.
- The simulations that were undertaken with the JET equilibrium should be repeated with the physics that were observed for the circular outer boundary case included, such as the corrected drive terms. Unfortunately, there was not time to repeat the simulations during this PhD.
- These simulation results could then be compared to experimental pressure profiles from JET, just before an ELM and further simulations could then be run of other devices to fully test the results observed here.
- Predictions could be provided for the pedestal height and width for future plasmas to confirm the predictive power of the EPED model.
- ORB5 could be used to model other instabilities that occur within a plasma with more confidence that the theory in ORB5 is robust.
- The method of correcting the drive strength provided in this thesis, could be tested in other codes, that use an $A_{||}$ formalism.

# Bibliography

[1] S.SAARELMA et al. *Plasma Physics and Controlled Fusion*, 59(064001), 2017.

[2] F.F.CHEN. *An Indispensible Truth: How Fusion Power Can Save the Planet.* Springer, 2011.

[3] J.KESNER et al. *Nuclear Fusion*, 44(1), 2004.

[4] J.D.LAWSON. *Proceedings of the Physical Society Section B*, 70(6), 1957.

[5] D.TWAROG et al. Test of the european transport solver in the frame of integrated tokamak modelling. *Technical Report No. 2051/AP*, Institute of Nuclear Physics, Polish Academy of Sciences, 2001.

[6] J.H.E.PROLL. Trapped-particle instabilities in quasi-isodynamic stellarators. *PhD thesis*, Greifswald Max-Planck-Institut für Plasmaphysik, 2014.

[7] F.WAGNER et al. *Physical Review Letters*, 49(1408), 1982.

[8] H.ZOHM. *Plasma Physics and Controlled Fusion*, 38(105), 1996.

[9] A.HASSANEIN et al. *Journal of Nuclear Materials*, 390-391(777), 2009.

[10] A.V.BOGOMOLOV et al. *Nuclear Fusion*, 55(8), 2015.

[11] P.B.SNYDER et al. *Nuclear Fusion*, 49(8), 2009.

[12] P.B.SNYDER et al. *Physics of Plasmas*, 9(2037), 2002.

[13] P.B.SNYDER et al. *Physics of Plasmas*, 16(056118), 2009.

[14] P.B.SNYDER et al. *Nuclear Fusion*, 47(961), 2007.

[15] R.J.GOLDSTON and P.H.RUTHERFORD. *Introduction to Plasma Physics.* Institute of Physics Publishing, 1995.

[16] W.HORTON. *Reviews of Modern Physics*, 71(735), 1999.

[17] G.TRYGGVASON. *Journal of Computational Physics*, 75(253), 1988.

[18] W.W.LIU. *Journal of Geophysical Research*, 102(4927), 1997.

[19] E.A.FRIEMAN and L.CHEN. *The Physics of Fluids*, 25(502), 1982.

[20] R.G.LITTLEJOHN. *Journal of Mathematical Physics*, 23(742), 1982.

[21] R.G.LITTLEJOHN. *Journal of Mathematical Physics*, 20(2445), 1979.

[22] W.W.LEE. *The Physics of Fluids*, 26(556), 1983.

[23] T.S.HAHM. *The Physics of Fluids*, 31(2670), 1988.

[24] N.TRONKO et al. *Plasma Physics and Controlled Fusion*, 59(064008), 2017.

[25] B.F.MCMILLAN and A.SHARMA. *Physics of Plasmas*, 23(092504), 2016.

[26] B.J.HUNT. *The Maxwellians*. Cornell University Press, 1991.

[27] S.COWLEY. *From ITER time scales to Gyro-Kinetics*. Wolfgang Pauli Institute, Vienna, September 2008.

[28] W.M.TANG et al. *Nuclear Fusion*, 20(11), 1980.

[29] J.R.CARY and R.G.LITTLEJOHN. *Annals of Physics*, 151(1), 1983.

[30] A.BRIZARD. *Journal of Plasma Physics*, 41(541), 1989.

[31] T.S.HAHM. *Physics of Plasmas*, 3(4658), 1996.

[32] R.G.LITTLEJON. *Journal of Plasma Physics*, 29(111), 1983.

[33] A.BRIZARD. *Journal of Plasma Physics*, 2(459), 1995.

[34] F.I.PARRA and I.CALVO. *Plasma Physics and Controlled Fusion*, 53(4), 2011.

[35] D.CORREA-RESTREPO et al. *Physica A: Statistical Mechanics and its Applications*, 136 Issues 2-3(453), 1986.

[36] H.SUGAMA. *Physics of Plasmas*, 7(466), 2000.

[37] M.KOTSCHENREUTHER. *Bulletin of the American Physical Society*, 34(2107), 1988.

[38] P.ANGELINO et al. *Physics of Plasmas*, 13(052304), 2006.

[39] X.XIAO et al. *Physics of Plasmas*, 18(032504), 2011.

[40] S.V.PUTVINSKII. *Reviews of Plasma Physics*, Consultants Bureau, New York(261), 1993.

[41] S.WANG. *Physics of Plasmas*, 5(3319), 1998.

[42] F.L.HINTON and R.D.HAZELTINE. *Reviews of Modern Physics*, 48(239), 1976.

[43] S.JOLLIET et al. *Computer Physics Communications*, 177(409), 2007.

[44] Y.IDOMURA et al. *Nuclear Fusion*, 43(234), 2003.

[45] P.ANGELINO et al. *Physics of Plasmas*, 13(052304), 2006.

[46] H.SUGAMA. *Reviews of Modern Plasma Physics*, 1(9), 2017.

[47] A.MISHCHENKO et al. *Physics of Plasmas*, 24(081206), 2017.

[48] R.SYDORA et al. *Plasma Physics of Controlled Fusion*, 38(A281), 1996.

[49] R.HATZKY. *Physics of Plasmas*, 9(898), 2002.

[50] W.W.LEE. *Journal of Computational Physics*, 72(243), 1987.

[51] J.VILLASENOR and O.BUNEMAN. *Computer Physics Communications*, 69(306), 1992.

[52] J.LIOUVILLE. *Journal fur die Reine und Angewandte Mathematik*, 88(277), 1879.

[53] E.SULI and D.MEYERS. *An Introduction of Numerical Analysis.* Cambridge University Press, 2003.

[54] M.FIVAZ et al. *Computer Physics Communications*, 111(27), 1998.

[55] K.HOLLIG. *Finite Element Methds with B-Splines.* Society for Industrial and Applied Mathematics, 2003.

[56] S.JOLLIET et al. *Journal of Computational Physics*, 231(3), 2012.

[57] J.V.W.REYNDERS. Gyrokinetic simulation of finite-beta plasmas on parallel architectures. *PhD Thesis*, Princeton University, 1992.

[58] J.C.CUMMINGS. Gyrokinetic simulation of finite-beta and self-generated sheared-flow effects on pressure-gradient-driven instabilities. *PhD thesis*, Princeton University, 1995.

[59] R.HATZKY et al. *Journal of Computational Physics*, 225(568), 2007.

[60] J.W.CONNOR and R.J.HASTIE. *Plasma Physics*, 17(97), 1975.

[61] B.COPPI and G.REWOLDT. *Physics Letters A*, 49 Issue 1(36), 1974.

[62] J.W.CONNOR et al. *Plasma Physics*, 22(757), 1980.

[63] E.A.FRIEMAN et al. *The Physics of Fluids*, 23(1750), 1980.

[64] P.J.CATTO and K.T.TSANG. *The Physics of Fluids*, 20(396), 1977.

[65] K.ALEYNIKOVA and A.ZOCCO. *Physics of Plasmas*, 24(092106), 2017.

[66] M.S.CHANCE et al. *7th IAEA Plasma Physics and Controlled Nuclear Fusion Research, Innsbruck Austria 1978*, 1(677), 1979.

[67] K.V.ROBERTS and J.B.TAYLOR. *Physical Review Letters*, 8(197), 1962.

[68] J.W.CONNOR et al. *Physical Review Letters*, 40(396), 1978.

[69] H.ALFVEN. *Nature*, 150(405), 1942.

[70] W.BAUMJOHANN and R.A.TREUMANN. *Basic Space Plasma Physics*. Imperial College Press, 1997.

[71] S.I.BRAGINSKII. *Reviews of Plasma Physics*, 1(205), 1965.

[72] G.BATEMAN. *MHD Instabilities*. The MIT Press, 1978.

[73] J.H.POYNTING. *Philosophical Transactions of the Royal Society of London*, 175(343), 1884.

[74] V.I.ILGISONIS. *Physics-Uspekhi*, 52(7), 2009.

[75] J.P.FREIDBURG. *Ideal MHD*. Cambridge University Press, 2014.

[76] H.GRAD and J.HOGAN. *Physical Review Letters*, 24(1337), 1970.

[77] V.D.SHAFRANOV. *Soviet Journal of Experimental and Theoretical Physics*, 6(545), 1958.

[78] G.BATEMAN. *Nuclear Fusion*, 13(581), 1973.

[79] H.LUTJENS et al. *Computer Physics Communications*, 97(5219), 1996.

[80] S.POEDTS et al. *FOM Rijnhuizen Report*, (RR 96-228), 1996 Jan.

[81] F.TROYON et al. *Plasma Physics and Controlled Fusion*, 26(209), 1984.

[82] A.D.TURNBULL et al. *Journal of Computational Physics*, 66(391), 1986.

[83] J.DELUCIA et al. *Journal of Computational Physics*, 37(183), 1980.

[84] J.R.KING et al. *Physics of Plasmas*, 24(012504), 2017.

[85] L.L.LAO et al. *Nuclear Fusion*, 25(1611), 1985.

[86] B.S.JINGFEI MA. The macro- and micro-instabilities in the pedestal region of the tokamak. *PhD Thesis*, University of Texas, 2015.

[87] K.D.NIELSON. Analysis and gyrokinetic simulation of mhd alfven wave interactions. *PhD Thesis*, University of Iowa, 2012.

[88] N.JOINER et al. *Physics of Plasmas*, 17(072104), 2010.

[89] E.A.BELLI and J.CANDY. *Physics of Plasmas*, 17(112314), 2010.

[90] G.DONG et al. *Physics of Plasmas*, 24(081205), 2017.

[91] C.E.SHANNON. *Proceedings of the IRE*, 37 Issue 1(10), 1949.

[92] N.R.WALKDEN et al. *Nuclear Fusion*, 57(3), 2017.

[93] S.SAARELMA et al. *Nuclear Fusion*, 53(12), 2013.

[94] D.R.HATCH et al. *Nuclear Fusion*, 56(104003), 2016.

[95] WEBSTER et al. *Physics of Plasmas*, 12(092502), 2005.

[96] T.E.EVANS et al. *Nature Physics*, 2(419), 2006.

[97] P.B.SNYDER et al. *Physics of Plasmas*, 19(056115), 2012.

[98] S.SAARELMA et al. *39th EPS Conference on Plasma Physics*, Stockholm Sweden(O4.111), 2012.

[99] C.M.ROACH et al. *24th IAEA Fusion Energy Conference*, San Diego USA(TH/5-1), 2012.

[100] O.SAUTER and C.ANGIONI. *Physics of Plasmas*, 6(2834), 1999.

[101] L.FRASSINETTI et al. *Review of Scientific Instruments*, 83(013506), 2012.

[102] R.J.GROEBNER et al. *Plasma Physics and Controlled Fusion*, 44(5A), 2002.

[103] H.R.WILSON and R.L.MILLER. *Physics of Plasmas*, 6(873), 1999.

[104] C.H.MA and X.Q.XU. *Nuclear Fusion*, 57(016002), 2017.

[105] B.N.SORBORN et al. *Fusion Engineering and Design*, 100(378), 2015.

[106] J.E.KINSEY et al. *Nuclear Fusion*, 51(8), 2011.